Boosting Solar Energy Harvesting with Ordered Nanostructures Fabricated by Anodic Aluminum Oxide Templates

Dissertation

zur Erlangung des Doktorgrades

Dr. rer. nat.

vorgelegt der

Fakultät für Mathematik und Naturwissenschaften der

Technischen Universität Ilmenau

von

M. Sc. Rui Xu

Ilmenau

TECHNISCHE UNIVERSITÄT
ILMENAU

Die Arbeit wurde von Prof. Dr. Yong Lei betreut.
urn:nbn:de:gbv:ilm1-2020000045

1. Gutachter: Prof. Dr. Yong Lei
2. Gutachter: Prof. Dr. Heiko O. Jacobs
3. Gutachter: Prof. Dr. Puxian Gao

Tag der Einreichung: 20/08/2019

Tag der wissenschaftlichen Aussprache: 07/02/2020

Abstract

To date, technical development has boosted the efficiencies of solar energy conversion devices with conventional planar architectures to be close to the respective theoretical values, which are hard to be further improved without reforming the device structures. Alternatively, ordered nanostructure arrays have recently emerged as efficacious scaffolds to construct devices for converting energy more efficiently due to their advantageous optical effects. To meet the global energy requirements for producing renewable energy efficiently, a general approach is needed to fabricate diverse ordered nanostructure arrays. In the meantime, the approach should allow for fine tuning in every set of nanounits towards obtaining desired properties. Herein, we utilized anodic aluminum oxide (AAO) templates to provide a versatile method for constructing ordered nanostructure arrays from one to two dimensions. Firstly, arrays of one-dimensional Au nanowires comprising two components of pillar and truncated pyramid were fabricated. Then, periodic one-dimensional Janus hetero-nanostructures with programmable morphologies, compositions, dimensions, and interfacial junctions were realized. Finally, two-dimensional superlattice photonic crystals with two sets of nanopores were constructed via a combination of the AAO template and the structural replication technique. Subsequently, these as-obtained nanostructures were integrated into photoelectrochemical water-splitting cells and solar-to-thermal conversion systems, which significantly boosted solar energy harvesting performance. In conjunction with theoretical simulations, we further elucidated that the enhanced light harvesting ability can be ascribed to twofold facts: photonic effects and surface plasmon resonance which thus provide a route to manipulate light at the nanoscale.

Zusammenfassung

Bis heute hat die technische Entwicklung die Effizienz der solaren Energiekonversion in Anwendungen mit planarem Aufbau nahe an die entsprechenden hierfür theoretisch erreichbaren Werte herangeführt, welche nur sehr schwer weiter verbessert werden können ohne grundlegende Veränderungen am Device-Aufbau. Als Alternative dazu sind geordnetete Nanostruktur-Arrays in letzter Zeit als wirksame Möglichkeiten zum Aufbau von Devices für die effizientere Energieumwandlung hervorgetreten, durch ihre vorteilhaften optischen Effekte. Um die globale Nachfrage an Energie für die effiziente Produktion von erneuerbaren Energien bedienen zu können braucht es einen grundlegenden Ansatz um verschieden geordnete Nanostruktur-Arrays herzustellen. Indessen sollte das Vorgehen zur Feineinstellung der verschiedenen Nanostruktur-Einheiten hin zu den gewünschten Eigenschaften unternommen werden. Dafür wurden Anodische-Aluminium-Oxid (AAO) Template verwendet, da sie eine vielseitige Methode zur Konstruktion von 1 bis 2-dimensionalen geordneten Nanostruktur-Arrays bieten. Zuerst wurden Arrays von 1-dimensionalen Gold-Nanodrähten bestehend aus zwei Komponenten aus Säulen- und abgestumpften Pyramiden hergestellt. Nachfolgend wurden periodische 1-dimensionale Janus Heteronanostrukturen mit einstellbaren Morphologien, Kompositionen, Dimensionen und Flächenverbindungen realisiert. Zuletzt wurden 2-dimensionale photonische Kristalle im Supergitter mit zwei Sets von Nanoporen konstruiert durch die Kombination von AAO-Templaten und der strukturellen Replikationstechnik. Anschließend wurden die erlangten Nanostrukturen in photoelektrochemischen Zellen zur Wasserspaltung und in solarthermische Energieumwandlungssysteme integriert, was die solare Ausbeute jeweils signifikant verbesserte. In Verbindung mit theoretischen Simulationen wurde weiter gezeigt, dass die verbesserte Lichtausbeute zwei Mechanismen zugeordnet werden kann: Photonische Effekte und/oder plasmonische Oberflächenresonanz, welche weitere Möglichkeiten zur Manipulation des Lichts im Nanobereich ermöglichen.

Acknowledgement

This work was carried out from October 2014 to June 2019 under the supervision of Prof. Dr. Yong Lei at the Institute of Physics and the Institute of Micro- and Nanotechnologies (IMN MacroNano®), Technische Universität Ilmenau.

First and foremost, I want to express my sincere gratitude to my doctor supervisor Prof. Dr. Yong Lei for his continuous encouragement, guidance, and advice. He helped me in all the time of my research and always provided fruitful suggestion when I met with dilemmas. He also encouraged me to be more positive in the academic communication.

Moreover, I want to deeply thank all our group members for their kind help in the academic matters and everyday life in Germany. My special thanks to Dr. Liaoyong Wen for the collaboration work in the photoelectrochemical water-splitting project. Many thanks to Dr. Huaping Zhao, Dr. Zhijie Wang, Mr. Zhiqiang Zeng, Mr. Max Sommerfeld, Dr. Shipu Xu, Dr. Samar Tarish, Mr. Huanming Zhang, Mr. Yuhan Wu, Dr. Yan Mi, Dr. Yaoguo Fang, Dr. Min Zhou, Dr. Yang Xu, Mr. Marco Eckstein, and Dr. Ahmed Shukur Hameed Al-Haddad for their useful discussion and technique supports. It is my great honor to work in such a friendly group.

I gratefully acknowledge the academic discussion in the field of nanophotonics with Prof. Erich Runge and Mr. Sebastian Bohm. For the FIB and argon ion milling systems, I want to thank Dr. Henry Romanus, Mr. Dominik Flock and Ms. Diana Herz for their contributions.

Last but not least, I would like to thank my family for supporting me spiritually through my Ph.D. studies.

Table of Content

List of Figures

List of Abbreviations

AAO	anodic aluminum oxide
ALD	atomic layer deposition
PVD	physical vapor deposition
ECD	electrochemical deposition
FIB	focused ion beam approach
EBL	electron beam lithography
SPR	surface plasmon resonance
(0-3)D	(zero-three) dimensional
SEM	scanning electron microscopy
TEM	transmission electron microscopy
XRD	X-ray Powder Diffraction
EDX	energy-dispersive X-ray spectroscopy
XPS	X-ray photoelectron spectroscopy
DMSO	dimethyl sulfoxide
PMMA	polymethyl methacrylate
MB	methylene blue
FDTD	Finite Difference Time Domain
NP	nanoparticle
NW	nanowire
NT	nanotube
NC	nanocone
ND	nanodent
NR	nanorod
HNs	hetero-nanostructures
TP	truncated-pyramid
PTP	pillar/truncated-pyramid
PhCs	photonic crystals
SPhCs	superlattice photonic crystals
IPCE	incident photon to charge carrier efficiency
PEC	photoelectrochemical
ALA	averaged light absorption
UV-Vis	ultraviolet–visible spectroscopy
RHE	reversible hydrogen electrode
SHE	standard hydrogen electrode

CHAPTER 1. Introduction

Currently, the global energy utilization presents two distinct features. First, the conventional fossil energies, which account for more than 70% of power supply, could not meet the increasing demand for energies. The production of fossil energies like oil and natural gas is predicted to peak over in the next few decades.[1, 2] Moreover, the extensive use of fossil energies would unavoidably release a large mount of pollutants and CO_2 to the ambient. The tremendously increasing CO_2 in the atmosphere has been regarded to be responsible for the global warming.[3] Thus, exploring an alternative energy resource with renewable and environmental characteristics and utilizing it efficiently could be of great significance to address the energy crisis.

With the magnitude of available energy directing towards the surface of the earth at any one instant equal to 130 million 500 MW power plants, solar power has long been esteemed as the inexhaustible source for generating electricity and clean fuels.[4] So far, a large diversity of devices have been developed to convert solar power to electricity, fuels and thermal energy, including photovoltaics, photoelectrochemical (PEC) water splitting cells, and solar steam generation, solar desalination, solar thermoelectrics, etc. With the development of advanced techniques in material preparations and device fabrications, the energy conversion efficiencies of these devices have been approaching to the theoretical values. Though the feed-in tariff paid for electricity from large-scale photovoltaic installations in Germany fell from over 40 ct kWh^{-1} in 2005 to 9 ct kWh^{-1} in 2014,[5] a continuous effort for reducing the cost and increasing the efficiencies is still needed to make solar energy converting techniques more popular in the energy market.

For further improving the efficiencies of these energy converting devices to break the performance limits imposed by the conventional planar architecture, an important point is how to manipulate the incident light so that more light can be efficiently scattered and absorbed within the active semiconductors and that the photogenerated carriers can be fully

used prior to recombination. Ordered nanostructure arrays are usually introduced as key functional components in the device construction.[6, 7] On one hand, photonic effects existing in such ordered nanostructures can enhance the photon absorption efficiency via scattering, diffraction, and anti-reflection. On the other hand, surface plasmon resonance (SPR) originating from periodic plasmonic nanostructures gives rise to electromagnetic radiation guidance and near-filed electric field enhancement which can fold the incident light into the active material to reduce the recombination possibilities of photo-generated charge carriers via decreasing the diffusion distance of the charge carriers before being collected.

In comparison with the irregular nanostructures in which the nanounits distribute randomly, ordered nanostructure arrays exhibit a superior capability in regulating the energy converting procedures to a certain direction and range, which is beneficial for optimizing the efficiencies and attaining a reproducible performance. The self-standing nanounits with well spacial orientation/arrangement are crucial to making the reactions of energy conversion occur in nanoscale, without interrupting the reactions in other units. Such advanced architectures have been widely employed in energy-related devices, including various solar energy conversion devices, ion batteries, and supercapacitors.[1, 6, 8, 9] According to the different roles in the conversion of energy, ordered nanostructure arrays could be purposely designed with various morphological nanounits, like nanoparticle (NP) arrays, nanowire (NW) arrays, nanotube (NT) arrays, and nanocone (NC) arrays, etc.[10] For in-depth fundamental research and practical utilization, it is imperative to develop an approach to fabricate large-scale highly-ordered nanostructures for acquiring uniform optical response over large areas. In the meantime, the approach should allow for fine tuning in structural geometries towards realizing desired optical property to satisfy diverse operational requirements and obtain superior solar conversion efficiency, for example, to combine SPR and photonic effect together to enhance light utilization over the whole solar spectrum for solar power conversion devices.

The main goal of this dissertation is to construct periodic nanostructures with well-designed geometries through exploiting the AAO technique and to integrate periodic nanostructures into functional devices for enhancing solar energy conversion efficiency. The key achievements of this dissertation are summarized as follows:

(1) Au pillar/truncated-pyramid (PTP) arrays were fabricated via a combination of two-step aluminum anodic oxidization and structural replication. The geometries (e.g., size and height) of Au PTP array can be facially tuned by changing the anodization parameters and the wet-chemical etching time. SPR modes and photonic modes are successfully combined to contribute to the light utilization of the CdS/Au PTP photoanode. Superior optical absorption of about 95% within a wide wavelength range from 300-600 nm is observed from the CdS/Au PTP photoanode which consequently demonstrates an omni-directional photocurrent with an enhancement of about 400% over that of planar CdS photoanode.

(2) A general yet scalable technique is utilized to fabricate arrays of programmable Janus hetero-nanostructures (HNs) based on AAO multi-pore templates. By designing and employing an over-etching process to partially expose four-edges of one set of nanocomponents in a binary-pore template, selective deposition and interfacing of the other set of nanocomponents is successfully achieved along the exposed four-edges to form a densely packed array of Janus HNs on a large scale. In combination with upgraded two-step anodization, the synthesis provides high degrees of freedom for both nanocomponents of the Janus HNs, including morphologies, compositions, dimensions, and interfacial junctions. Arrays of TiO_2–Au and TiO_2/Pt NPs–Au Janus HNs are designed and fabricated, demonstrating about 2.2 times photocurrent density and 4.6 times H_2 evolution rate of that obtained from their TiO_2 counterparts. The enhancement was mainly determined as a result of SPR induced direct hot electron injection and plasmon resonance energy transfer near the interface of TiO_2 nanotubes and Au nanorods.

(3) Ni dual-pore superlattice photonic crystals (SPhCs) with an area of about 500 mm^2 were realized, which is about 50 times larger than the reported maximum SPhC area. The self-alignment effect between dual sets of pores circumvents the mismatching error in the conventional multi-step lithography, thus leading to uniform structure over large areas. For the first time, we systematically modulated the geometrical parameters for each set of pores in Ni SPhCs (e.g., pore periodicity, depth, size, morphology) and investigated the corresponding influence on light trapping performance. We realized omnidirectional stably-strong light absorption spectra (~95%) with sharp cutoff wavelengths which were spectrally programmable in the range of about 600 - 1500 nm. Numerical simulations indicate that the prominent light trapping capability is attributed to the synergistic effects of cavity resonance and SPR. Subsequently, Ni SPhCs were exploited to promote a solar steam generation system and a solar thermoelectric system. Accordingly, the water evaporation efficiency and the open circuit voltage output were enhanced by a factor of 2.3 and 2.5, respectively.

CHAPTER 2. General Background

2.1 Techniques for realizing ordered nanostructure arrays.

To date, there have been various techniques to fabricate ordered nanostructure arrays. In the aspects of nanostructure formation, these techniques could be divided into two approaches: 'top-down' and 'bottom-up'. The top-down approach usually utilizes the micro-fabrication methods in which externally controlled tools are used to cut, mill, or shape materials into the desired profile and order at the nanoscale. The bottom-up approach, on the other hand, utilizes single-molecule components to self-organize, self-assemble or positional-assemble into the desired nanostructures. Such a bottom-up approach could be able to produce devices in parallel with the cost much cheaper than the top-down method, but could potentially be overwhelmed when the complexity of the desired assembly increases. As to the specific technologies to realize nanostructure arrays, the methods mainly include template-directed techniques, lithographic techniques, nano-imprinting, etching techniques, and self-assembly. Herein, we will elaborate on these techniques point-by-point.

2.1.1 Lithographic techniques

Varieties of lithographic techniques were developed in the past 40 years.[11-13] Optical lithography refers to an approach that utilizes light to transfer the geometric pattern from a photo mask to a light-sensitive chemical on the substrate and to accomplish a certain nanostructure based on the patterned chemical. The resolution limit is from less than 10 nm to several micrometers, depending on the wavelength of the used light. It was demonstrated that the full width at half maximum of the focus spot can be 7 nm with an enhancement of about 800 at the UV region.[14] Due to the multiple steps of optical lithography, there are several other lithographic techniques being developed as alternatives, such as electron beam lithography (EBL), colloidal lithography *etc*. EBL is a pattern writing technology by scanning with a focused electron beam.[15] It is widely used in producing very small samples experimentally and the pattern can be very fine because of the focused electron beam and

small size. Another advantage of EBL is the capability of the mask less lithography, which avoids the expense of masking. The main problem is the throughput capability, namely, when it comes to large industrial devices, the higher resolution cannot be achieved simultaneously by a single electron beam. Although the multiple-beam system has been developed, it has not yet arrived at the required level. As the development of colloidal science and self-assembling technique, colloidal lithography has been applied to fabricate highly ordered arrays of nanostructures. The colloidal monolayers can be prepared in large scale by using monodispersed colloidal spheres in very small size, to generate periodic nanostructure array. By controlling the etching conditions, the spacing (50-400 nm) and diameter (60-600 nm) of nanostructure arrays could be highly manipulated, in principle. What's more, the simple, low-cost and time-effective method makes the colloidal lithography as a flexible alternative lithographic technique in comparison with the former ones. However, colloidal lithography also has its disadvantage like the surface impurity of the array.

2.1.2 Nano-imprinting

At present, fabrication technologies of micro- and nanostructures have to face the associated defects, when it comes to large industrial devices. Alternatively, nano-imprinting, which was first proposed by the Chou group,[16, 17] has been considered as the most promising fabrication technology for high throughput patterning of the nanostructure. The operating procedure of nano-imprinting is simple: a hard mould, which includes nanostructures on its surface, is put on the wafer substrate with polymer material cast under fixed temperature and pressure, so a contrast with a fixed thickness in the polymer material is fabricated. It is reported that nano-imprinting technology has the ability to fabricate sub 10 nm structure,[18] but only for a simple process. The mould in nano-imprinting has the same function as the mask in photolithography and it has been made of Si or SiO_2. Besides, the mould surface contains a high density of nanoscale features, which increases the total surface area and results in a strong adhesion of polymer. Another importance is that the mould durability is related to the

stability of the coating layer, which is critical for the application of nano-imprinting in industry. The resist materials of nano-imprinting must be easily deformable under a fixed pressure, because imprinting makes a copy of the surface patterns by mechanical embossing. The simplicity of the nano-imprinting technique makes itself widely applied in various research fields. New methods based on mechanical printing (embossing) have been proposed as well. These unconventional pattern technologies have attracted extensive research attention for the low cost, scalability and new applications.

2.1.3 Etching methodologies

Wet chemical etching is widely applied in semiconductor industries because of the reliability and low cost. However, the minimum size of patterns is limited by the liquid phase etching reactions, thus dry etching was developed in the early 1970s.[19] Among these dry etching techniques, plasma etching have attracted much more applications for the moderate etch rate, high anisotropy, and selectivity.[20] Plasma etching is a combination process of chemical and physical etching, which makes it different from wet etching. The balance of this combination can be manipulated by the etching parameters (e.g., plasma gas composition, pressure, substrate temperature and biasing), the utilization of mask and passivation layer, and different plasma categories. However, when it comes to the fabrication of practical devices by plasma etching, challenges remain. First, a fully understanding of the plasma etching procedure is needed to make the processes and products more controllable. Second, it is hard to remove materials without affecting others for precision in nanoscale since the structures under research become multi-components. Although there are challenges, it is still valuable to explore new developments of nanotechnologies on this conventional plasma etching technique.

2.1.4 Self-assembly

Recently, self-assembly, a chemical process between particles resulting in a spontaneous fabrication of micro- and nanoscale structures,[21-23] attracts great interest as a

convenient and reliable methodology for fabricating ordered nanostructure arrays. The specific process could be controlled by the chemical interactions between NPs including capillarity (e.g., there are also other forces like magnetic, gravitational, hydrodynamic, electrostatic and surface adhesion, which are dominated by capillary forces when the size of structure decreases).[24, 25] As the technique develops, many different types of self-assembly are proposed, such as layer-by-layer, molecular, physical, chemical, and evaporation-induced self-assemblies.[26-30] Among these, the assemblies involved wet treating procedure have proven to be a versatile way to fabricate nanoscale structures at a high rate for the following advantages: low work temperature, controllable thickness of coating, and strong adhesion to the substrate, economic and experimental simplicity.[31] However, wet assembly has also its limits to satisfy industrial produce, such as weak bonding, low wear resistance, and defects problem. Nowadays, more and more researchers pay attention to fabricate large, highly ordered nanostructure arrays for achieving well chemical and physical applications. In this case, fully understanding of the chemical interaction related to the generation of two-dimensional (2D) or three-dimensional (3D) nano-arrays and the characteristics of the self-assembly process is thus specifically necessary.

2.1.5 Template-directed techniques

In general, template-directed techniques refer to the techniques that utilize the template to regulate the synthesis of the nanomaterials or the dismounting of bulk materials into the desired nanostructures. Thus, both top-down methods (e.g., chemical etching, ion milling, etc.) and bottom-up methods such as electrochemical deposition (ECD), atomic layer deposition (ALD) could be combined with the templates, thereby yielding a sort of powerful and universal techniques to fabricate nanostructure arrays in large scale with a relatively low cost, in comparison with the lithography technologies. In principle, any substance with nano-patterned features, including natural and artificial nanostructured materials, can be used as a template for the construction of nanostructure arrays. Though various nano-patterned

architectures have been extensively investigated, the most accessible and popular template used in nanostructure fabrication is the AAO template.

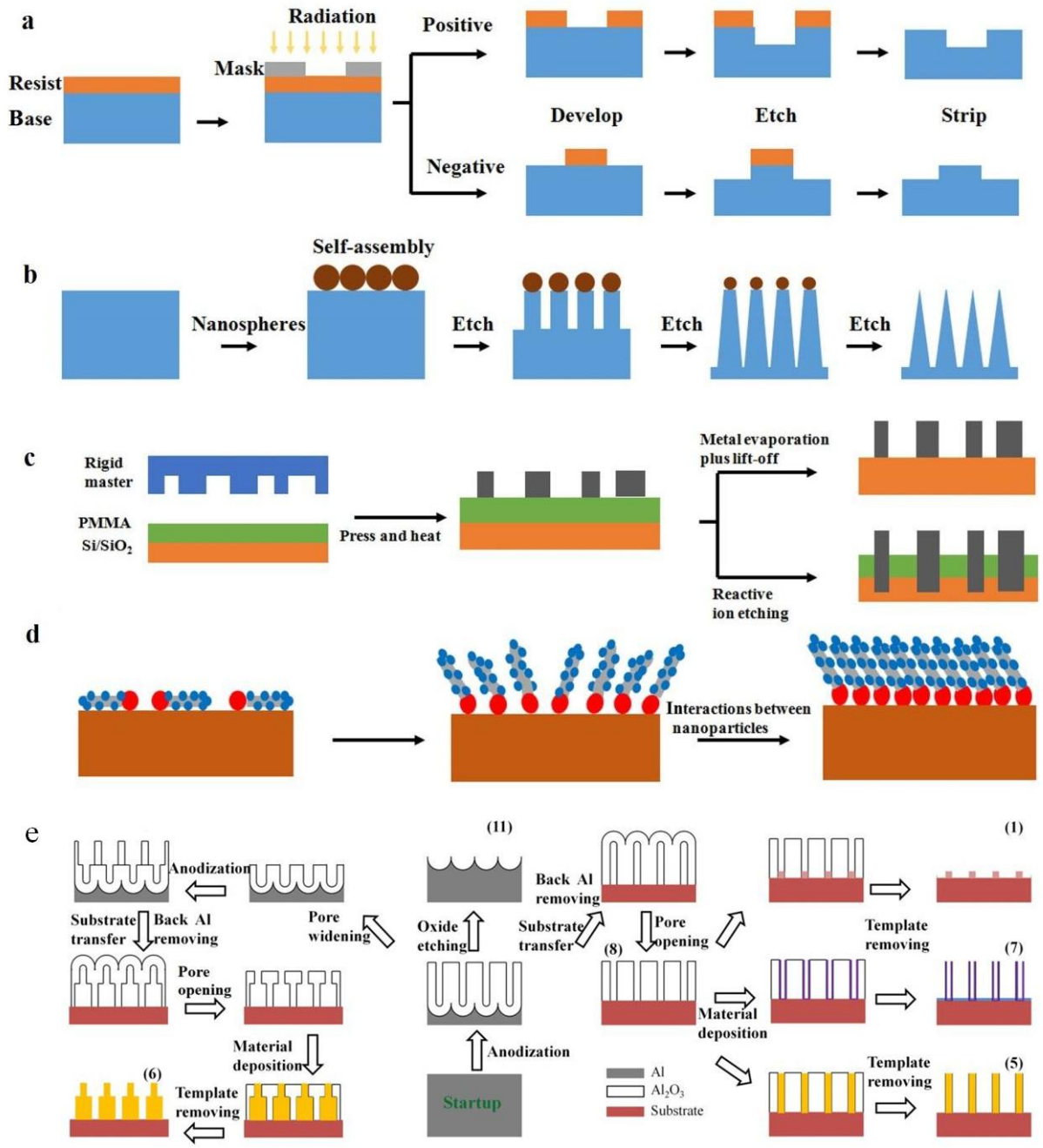

Figure 2-1. Cartoons for fabrication process of nanostructures. (a) Schematic representation of a procedure for optical lithography. (b) Schematic procedure of fabricating nanostructure arrays by colloidal lithography. (c) Schematic overview of the process of nano-imprinting. (d) Schematic representation of the procedure for self-assembly. (e) Detailed procedures for realizing a series of ordered nanostructure arrays using template-directed techniques.

2.1.6 Comparison between nanostructure fabrication techniques

Collectively, a large variety of nanostructure arrays could be realized by the above techniques and each technique has its own advantages and limitations, as summarized in Table 1. To manipulate the geometric characteristics of the nanostructure arrays freely, scalablely, broad material applicably and cost effectively, lots of efforts still need to be performed. In consideration of the prominent advantages such as cost-effectiveness, high-resolution and uniform structures, we will focus on the AAO template technique to construct various periodic nanostructures in this dissertation.

Method	Application	Requirement	Cost	Resolution (nm)	Disadvantages
AAO template	nanoparticle, nanowire, nanotube, nanopore	Normal lab conditions	Low-cost	<10	Few pattern defects
Colloidal crystal template	nanoparticle, nanoring, nanocone, nanopore	Normal lab conditions	Low-cost	<5	More pattern defects
Optical lithography	nanopore, nanoparticle complicated 2D nanostructures	Optical lithography system, clean room	High-cost	<10	Multiple steps; incompatible with organic solvent
EBL	nanopore, nanoparticle, complicated nanostructure	EBL system in clean room	Expensive	<10	Time-consuming, small area and low throughput
Colloidal Lithography	nanoparticle, nanocone, nanowire	Normal lab conditions	Low-cost	50	Non-uniform
Nano-imprinting	nanoparticle, nanodisk	Normal lab conditions	Low-cost	20-30	More pattern defects
Plasma etching	nanodent nanowire	High vacuum system, clean room	High-cost	30	Multiple parameters; weak controllability
Self assembly	nanoparticle	Normal lab conditions	Low-cost	<5	More pattern defects, weak controllability

2.2 Anodic aluminum oxide Template

Since 1995, when Masuda and co-workers reported that well-ordered AAO nanoporous structure could be attained by anodizing aluminum metal in acidic electrolytes, AAO template has inspired a wave of fashion for fabricating highly-ordered nanostructure arrays. Such AAO template has a self-ordered, honeycomb-like and highly-oriented porous structure in nanoscale, with tunable pore size, density, interpore distance, and distribution topologies. By adjusting the anodization conditions (e.g., choosing different electrolytes, applying different anodic biases, etc.), self-ordered AAO templates with tunable pore diameters of about 10–400 nm and densities in the range 10^8–10^{10} pores cm^{-2} can be prepared.[32] Combining with an imprinting process, long-range order of AAO templates with tunable pore distributions and profiles could be conveniently realized.[33, 34] Thereby, during the last decades, AAO template has been extensively exploited in the fabrication of diverse nanostructure arrays in the form of nanopores,[35-37] NPs,[38, 39] NCs,[40, 41] NWs[42, 43] and NTs[44, 45]. In addition, the developed pulse anodization, as well as the alternative usage of mild and hard anodization for one specimen, enables the fabricated AAO templates with periodically modulated nanopore diameters along the pore axes, supplying another opportunity for tailoring the morphological parameters of the as-fabricated nanostructure arrays.[46, 47] Due to the high compatibility of the AAO template with a broad scope of techniques for material synthesis, many categories of materials can be prepared into nanostructure arrays, like metal, semiconductors, wide band gap oxides, polymers, and organic materials. To be more important, by manipulating the sequences of synthesizing various materials in the AAO template, nanostructure arrays with multi-components and multi-segments could also be attained.[48] Thus, the AAO template provides a good scaffold to prepare nanostructure arrays for real device fabrications.

2.2 .1 Formation mechanism of AAO templates

Considering the significance of the AAO template, it is necessary to understand the formation of AAO in detail and this area is lack of specific theoretical attention. Figure 2-2a and b schematically show the ideal structure of anodic alumina membrane, which consists of a large number of parallel pores perpendicular to the aluminum substrate.[49] Each pore cell can be geometrically defined by the pore diameter, pore wall thickness, pore length, interpore distance, and porosity. The biggest advantage of the AAO template is the high tunability of these geometric parameters, which are governed by the anodizing electrolyte, potentials and time. As shown in Figure 2-2c, at the beginning of the anodization, a thin compact oxide layer grows to cover the whole Al surface (stage I). Thickening the barrier oxide leads to an increase in local stress. When the thickness of the compact oxide reaches a certain value, local crack happens, resulting in a path for the acid solution which penetrates to the Al foil under the oxide barrier (stage II). The internal stress resident in the defective oxide barrier promotes the self-organization of the neighboring pores (stage III). As the anodization continues, the regularity of the pore arrays improves. Normally the regularity of anodic alumina is proportional to the anodization time. After about 10 hours, an alumina membrane with disordered pores on the top and ordered pores at the bottom is obtained (stage IV). Due to the disordered nature of the template on the top, we usually etch this layer away and leave Al foil being textured with an ordered array of semispherical concaves (stage V). Then another procedure for anodizing is performed to acquire a well ordered Al_2O_3 porous structure (stage VI). This so called two-step anodization process was firstly proposed by Masuda and Satoh.[50] Considering the time-consuming of the first anodization procedure and the difficulty of manipulating the distribution of nanopores, which are hexagonally distributed in nature, in 1997, Masuda and coworkers developed a so-called ‘pretexturing’ process, which used a silicon carbide mold with ordered array of convexes to stamp an Al foil before anodization.[51] In this way, the time-consuming first step anodization process could be

omitted and the second anodization step can be directly carried out. More importantly, the profiles and distributions of the resulted Al_2O_3 nanoporous array could be highly manipulated by the geometric parameters of the convexes in the mold.

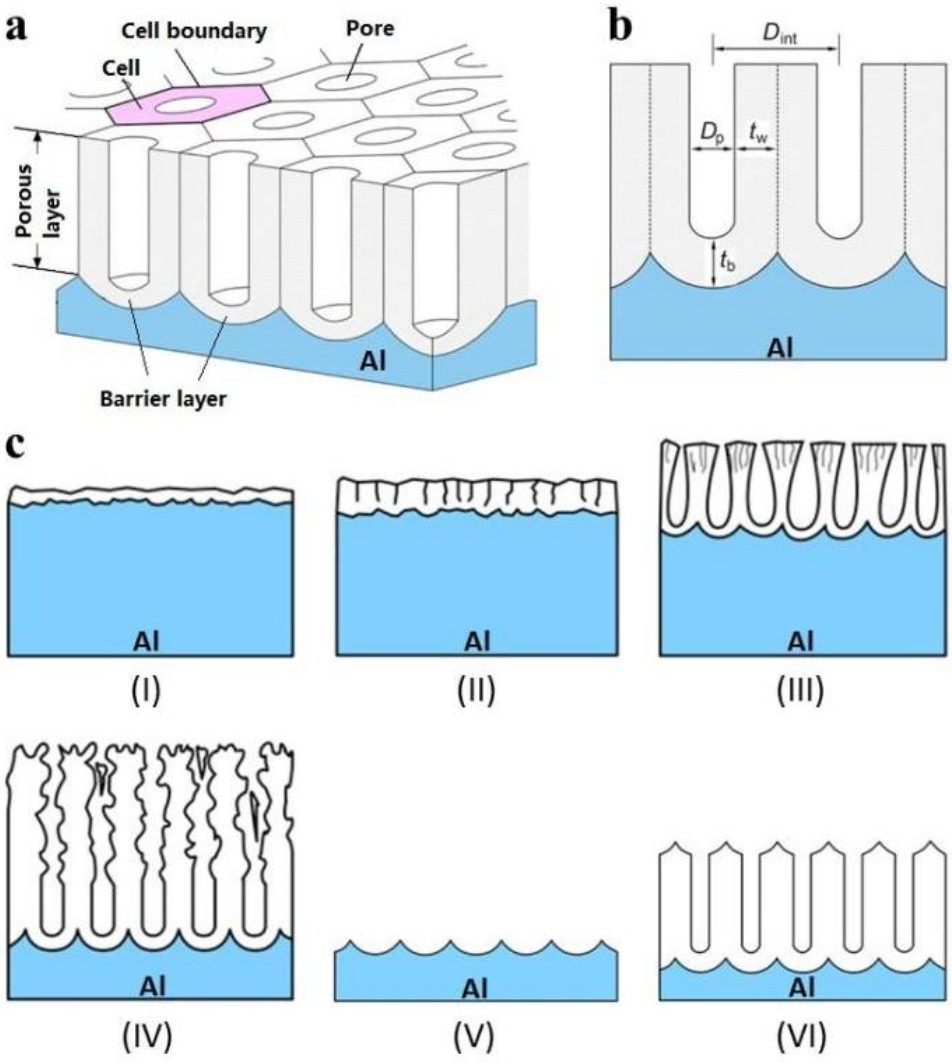

Figure 2-2. Schematic drawing for AAO templates. (a, b) Schematic structure of a representative AAO template, showing the parameter definitions. (c) Schematic of the two-step anodization process for realizing AAO template.

It should be mentioned that even using two-step anodization processes, it is still tough to get a large area of nanopore arrays without defects. In order to obtain larger-areal and highly ordered anodic alumina membrane, treatments like annealing and electropolishing the Al foil have to be performed. Such treatments are helpful to remove resident stress and

defects in the Al foil. To understand the anodization procedure fundamentally, COMSOL Multiphysics software was used to simulate the 3D electric field distribution in the Al foil and barrier oxide. The simulation was based on steady-state current continuity equation, excluding the potential drop in the electrolyte and the electrode double layer at the electrolyte/metal interface. Figure 2-3a-d show the electric field distribution in Al film at the initial stage of the first step anodization, where (a) and (b) indicate that the ideally defect-free sample has a uniform electric field distribution and a relatively small value ($1.17*10^8$ V m^{-1}) through the whole Al foil. In contrast, the defect sample shows a nonuniform electric field (Figure 2-3c and d). The electric field at the corners of the defects is several orders higher than that at other positions. The fluctuant electric field will result in different oxide barrier growth rates and local stresses, finally affecting the regularity of the pore arrays.

Figure 2-3e-h show the electric field distribution in the Al foil at the steady pore formation stage of the second step anodization. For this surface-textured Al foil, the electric field of each cell at the initial stage is periodic, with the intensity at the bottom of the nanocaves much bigger than that at the top, as shown in Figure 2-3e and f. Such electric field concentration at the bottom of the pores during the pore formation indicates that the oxide dissolution mainly occurs at the bottoms of the pores. According to the field-assistant oxide dissolution theory,[52] the electric field promotes the immigration of ions through the oxide barrier. The electric field along the sidewall and on the top surface of the barrier layer is almost zero, demonstrating that there is almost no dissolution of oxide on the wall and the top surface for the procedures with the same anodizing conditions. This results in a highly-uniform and vertically-distributed Al_2O_3 nanoporous arrays (Figure 2-3g and h).

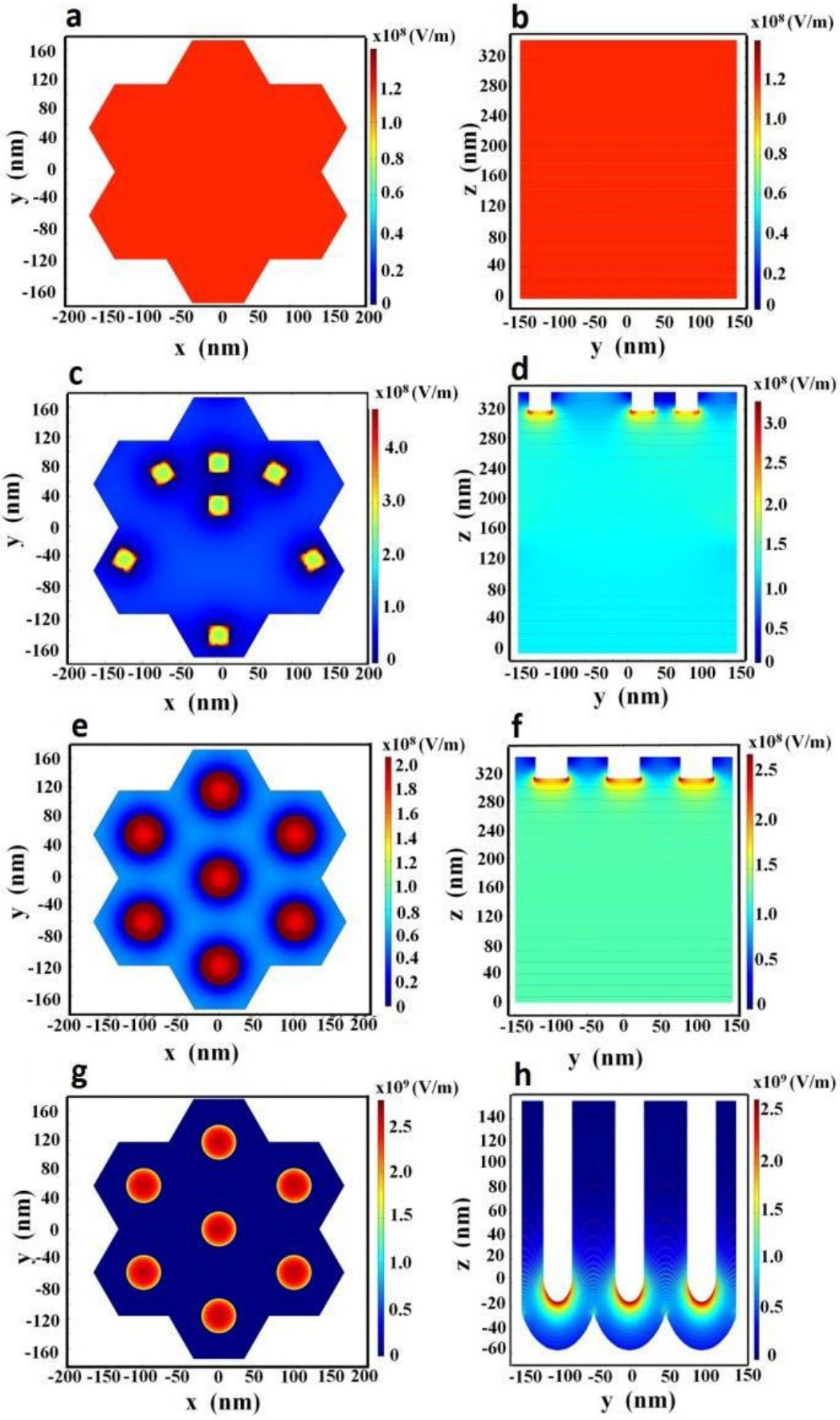
a
x10⁸ (V/m)
y (nm)
x (nm)
b
x10⁸ (V/m)
z (nm)
y (nm)
c
x10⁸ (V/m)
y (nm)
x (nm)
d
x10⁸ (V/m)
z (nm)
y (nm)
e
x10⁸ (V/m)
y (nm)
x (nm)
f
x10⁸ (V/m)
z (nm)
y (nm)
g
x10⁹ (V/m)
y (nm)
x (nm)
h
x10⁹ (V/m)
z (nm)
y (nm)

Figure 2-3. Electric fields for Al anodization. (a, b) Top and cross-sectional views of the electric field distribution of polished Al foils at the beginning of the first anodization step. (c, d) Top and cross-sectional views of the electric field distribution of unpolished Al foils at the beginning of the first anodization step. (e, f) Top and cross-sectional views of the electric field distribution of Al foils with nano-textured surface at the beginning of the second anodization step. (g, h) Top and cross-sectional views of the electric field distribution of alumina membrane at the stable stage of hole formation. The voltage applied in all these samples is 40 V and the corresponding interpore distance is about 110 nm.

2.2.2 Nanostructure array fabricated with AAO templates

Practically, a large diversity of ordered nanostructure arrays, which have been broadly employed in energy-related applications, could be realized by these AAO template-directed methods. As summarized in Figure 2-4, the profiles, dimensions and distributed regularities of these nanostructure arrays could be well controlled. Even complicated nanostructure arrays, like multi-segmented and multi-profiled nanostructure arrays, could also be attained by tuning the formation procedure of template and the synthetic process of the targeting materials. These ordered nanostructure arrays behave as scaffolds to construct energy-related devices and are of great merit in regulating the energy converting reactions and optimizing the corresponding performances.

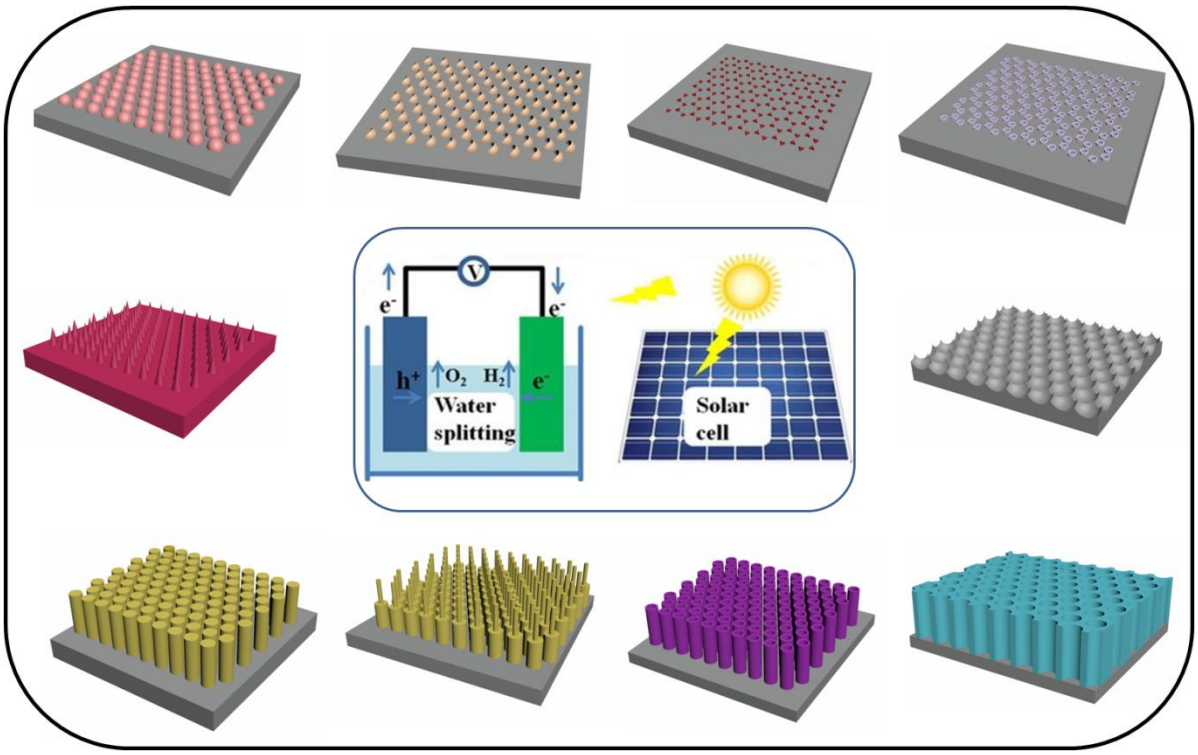

Figure 2-4. Schematic of ordered nanostructure arrays that could be realized via template-directed techniques and the according applications to energy-related devices.

2.3 Progress in ordered nanostructures for solar energy conversion

Generally, the process of solar energy conversion mainly includes three steps: photon absorption, charge carrier generation and transport, as well as final product (electricity or hydrogen) collection. Though the devices for solar energy converting are of large diversity depending on the specific active materials, configuration of the device architecture with ordered nanostructure arrays provides a universal methodology to improve the overall efficiency from all these detailed energy converting steps. In principle, the ordered nanostructures with a higher surface-to-volume ratio could provide a larger active area for scattering and absorbing the incident light, promoting the separation of photo-generated charges and reducing the diffusion distance of charge carriers before being collected, thus beneficial for improving the overall efficiencies. However, the enlarged surface area would induce a large density of surface states, which would deteriorate the device performance.

How to balance the two issues is crucial for the device design, which is largely influenced by the active materials employed.

PEC energy conversion refers to the procedure that utilizes photo energy to drive electrochemical reactions and collect the final products for energy utilization. Water splitting cells utilize the absorbed photons by the semiconductor electrodes to excite free charge carriers, which will subsequently initiate water oxidation or reduction reactions at the interface with aqueous solution and convert water molecules to the final products, oxygen and hydrogen. In particular, hydrogen is esteemed as the cleanest fuel energy since the only waste product upon utilization is water. Since the pioneering work by Honda et al. in 1972,[53] water splitting research has attracted huge attention. Specifically, the recent research work from Lewis et al. pushed this area to a new high. The authors investigated a series of crystalline semiconductors (e.g. Si, GaAs and GaP) systematically for water splitting.[54, 55] It was demonstrated that Si photoanodes exhibited continuous oxidation of water to O_2 for more than 100 hours at photocurrent densities of >30 mA cm^{-2} and ~100% Faradaic efficiency. TiO_2-coated GaAs and GaP photoelectrodes exhibited photovoltages of 0.81 and 0.59 V as well as photocurrent densities of 14.3 and 3.4 mA cm^{-2}, respectively, for water oxidation.[55]

In the construction of the photoelectrodes for water splitting, nanostructuralizing the device architecture is a wise choice, since the nanostructures could provide a good platform to enhance the absorption efficiency by the scattering effect and to drive the PEC reactions extensively though the huge surface area. Herein, the devices are introduced according to the morphology of the nanostructures from 0D to 3D nano arrays. Figure 2-5a presents a SEM image of the Au ND arrays (0D nano arrays) for the fabrication of Au/TiO_2 photoelectrode. The Au ND arrays were prepared by an AAO involved nano-imprinting technique and the TiO_2 layer was synthesized by a dip-coating procedure. The photocurrent of the as-prepared photoelectrode was realized over 0.7 mA cm^{-2} at 1.1 V vs SHE, much higher than that from the pure TiO_2 electrode. In addition, the high hydrogen evolution rate yielded a high Faradaic

efficiency of 94.9% (Figure 2-5b and c). This result indicates that metallic nanostructure arrays could boost the PEC reactions substantially due to both the scattering and SPR effects.[56] Lee et al. designed a plasmonic water-splitting cell, which was functioned by illuminating a dense array of aligned gold NRs capped with TiO_2 (1D nano arrays), forming a Schottky metal/semiconductor junction which collected and conducted the hot electrons to an unilluminated platinum counter-electrode, where hydrogen gas evolved. The results demonstrated that 95% of the effective charge carriers derived from surface plasmon decay to hot electrons.[57] Afterwards, the same group reported an efficient, autonomous solar water-splitting device based on a gold NR array, in which each rod was decorated with TiO_2/Pt on the top for hydrogen generation and cobalt-based oxygen evolution catalyst on the side. In this case, such unique core/shell NRs integrated both a photocathode and a photoanode and could generate H_2 and O_2 synchronously without any external wiring, producing 5×10^{13} H_2 molecules per cm^2 per s under 1 sun illumination, with unprecedented long-term operational stability.[58] To be more interesting, Wang et al. fabricated photoanode based on multi-segmented CdS-Au NW arrays with a sequential and highly tunable configuration. In combination with the surface plasmon effects of each Au nanounit that could greatly enhance the absorption efficiency of the photoanode, the photocurrent at 0 V vs Ag/AgCl was realized as high as 10.5 mA cm^{-2} and presented long-term stability (Figure 2-5d-f).[59] In addition, Au NPs sensitized ZnO NR/nanoplatelet core/shell arrays were employed for water splitting as well and a high photocurrent at 0.6 V vs. Hg/Hg_2Cl_2 was realized as 2 mA cm^{-2}. [60]

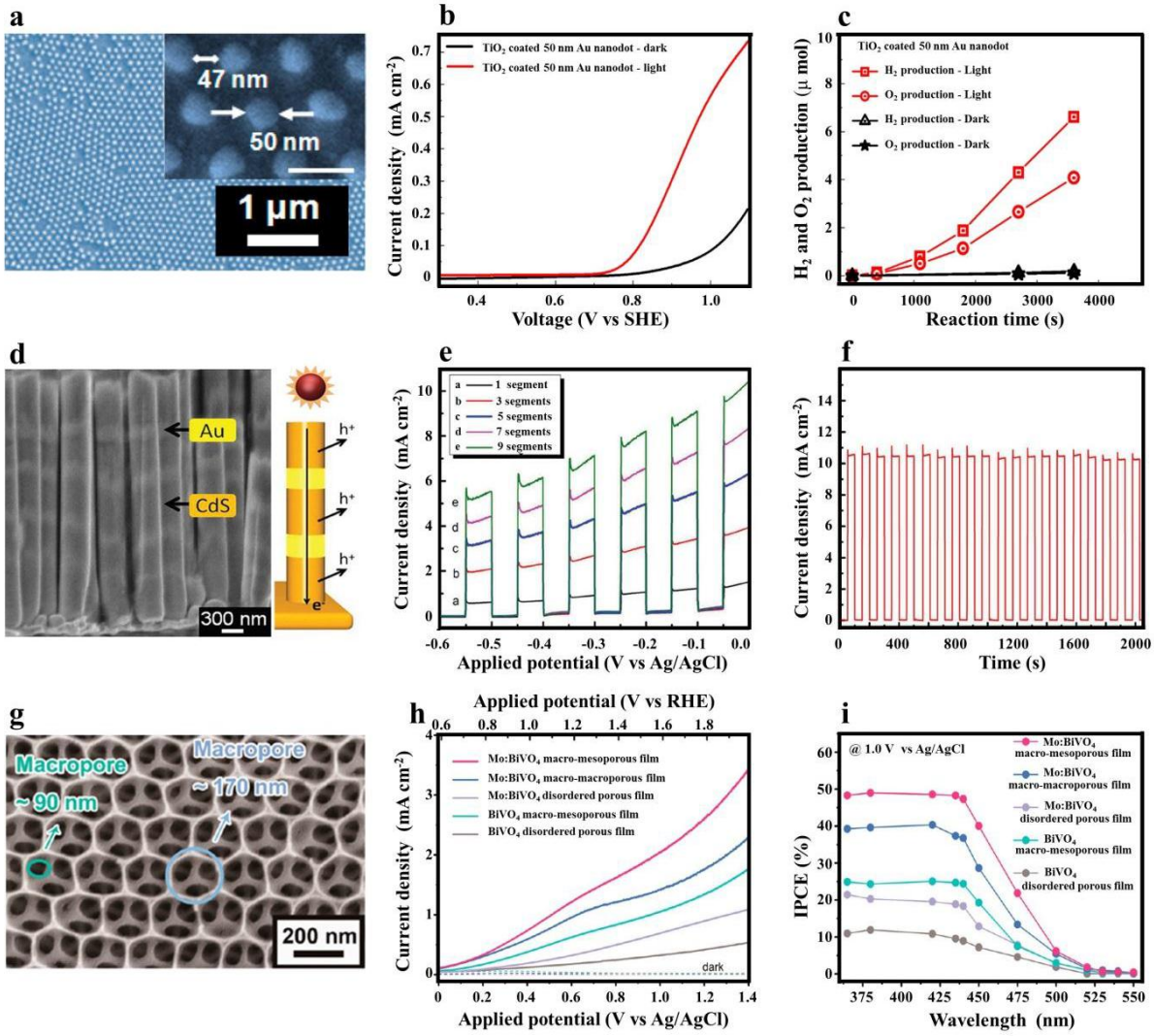

Figure 2-5. Structural and PEC characterization of photoelectrodes. (a) SEM images of prepared Au ND arrays; (b) J−V profile with light and dark condition from 0.3 to 1.1 V (vs SHE) at a scan rate of 5 mV s^{-1} for water splitting; (c) hydrogen and oxygen production vs reaction time on TiO_2-coated 50 nm Au ND arrays for water splitting at an applied potential of 0.897 V (vs SHE).[56] (d) SEM images of the multi-segmented CdS-Au NR arrays with nine segments and schematic diagram of the multi-segmented CdS-Au NR; (e) linear sweep voltammogram curves of the multi-segmented CdS-Au NR arrays with different number of segments in the range from one to nine; (f) stability test of the nine segments multi-segmented CdS-Au NR arrays under the illumination of AM1.5 at a potential of 0 V vs Ag/AgCl.[59] (g) Typical SEM images of Mo:$BiVO_4$ 3D ordered macro-macroporous architectures; (h) photocurrent density-potential curves (solid line) and dark-current density-potential curves

(dashed line) of various films (scan rate = 10 mV s^{-1}); (i) incident photon to charge carrier efficiency (IPCE) spectra of various films at 1.0 V vs Ag/AgCl.[61]

TiO_2 and ZnO are semiconductors with a large band gap, which are not suitable to absorb the photons in the visible range. Semiconductors with narrow band gap have been largely fabricated into 1D nanostructure arrays and applied in water splitting. By removing the as-prepared AAO template on Al to leave an Al nanospike array behind, Qiu et al. fabricated Al/Ti/Pt/FTO/α-Fe_2O_3 NC ordered arrays. The resulting photoelectrode presented an impressively high absorption efficiency of around 100% at 700 nm. With electrodeposited CoPI on the surface, the photocurrent was measured as 4.36 mA cm^{-2} at 1.60 V vs reversible hydrogen electrode (RHE), about three times of that for a planar photoelectrode.[62] Using similarly protocol, the same group fabricated photoelectrode based on FTO/Au/Ti-α-Fe_2O_3/CoPI NC arrays. Remarkably, a high photocurrent density of 3.39 mA cm^{-2} (at 1.23 V vs RHE) could also be obtained, due to the double enhancements by the catalyst and gold reflection layers.[63] With the assistance of AAO template, Li et al. prepared cobalt phosphate-modified barium-doped tantalum nitride NR photoanode, which yielded a maximum solar energy conversion efficiency of 1.5%, more than three times higher than that of state-of-the-art single-photon photoanodes.[64] Additionally, through the incorporation of a hematite NR array into a plasmonic gold mesh array, PEC water splitting performance was dramatically improved, leading to an approximately ten-fold increase in the photocurrent at a bias of 0.23 V vs Ag/AgCl under simulated solar radiation.[65]

Alternatively, perfectly ordered Si NW array has proven to be another good candidate for PEC energy applications. Using a copper-catalyzed, vapor-liquid-solid-growth process, Boettcher et al. grew ordered arrays of crystalline P type silicon (p-Si) microwires on p^+-Si (111) substrates. Using these wire arrays as photocathodes in contact with an aqueous methyl viologen^{2+} electrolyte, energy conversion efficiencies of up to 3% were observed for monochromatic 808-nanometer light at fluxes comparable to solar illumination.[54]

Subsequently, the same group loaded earth abundant Ni-Co catalysts on the surface of Si NW arrays. The corresponding electrodes yielded a V_{OC} of 0.46 V vs RHE, a J_{SC} of 9.1 mA cm^{-2}, and thermodynamically based energy-conversion efficiencies of 1.9% under simulated 1 Sun illumination.[66] Furthermore, the authors developed an advanced photoelectrode constructed by core/shell tandem junction n–p+-Si/ITO/n-WO_3 NW arrays and the corresponding devices exhibited a V_{OC} of −1.21 V vs $E^{0'}(O_2/H_2O)$, demonstrating additive voltages across the individual junctions, which is good for hydrogen evolution.[67] Additionally, GaAs NW arrays and Si/GaP NW arrays, which exhibit decent PEC properties, were also investigated deeply.[68, 69] In particular, using ALD to grow hematite on vertically aligned Si NW array and form a dual-absorber system, a photocurrent turn-on potential as low as 0.6 V vs RHE was realized.[70]

In the aspect of the surface area, 3D hierarchical nanostructure arrays are superior over the conventional 1D nanostructure arrays. Hwang et al. synthesized InGaN NWs on Si NW arrays. Electrochemical measurements showed that the photocurrent density for the electrode with hierarchical Si/InGaN NW arrays was increased by 5 times compared to the photocurrent density of the electrode with InGaN NW arrays grown on planar Si (1.23 V vs RHE).[71] Meanwhile, recent research on building up 3D nanoporous arrays has attracted remarkable focus. Zhou et al. designed nanoengineered 3D ordered macro-mesoporous architecture of Mo:$BiVO_4$ through a controllable colloidal crystal template method with the help of a sandwich solution infiltration method and adjustable post-heating time. A superior photocurrent density as high as 2.0 mA cm^{-2} at 1 V vs Ag/AgCl was achieved. The corresponding IPCE was close to 50% (Figure 2-5g-i).[61] Other materials like SnO_2, Fe_2O_3, and WO_3 etc. have been also made into the nanoporous structure for water splitting and the results were demonstrated to be promising.[72-74] Furthermore, Coridan et al. deposited nanoporous WO_3 on well-ordered Si NW arrays through the assistance of polystyrene sphere template. Comparing with conformal, unstructured WO_3 shells on Si microwires, the hierarchically structured photoanodes exhibited enhanced near-visible spectral response behavior, attributing

to the increased light absorption and reduced distances over which photo-generated carriers were collected.[75] Generally speaking, the contact of semiconductor with electrolyte governs the reactions in the PEC energy conversion process. Making the semiconductor layer into nanostructure array supplies a huge area for the PEC reactions, which is beneficial for improving the overall efficiency. Moreover, considering the long transport route from the top surface of nanounit to the bottom electrode, nanostructuralizing the electrode in an order way could be helpful to maintain the large surface area without thickening the semiconductor layer.

CHAPTER 3. Experiments and simulations

All experiments and simulations in this thesis were conducted according to the protocols outlined in this chapter. The highly-ordered nanostructure array and the resulting devices were constructed by a combination of the above-mentioned AAO method and various synthesis techniques involving ALD, ECD, and physical vapor deposition (PVD). The compositional and geometrical details were characterized by field emission scanning electron microscopy (SEM), transmission electron microscopy (TEM), X-ray powder diffraction (XRD), and energy-dispersive X-ray spectroscopy (EDX). The optical and PEC performance were measured by UV-Vis absorption spectroscopy, electrochemical workstation, and QEPVSI-b quantum efficiency measurement system. The simulation software packages of COMSOL Multiphysics and Finite Difference Time Domain (FDTD) were exploited to shed light on the optical and electrical details at the nanoscale.

3.1 Synthesis techniques

3.1.1 Atomic layer deposition

ALD is a technique on the basis of the sequential use of a gas phase chemical process to realize thin film deposition. Unlike CVD in which precursors are present simultaneously in the reactor, in ALD the precursors are supplied in a series of sequential and non-overlapping pulses. During each pulse, the precursor molecules react with the surface in a self-limiting way, and the reaction terminates after all the reactive sites on the surface are consumed. This this specific technique is governed by the nature of the precursor-surface interaction. Different from ECD, PVD and CVD where the material growing orientation is determined by the flow direction of the ions, vapors or precursors and it is not easy to grow uniform and rigid film on completed nanostructured substrate, ALD shows an amazing ability to grow ultrathin uniform film all over the substrate, no matter how rough the substrate is. Thus, we can duplicate precisely the morphology of the template and fabricate the targeting material to NDs, NTs,

NWs, and nanopores etc. Concerning the slow layer growing procedure and the high vacuum operation, the cost of ALD is high, but it is still worthy of using such advanced technique to fabricate precisely controlled nanostructure for energy-related applications.

3.1.1.1 Atomic layer deposition of TiO_2

ALD reactions were carried out using Picosun SUNALETM R150 ALD System. The recipes for the growth of TiO_2 NTs and Pt NPs are the same as our previous reports.[76, 77] Titanium (IV) chloride ($TiCl_4$) and distilled-water were used as the precursors of TiO_2, while Trimethyl (methylcyclopentadienyl) platinum (IV) ($Pt(MeCp)Me_3$) and oxygen were used as the precursors of Pt, respectively. One typical TiO_2 growth cycle consists of: $TiCl_4$ (0.1 s) – N_2 purge (5 s) – H_2O (0.1 s) – N_2 purge (5 s). TiO_2 growth rate is about 0.05 nm per cycle at 300 °C.

3.1.1.2 Atomic layer deposition of SnO_2

Tin (IV) chloride ($SnCl_4$, Sigma-Aldrich) and distilled-water (H_2O) are used as the precursors of Sn and O, respectively. The reactor is maintained at a temperature of 250 °C and the N_2 carrying gas is kept at 100 sccm during the deposition process. The recipe of SnO_2 growth is as similar as that described in TiO_2. The growth rate of SnO_2 is about 0.3 nm per cycle. The pulsing time of $SnCl_4$ and H_2O are 0.5 s and 0.1 s, respectively. The N_2 purging time is 5 s.

3.1.1.3 Atomic layer deposition of Pt

One typical Pt growth cycle consists of $Pt(MeCp)Me_3$ pulsing (1.3 s) – low N_2 filling (30 s) -N_2 purging (18 s) – O_2 pulsing (1.3 s) – low N_2 filling (30 s) – N_2 purging (18 s).

3.1.2 Electrochemical deposition

ECD is the process that uses electric power to initiate the electrochemical reactions of the ions in the solution and deposit the targeting materials on the working electrode. In principle, nearly all of the substances that can be synthesized in a solution-based procedure could be realized via ECD procedure, like metals, semiconductors and even polymers etc. By

placing the template on the working electrode and controlling the detailed deposition procedures, including depositing time, potentials and precursors of the targeting materials, a large variety of ordered nanostructure array could be realized, like ND array, NW array, NT array and nanoporous array. Significantly, by manipulating sequence of depositing different materials, nanostructure arrays with multi-segmented and core-shell configurations could also be easily realized. ECD is a cost-less and convenient technique but the resulting materials are usually amorphous or polycrystalline. To improve the photoelectric properties of the as-grown materials, a subsequent annealing procedure is often involved.

3.1.2.1 Electrochemical deposition of Ni

The Ni ECD was performed under a constant current of 5.0 mA/cm^2 in an aqueous electrolyte (0.38 M $NiSO_4$, 0.12 M $NiCl_2$, and 0.5 M H_3BO_3).

3.1.2.2 Electrochemical deposition of Au

A conventional three-electrode electrochemical cell was chosen for Au deposition. The reference and counter electrodes were Ag/AgCl in saturated KCl solution and Pt wire, respectively. The Au deposition was conducted in Au plating solution (Orotemp 24 Rack) under a potential of -0.95 V.

3.1.2.3 Electrochemical deposition of CdS

CdS was cathodically electrodeposited under a constant current of 1.0 mA/cm^2 at 130°C in a two-electrode electrochemical bath where a Pt mesh and the conductive targets served as the counter electrode and working electrode, respectively. The electrolyte was made by dissolving 3.6 g $CdCl_2$ and 1.6 g S in dimethyl sulfoxide (DMSO). Thermal treatment of the sample was carried out in ambience at 350°C for 30 minutes with 5°C/min heating rate and then naturally cooled to room temperature.

3.1.3 Physical vapor deposition

PVD employs physical process (heating, sputtering etc.) to vaporize the targeting material and then deposit it on the substrate. In principle, more easily the materials can be

vaporized, more feasibly to be prepared by PVD techniques. The materials that are usually used in PVD involve metals, organic molecules and even metal nitrides etc. In combination with the templates, these materials can be fabricated into any nanostructural morphology that can be realized by CVD procedures. PVD is more environmentally friendly than CVD, due to no waste gas in the procedure. However, PVD is usually operated in high vacuum and temperature conditions, thus giving rise to a relatively high cost. In addition, the resulting films or nanostructures made by PVD are usually polycrystalline and it is not easy to prepare single crystals via PVD.

3.2 Device measurements

3.2.1 PEC measurement for CdS photoanode

Oriel solar simulator (300 W Xe lamp, AM 1.5 global filter) was taken as the simulated light source and calibrated to AM 1.5G by a standard Si photodiode (Model 818, Newport). The photocurrent density was measured using a three-electrode electrochemical cell, in which $Na_2S/Na_2S_2O_3$ (0.2 M/1 M) aqueous solution served as the electrolyte, the CdS/Au PTPs acted as the working electrode, the Pt mesh worked as the counter electrode, and an Ag/AgCl electrode functioned as the reference electrode. IPCE measurements were performed using the same electrolyte in a two-electrode electrochemical cell under no external bias with QEPVSI-b Quantum Efficiency Measurement System (Newport).

3.2.2 PEC measurement for TiO_2-Au Janus hetero-nanostructure photoanode

Oriel solar simulator (150 W Xe lamp, AM 1.5 global filter) was used as the simulated light source and calibrated to AM 1.5G by a standard Si photodiode (model 818, Newport). The photocurrent density was measured using a three-electrode electrochemical cell in a 0.5 M Na_2SO_4 electrolyte (pH = 6.8). The applied biases are subsequently converted to the RHE scale using the Nernst equation:

$$E_{RHE} = E_{Ag/Agcl} + E^{0}_{Ag/Agcl} + 0.059\text{pH} \quad (1)$$

where the E_{RHE} is the converted bias versus RHE, the $E_{Ag/AgCl}$ is the applied bias measured against the Ag/AgCl reference electrode, and the $E°_{Ag/AgCl}$ is the standard potential of Ag/AgCl at 25 °C (0.1976 V). IPCE measurements were performed using the same electrolyte in a two-electrode electrochemical cell under no external bias with the QEPVSI-b quantum efficiency measurement system (Newport).

The photocatalytic H_2-production experiments were performed in a 300-mL cylinder-shape quartz reactor. All glassware was rinsed thoroughly with Milli-Q water prior to use. The samples were immersed in a mixed aqueous solution of v/v 20% methanol and magnetic stirring (500 rpm) was applied throughout the experiment. The temperature was controlled at ~28 to ~33 °C by a cooling fan. For complete removal of O_2, the solution was purged with argon for 1 h before illumination. Sampling was processed with 1.0 mL gas intermittently through the septum and quantified with an Agilent Micro-GC gas analyzer (3000A or 490) equipped with two columns and two TCD detectors. Experiments on the direct photocatalytic reduction of a model acceptor molecule, methylene blue (MB), were performed under conditions similar to those above, but in addition 1 mL 0.6 mM aqueous MB solution was injected into the quartz reactor before photocatalysis was initiated. Before illumination, the immersed sample was placed in the dark under constant stirring for 90 min to reach adsorption/desorption equilibrium. The reaction process was monitored by measuring the MB concentration/absorbance using a Varian Cary 5000 UV–vis-NIR spectrophotometer.

3.2.3 Solar thermoelectric generator experiment

We exploited commercially available thermoelectric generators (TEG-127009-30X34 made by P&N Technology Co., Ltd) to perform the solar thermoelectric generator experiment. The thermoelectric generator was 30 mm in width and 34 mm in length. The hot side of the thermoelectric generator was illuminated by a solar simulator (Newport, 67005), and

meanwhile the other side was exposed to the atmosphere. The radiation power density of the solar simulator was calibrated by the optical power meter (Newport, 1916-R, with a detector, 818-UV). The Ni SPhC of 1-inch diameter was attached to the hot side of the thermoelectric generator by thermal transfer compound.

The absorbed energy P_a and reemissive energy P_e of a solar absorber can be described as follows [78]:

$$P_a = \int \alpha(\lambda) \times S_{solar}(\lambda) d(\lambda) \tag{2}$$

$$P_e = \int \varepsilon(\lambda) \times S_{bb}(\lambda) d(\lambda) \tag{3}$$

where the wavelength-resolved $S_{solar}(\lambda)$, $\alpha(\lambda)$, $\varepsilon(\lambda)$ and $S_{bb}(\lambda)$ represent AM 1.5G solar spectrum, the absorption spectrum of the solar absorber, the spectral remission spectrum of the absorber, $S_{bb}(\lambda)$ is the black body emittance spectrum, respectively. $S_{bb}(\lambda)$ is represented as

$$S_{bb} = \frac{2\pi hc^2}{\lambda^5 \left[\exp\left(\frac{hc}{kT} \right) - 1 \right]} \tag{4}$$

where T is the working temperature, k is the Boltzmann constant, h is the Planck constant, and c is the light speed in vacuum. Based on Kirchhoff's law of thermal radiation, the emittance $\varepsilon(\lambda)$ is identical to the absorbance $\alpha(\lambda)$ for a thermally stable system. So the solar-to-thermal conversion efficiency of a solar absorber can be described by

$$\eta = \frac{N \times P_a - P_e}{N \times \int s_{solar}(\lambda) d(\lambda)} \tag{5}$$

N is the radiation concentration.

3.2.4 Solar steam generation experiment

A piece of Ni SPhC was dipped into water in a custom-built glass cell with dimensions of 15 mm × 15 mm × 15 mm. The dimension of Ni SPhC in water is about 14 mm × 14 mm.

The solar beam from a solar simulator (Newport, 67005) illuminated Ni SPhC under the power density of ~1 kW m^{-2}. The power density of the illumination intensity was calibrated by an optical power meter (Newport, 1916-R, with a detector, 818-UV). The weight loss over the entire duration was recorded by an electronic mass balance (Sartorius, AZ214, 0.1 mg accuracy).

The steady-state water evaporation efficiency at steady-state conditions is defined as [79]

$$\eta = \frac{m_f h_{fg}}{Qs} \tag{6}$$

where m_f (kg m^{-2} h^{-1}) is the steady-state vapor mass flux rate, h_{fg} is the latent heat of vaporization for water at 1 atm (2.257 MJ kg^{-1}), and Q_s is the total incoming solar flux density (kW m^{-2}). The steady-state efficiency was calculated by using the data where the mass loss is linear to within an R^2-value of 0.998. Accordingly, with Ni SPhC as solar absorber, the steady-state evaporation efficiency was 81.5% under a solar intensity of 1 kW m^{-2}.

3.3 Theoretical simulations

3.3.1 FDTD simulation

All optical simulations were performed using FDTD simulation software package from Lumerical Computational solutions, Inc. 3D layout was employed for all theoretical simulations. Electric field distributions were recorded through two-dimensional frequency-domain field profile monitors. The transmitted power was detected using 2D power monitors. The permittivity of the exploited materials was measured by a three-dimensional refractive index monitor. All geometrical parameters of the sample were set according to the experimental measurements.

3.3.2 Comsol simulation

Electric filed distributions in the surface pre-patterned Al foil at the initial stage of anodization were calculated by COMSOL Multiphysisc (4.4 version). An ACDC module

(resistive device) was utilized for simulation. The periodic condition was set for cell boundaries. All structural geometries were set according to the SEM images of the as-imprinted Al foil. Due to the minimal potential drop in the electrolyte, a bias of V was completely applied to the Al foil following the stationary current conservation equations :

$$\nabla \cdot J = Q \tag{7}$$

$$J = \sigma E \tag{8}$$

$$E = -\nabla V \tag{9}$$

where J, Q, E, and V indicate the ionic current density, electric charge, electric field, and electric potential inside the Al foil, respectively.

CHAPTER 4. Results and discussion

In this chapter, PEC solar water splitting cells based on 1D nanostructure arrays and solar-to-thermal conversion systems using 2D superlattice photonic crystals as optical absorber are systematically investigated. In Section 4.1, 1D Au-PTP-core/ CdS-shell arrays were utilized to obtain omnidirectional photocurrent with an enhancement of about 400% due to the spectral complementation between SPR modes and photonic modes in the Au PTP structure over the operational spectrum. In Section 4.2, we elaborately designed and fabricated Janus Au/TiO_2 NWs and TiO_2/Pt NPs−Au, showing about 2.2 times photocurrent density and 4.6 times H_2 evolution rate of that obtained from their TiO_2 counterparts. The enhancement was mainly determined as a result of localized surface plasmon resonance induced direct hot electron injection and strong plasmon resonance energy transfer near the interfaces of TiO_2 nanotubes and Au nanorods. In Section 4.3, 2D Ni SPhCs with two sets of nanopores were fabricated, showing stable light absorption of ~95% and spectrally programmable cutoff wavelength in the range of 600-1500 nm. As selective solar absorber, Ni SPhCs promoted a solar steam generation system and a solar thermoelectric system. Accordingly, the water evaporation efficiency and the open circuit voltage output were enhanced by a factor of 2.3 and 2.5, respectively.

4.1 Plasmonic 1D nanostructure design for boosting PEC activity

4.1.1 State of the art

PEC water splitting, which could convert solar energy into chemical energy, has been intensively investigated over the last few decades.[53, 77, 80-86] One of the main challenges that limit the conversion efficiency of PEC electrodes is the severe trade-off between the long penetration depth of photons and the relatively short distance of carrier extraction at the electrode/electrolyte interface.[87, 88] Incorporating plasmonic nanostructures into a thin semiconductor is a promising route to address this issue, because SPR that originates from the plasmonic nanostructures can give rise to intriguing phenomena, including guiding electromagnetic radiation and enhancing near-filed electric field *etc*.[56, 89-95] By properly constructing plasmonic nanostructure, the incident light could be folded into the active material through directional scattering and intense-electric-field aided light absorption around the plasmonic nanostructures to achieve a film of electrical thinness and optical thickness.[96-98] Some attempts, like embedding gold NPs into a thin hematite Fe_2O_3 film,[99] or integrating gold pillars within CdS nanorod arrays,[100] were tried to incorporate these SPR features into PEC cells. However, SPR modes are typically suppressed in the short wavelength range (*e.g.*, < 500 nm for gold because of the strong intrinsic interband light absorption). In order to achieve a better light utilization, solar spectrum with short wavelengths needs to be concerned as well. Photonic modes that are capable of reducing reflection and inducing diffraction effect to the short wavelength range have been widely adopted, such as nanoengineering semiconductor films into archetectures with gradient refractive index profiles or manufacturing subwavelength periodic structures.[101-107] Moreover, SPR and photonic modes can work in synergy and compensate each other over a wide wavelength range. Such as, by conformally coating gold NP arrays with a thin hematite Fe_2O_3 film, an improved light utilization has been reported, in which the contributions of the photonic modes start over 500 nm and the SPR modes dominate at around 650 nm.[108] However, the zero dimensional nanostructure only

supports SPR modes at discrete wavelengths, which largely limits SPR function domain.[109-112] Meanwhile, the zero dimensional surface profile leads to a poor tunability of the photonic modes. Thus, in order to broaden the SPR optical region and photonic mode induced light trapping region, as well as to maximize their complementary absorption range, competent design of nanostructure architecture is highly requested.

In this section, an approach was proposed to construct an array of pillar/truncated-pyramid (PTP) Au plasmonic nanostructure on a large scale of centimeter-sized range, in which each unit is composed of a pillar (P) setting on a truncated-pyramid (TP). To demonstrate the advantages of the Au PTPs for light absorption, a uniform semiconductor (*e.g.*, CdS) film was deposited to form a CdS/Au PTP photoanode. Comparing to CdS/Au plane and pillars, a continuous IPCE enhancement from 300 to 600 nm was observed for the CdS/Au PTPs. Along with detailed FDTD simulation, we concluded that the IPCE enhancement above 450 nm is mainly originated in SPR modes, whereas the IPCE enhancement below 450 nm is dominated by the photonic modes. Systematic studies on the aspect ratio of P/TP and the thickness of CdS film were carried out to reach an omnidirectional and broadband enhancement in both optical absorption and quantum efficiency. The photocurrent density up to 3.5 mA cm^{-2} was obtained with only 120 nm thick CdS film on PTP (height = 270 nm, aspect ratio of P/TP = 0.5). Moreover, the activity of the as-prepared photoanode is almost angle independent and only less than 8% loss was observed from 0 to 40 degree.

4.1.2 Fabrication of periodic Au PTP nanostructure coated with CdS film

The process for fabricating CdS/Au PTP structures is revealed in Figure 4-1a. Briefly, a first-step anodization was carried out on an imprinted aluminum foil to grow AAO templates. By dissolving the AAO template in H_3PO_4 solution, aluminum nanotips were observed at the fourfold junction sites of anodized nanopores. Then, a second-step anodization was conducted to form inverted PTP nanopores. An Au (100 nm)/Ti (5 nm) layer

was deposited on the surface of the inverted PTP nanopores followed by growth of a thick Ni supporting film. An array of Au PTP was achieved by removing the unoxidized aluminum foil and AAO template, as the SEM images shown in Figure 4-1b and c. The profile of the PTP structure includes a P (height: 180 nm, size: 150 nm) on the top and a TP (height: 180 nm, size of the front- and back-side square surfaces: 150 and 370 nm) at the bottom. The P height can be easily tuned by altering the second-step anodization time. Finally, a continuous CdS thin layer (90 nm) was uniformly coated on the Au PTP using an electrodeposition process, as the top-down and cross-sectional SEM images shown in Figure 4-1d, e.

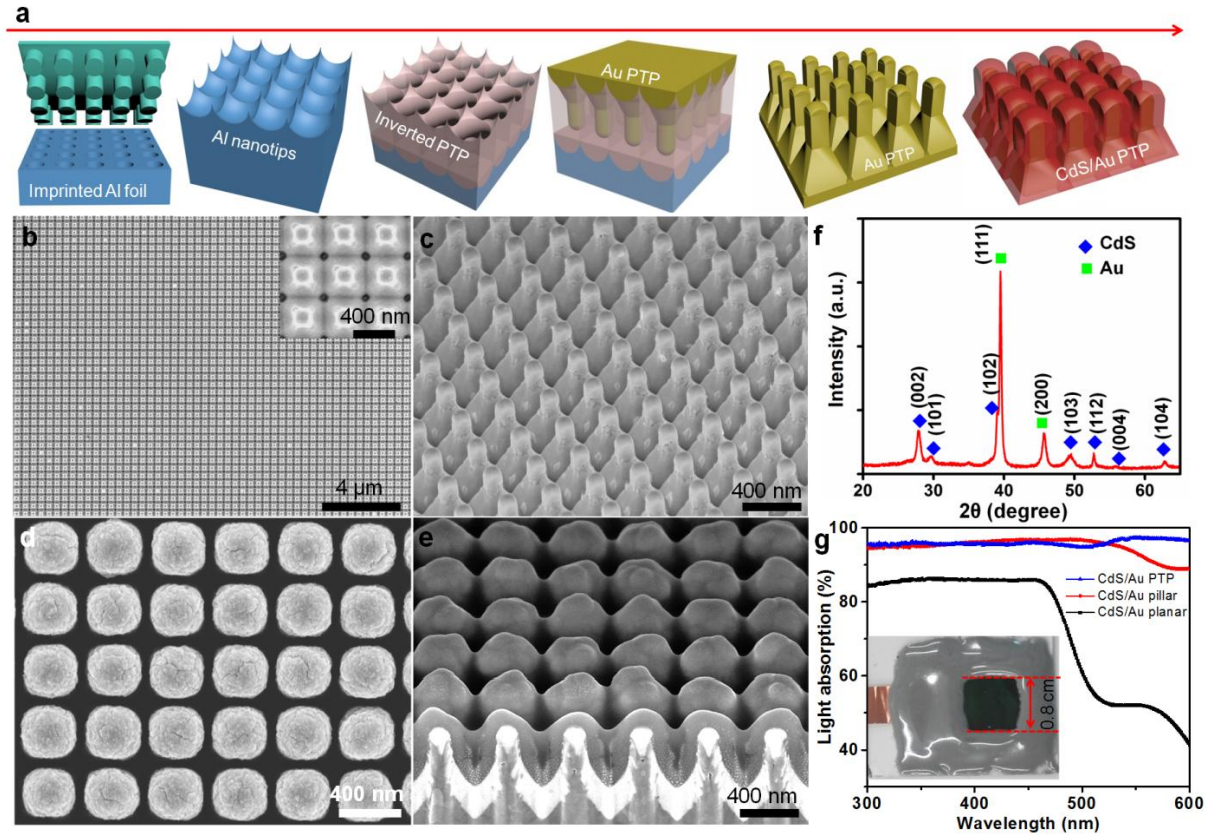

Figure 4-1. (a) Schematic of the fabrication process for CdS/Au PTP nanostructure array. (b) Large-area and (c) tilted SEM view of an Au PTP array, including top pillar (height: 180 nm, size: 150 nm) and bottom truncated-pyramid (height: 180 nm, size of the front- and back-side square surfaces: 150 and 370 nm, respectively). (d) Top-down and (e) cross-sectional SEM view of a CdS/Au PTP array coated with a 90 nm CdS film. (f) XRD of the as-prepared

CdS/Au PTPs. (g) Light absorption spectra of the CdS/Au PTPs, CdS/Au pillars, and CdS/Au planar, respectively. Inset: photo of a typical CdS/Au PTPs.

The composition of the as-prepared CdS/Au PTPs was confirmed by XRD measurement (Figure 4-1f). Besides the diffraction peaks of Au (JCPDS No. 65-8601), the other peaks can be indexed to (002), (101), (102), (103), (112), (004) and (104) diffractions of hexagonal CdS (PDF#65-3414). Meanwhile, an Au pillar array (with the same height of Au PTPs) and an Au planar coated with a 90 nm CdS film were used as the comparison samples. The absorption spectra of the CdS/Au PTPs, along with the CdS/Au pillars and planar, were collected under a diffuse reflectance mode (Figure 4-1g). The CdS/Au planar presents an absorption onset at 520 nm, in consistence with the bandgap of bulk CdS (2.42 eV).[113] More importantly, the CdS/Au PTPs shows a superior optical absorption of about 95% within the wavelength range of 300 − 600 nm. And a better optical absorption above 500 nm was also observed for the CdS/Au PTPs in contrast to the CdS/Au pillar, which agrees with the tendency of the Au PTPs and pillars absorption, indicating that the optical enhancement should be ascribed to the distinctive structure of the Au PTPs (Figure 4-2).

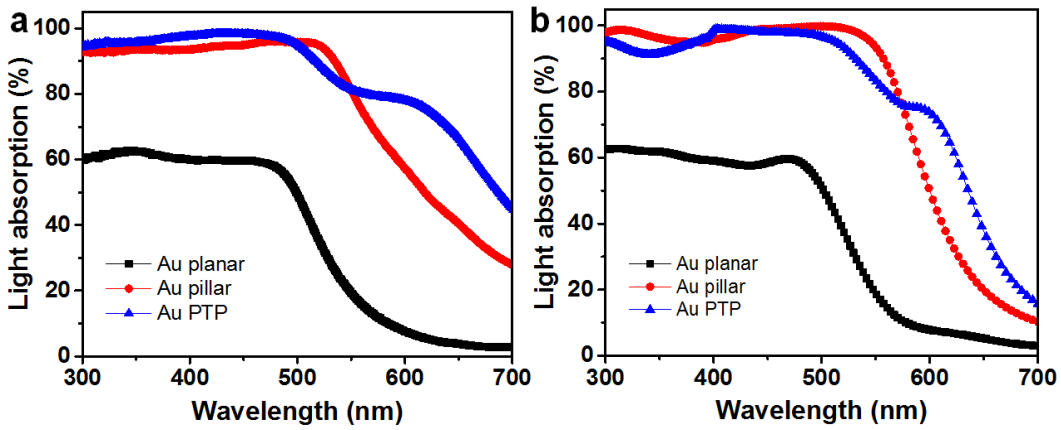

Figure 4-2. (a) Experimental and (b) simulated light absorption spectra of the Au PTP, pillar and planar.

4.1.3 PEC performance comparison between PTP and P CdS/Au anodes

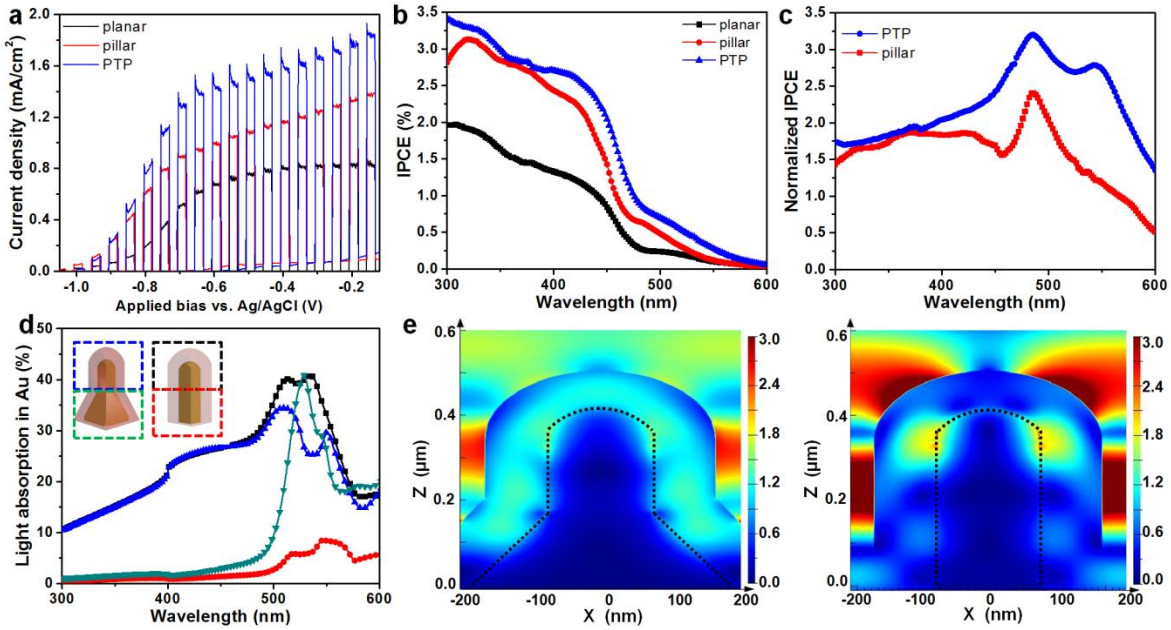

Figure 4-3. Characterization of CdS/Au PTP, pillar and plane. (a) Chopped photocurrent densities of CdS/Au PTPs, pillars, and plane under AM 1.5G illumination. (b) Spectrally resolved IPCE curves of the CdS/Au PTPs, pillars and plane within the wavelength range of 300 – 600 nm without applying an extra bias. (c) Normalized IPCE curves of the CdS/Au PTPs and pillars, which were calculated by dividing the IPCE of CdS/Au PTPs and pillars by that of the CdS/Au plane, respectively. (d) FDTD simulated absorption curves of the top (180 nm) and bottom (180 nm) parts of the Au PTPs and pillars in CdS/Au PTPs and pillars, respectively. (e) FDTD simulated electric field distributions $|E/E_0|$ of the CdS/Au PTPs (left) and pillars (right) at the wavelength of 550 nm.

The PEC performance was measured in a mixed aqueous solution (0.2 M Na_2S and 1.0 M $Na_2S_2O_3$) using a three-electrode cell under the illumination of AM 1.5G. The chopped I-V curves were collected in Figure 4-3a. The photocurrent density was significantly enhanced for the CdS/Au PTPs when compared to that of the CdS/Au pillars and planar, with an enhancement of about 40% and 125% at a bias of -0.4 V (vs. Ag/AgCl), respectively. Moreover, because the onset potential of the photocurrent remained the same for all three photoanodes, it can be concluded that the underneath Au has not been involved in a surface catalysis process at the semiconductor-electrolyte interface. Also, the CdS/Au PTPs

photoanode exhibits excellent thermal robustness after an annealing treatment at 350 ^{o}C, because the photocurrent even shows a slight improvement. The reason may be ascribed to the crystallization of the CdS film, which can be evidenced by the emergence of grains on the CdS surface and the intensity enhancement of the CdS diffraction peaks (Figure 4-4a-c).

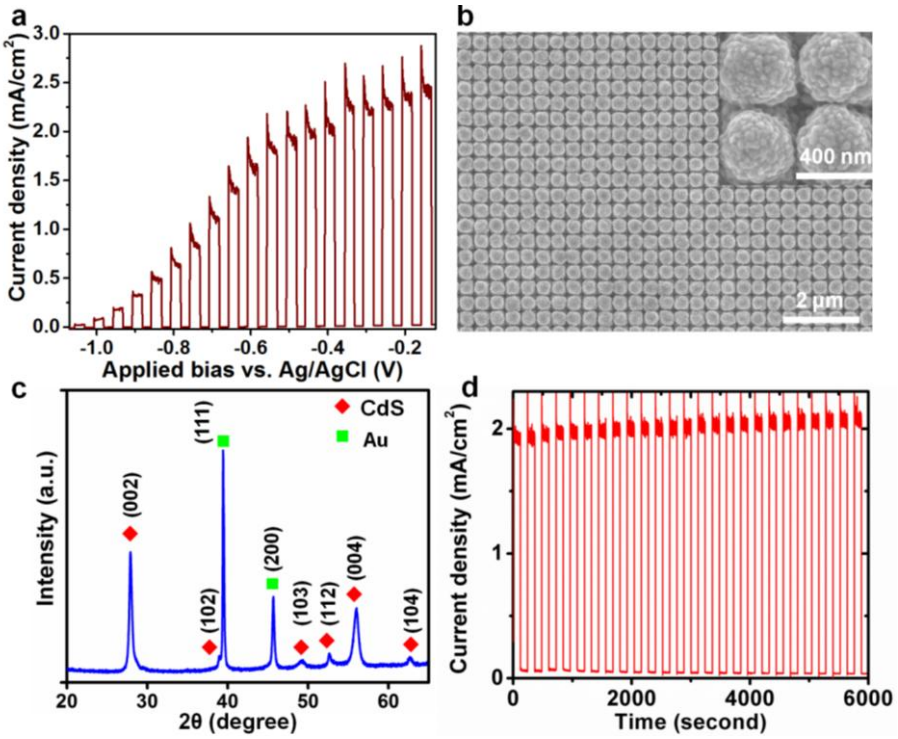

Figure 4-4. Characterization of annealed CdS/Au PTPs. (a) Chopped photocurrent densities of annealed CdS/Au PTPs under AM 1.5G illumination. (b) SEM image and (c) XRD diffraction peaks of the CdS/Au PTPs after annealing treatment. (d) Photocurrent stability test for the CdS/Au PTP anode at a bias of -0.4 V (vs. Ag/AgCl) under AM 1.5G irradiation.

On the other hand, spectrally resolved IPCE was measured in the same solution using a two-electrode cell without applying external bias. The CdS/Au PTPs showed a substantially IPCE enhancement within the wavelength range of 300 − 600 nm when compared with that of the CdS/Au planar (Figure 4-3b), agreeing with the tendency of the photocurrent results. In the meantime, a better IPCE enhancement over 450 nm was also observed for the CdS/Au PTPs than that of the CdS/Au pillars. The difference is more clearly from the normalized IPCE in Figure 4-3c, where a wavelength dependent IPCE enhancement with two peaks at

490 and 550 nm was observed for the CdS/Au PTPs, while only one peak at 490 nm for the CdS/Au pillars. The durability of the CdS/Au PTPs was tested at a bias of -0.4 V (vs. Ag/AgCl), in which the photocurrent maintained almost no degradation under AM 1.5G illumination over 100 minutes (Figure 4-4d).

Since the light absorption in the semiconductor (CdS) and in the metallic (Au) regions is hard to distinguish, theoretical FDTD simulations were employed to elucidate the optical difference between the CdS/Au PTPs and pillars. When SPR is excited, the collective charge oscillations at the metal surface cause increased the ohmic loss of electromagnetic energy, which can be visualized as peaks in the spectrally resolved absorption of the metal.[114] By extracting the absorption in the Au region, the electromagnetic energy dissipated at the top P (180 nm) and bottom TP (180 nm) of Au PTPs were obtained, respectively (Figure 4-3d). It shows that the top P part has two distinct absorption peaks at 500 and 550 nm, while the bottom TP part has one major peak at 525 nm and one shoulder at 550 nm. These Au absorption peaks are generally coincident with the normalized IPCE features of the CdS/Au PTP (Figure 4-3c). Small peak shift might originate from a discrepancy between the experiment and simulation, like the variation of the PTP geometry, the surface roughness of CdS/Au PTPs that is unavoidable in reality but not considered in the simulation. For a comparison, the FDTD simulation concerning the Au pillar was also studied. The top part of Au pillars (top P: 180 nm) shows two absorption peaks at 500 and 525 nm, which is quite similar to that of the Au PTPs (top P: 180 nm). However, no absorption peak from the bottom part of the Au pillars (bottom P: 180 nm) was observed, which explains the loss of the normalized IPCE peak at 550 nm for CdS/Au pillars. These results can be further supported by the electric field distribution on CdS/Au PTPs and pillars at 550 nm (Figure 4-3e). The red and yellow color areas in CdS present relatively strong electric fields, which uniformly distribute around the whole profile of the PTP, but only partially focus on the top part of the pillar. Therefore, the IPCE enhancement over 450 nm should be mainly caused by the SPR

modes that generate at the CdS-Au interface and result in an enhanced light absorption in CdS layer. This point can be further confirmed by a CdS photoanode based on weakly- or non-plasmonic metals (*e.g.*, Pt) PTP structure, where the IPCE enhancement can be barely observed in the long wavelength range (Figure 4-5).

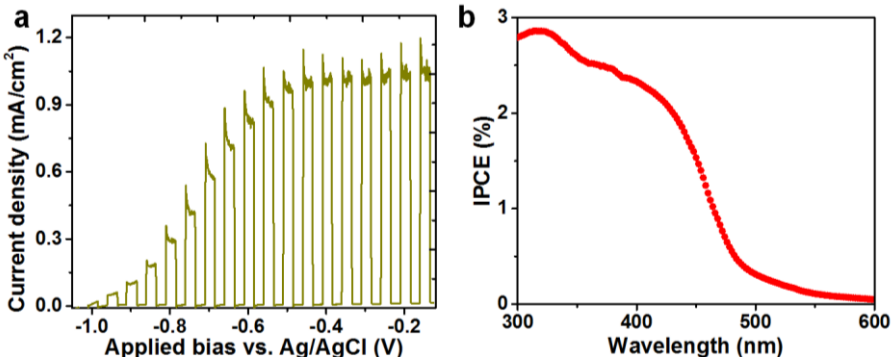

Figure 4-5. Characterization of CdS/Pt PTPs. (a) Chopped photocurrent densities of CdS/Pt PTPs under AM 1.5G illumination. (b) Spectrally resolved IPCE curves of the CdS/Pt PTPs within the wavelength range of 300 – 600 nm without applying an extra bias.

4.1.4 Performance optimization of PTP CdS/Au anode

On the other hand, because no SPR peak was observed below 450 nm, the IPCE enhancement within the range of 300 − 450 nm might be ascribed to the photonic modes and/or the increased surface area of the nanostructure. Considering that, CdS/Au PTPs with different P/TP height ratios (0.1, 0.5, 1.0) were prepared, in which the surface area increases gradually (Figure 4-6a). The chopped I-V curves of these photoanodes revealed that the photocurrent reaches to a maximal value of about 2.5 mA cm^{-2} at a bias of -0.4 V (vs. Ag/AgCl) when the ratio of P/TP is 0.5, instead of increasing with the raise of the photoanode surface area (Figure 4-6b). Moreover, from the normalized IPCE of CdS/Au PTPs in Figure 4-6c, the P/TP (0.5) shows an even IPCE enhancement across the whole wavelength range with a magnitude of about 300% and 150% to that of the P/TP (0.1) and P/TP (1.0), respectively. Thus, the change of surface area has an ignorable effect, while the photonic modes resulted strong light scattering at the interface of the CdS and Au plays a dominant role

in the enhanced photocurrent below 450 nm. These results can also be supported by the FDTD simulation results (Figure 4-6d). Comparing to the PTP (0.1) and (1.0), the PTP (0.5) demonstrates a strong electric field distribution not only at the top and side wall but also in the valley between the neighboring PTPs. More importantly, we can conclude that with an appropriate aspect ratio of P/TP, the SPR and photonic modes can efficiently compensate each other to improve the light utilization in CdS layer over a wide range of wavelengths.

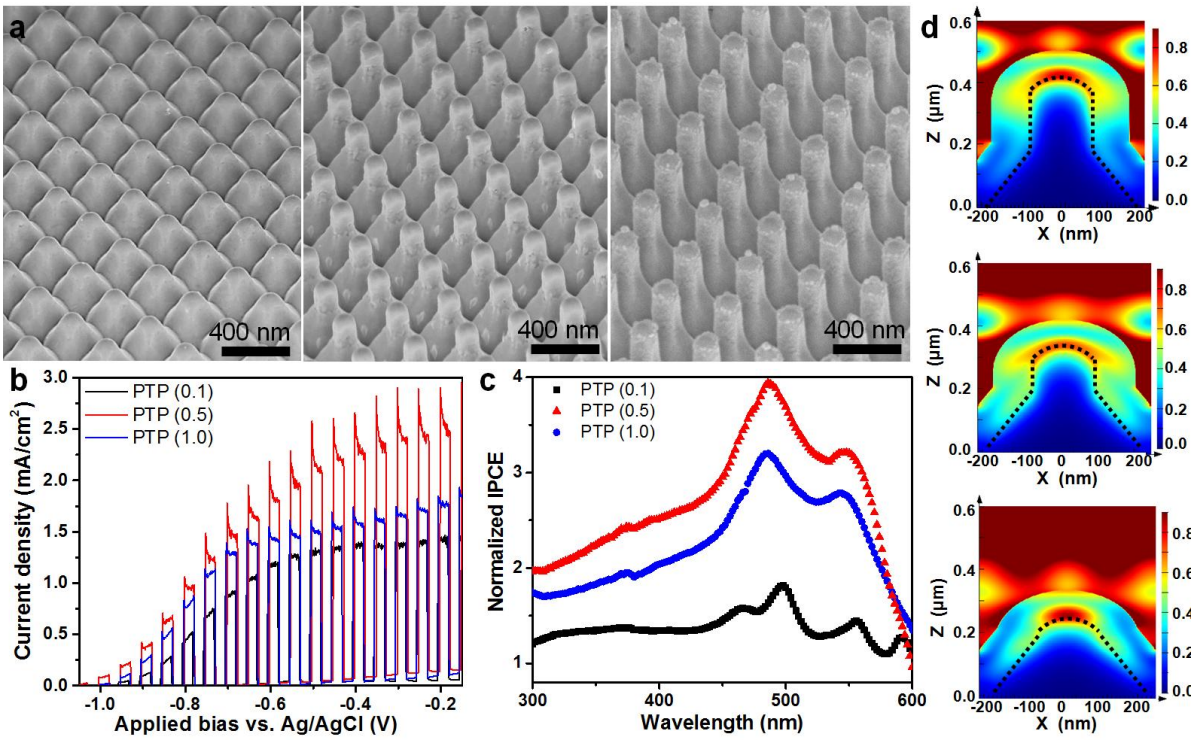

Figure 4-6. Characterization of CdS/Au PTPs with different P/TP height ratios. (a) SEM view of typical CdS/Au PTPs with different P/TP height ratios. From left to right: 0.1, 0.5, and 1.0, respectively. (b) Chopped photocurrent densities of the CdS/Au PTPs under AM 1.5G illumination. (c) Normalized IPCE curves of the CdS/Au PTPs, which were calculated by dividing the IPCE of the CdS/Au PTPs by that of the CdS/Au plane. (d) FDTD simulated electric field distributions $|E/E_0|$ of the CdS/Au PTPs with different P/TP ratios at the wavelength of 350 nm. From top to bottom: 1, 0.5, and 0.1, respectively.

Besides the metallic nanostructure, SPR effect also depends upon the dielectric environment surrounding the metal.[115, 116] Because of the subwavelength thickness of the CdS

layer, the effective refractive index is an average of the CdS layer and the electrolyte.[117, 118] Thus, the wavelength related photocurrent is possible to be tuned by changing CdS thickness. With deposition time elongation, the architecture of CdS/Au PTPs (0.5) gradually evolved from a core/shell structure to a planar film and the uniformity of the deposited CdS layers over large scales can be confirmed in Figure 4-7.

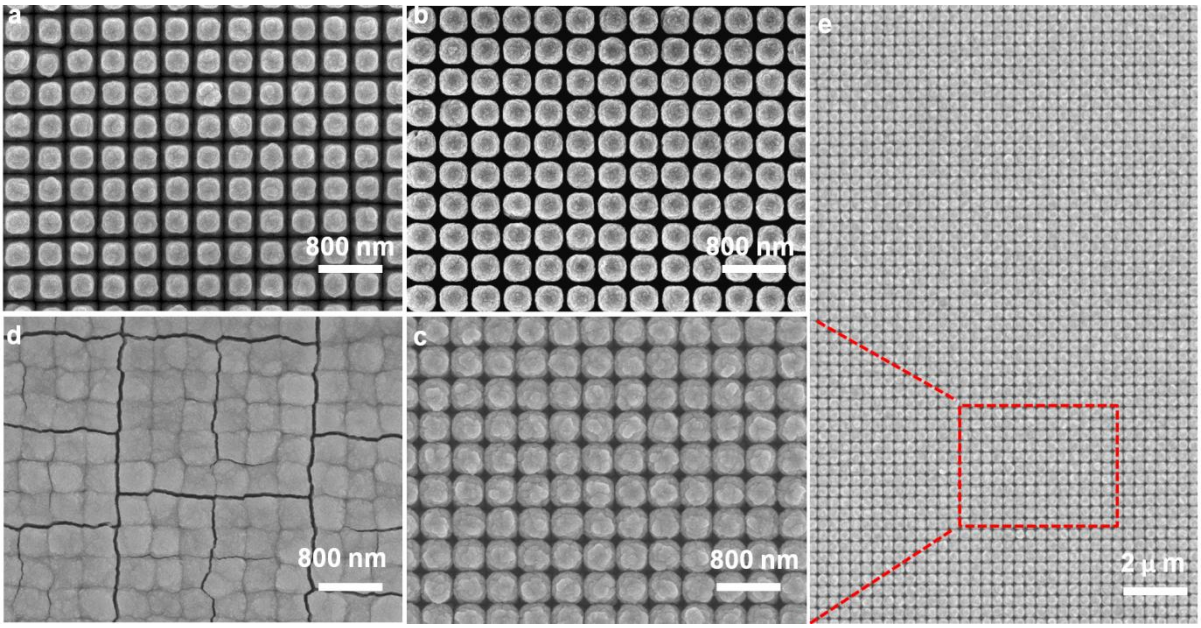

Figure 4-7. SEM images of CdS/Au PTP (0.5) anodes with various thicknesses of CdS films ranging from (a) 60 nm, (b) 90 nm, (c) 120 nm, to (d) a merged film. (e) SEM image of a typical large-scale CdS/Au PTP (0.5) with 120-nm-thick CdS.

The chopped I-V curves reveal that the photocurrent density was enhanced more than two times with the increase of CdS thickness from 60 to 120 nm (Figure 4-8a). When the CdS thickness was further increased, a merged CdS film was formed with a pronounced decline of photocurrent. Because the normalized IPCE peaks in the long wavelength region show minimal wavelength shift, SPR effects play a similar role in all samples (Figure 4-8b). But the absolute values of the normalized IPCE alter significantly with the change of CdS thickness, implying that the photonic modes strongly depend on the CdS thickness and the formed nanostructure profile. The FDTD simulated electric field distribution of the CdS/Au PTPs are in accordance with the IPCE results. Obviously, the coverage of the strong electric field in the

CdS layer becomes broader with the CdS thickness increasing from 60 to 120 nm. After the CdS layer merged to a planar film, surface-profile-induced photonic modes vanished, which results in a sharp shrink of the strong electric field in the CdS layer (Figure 4-8c).

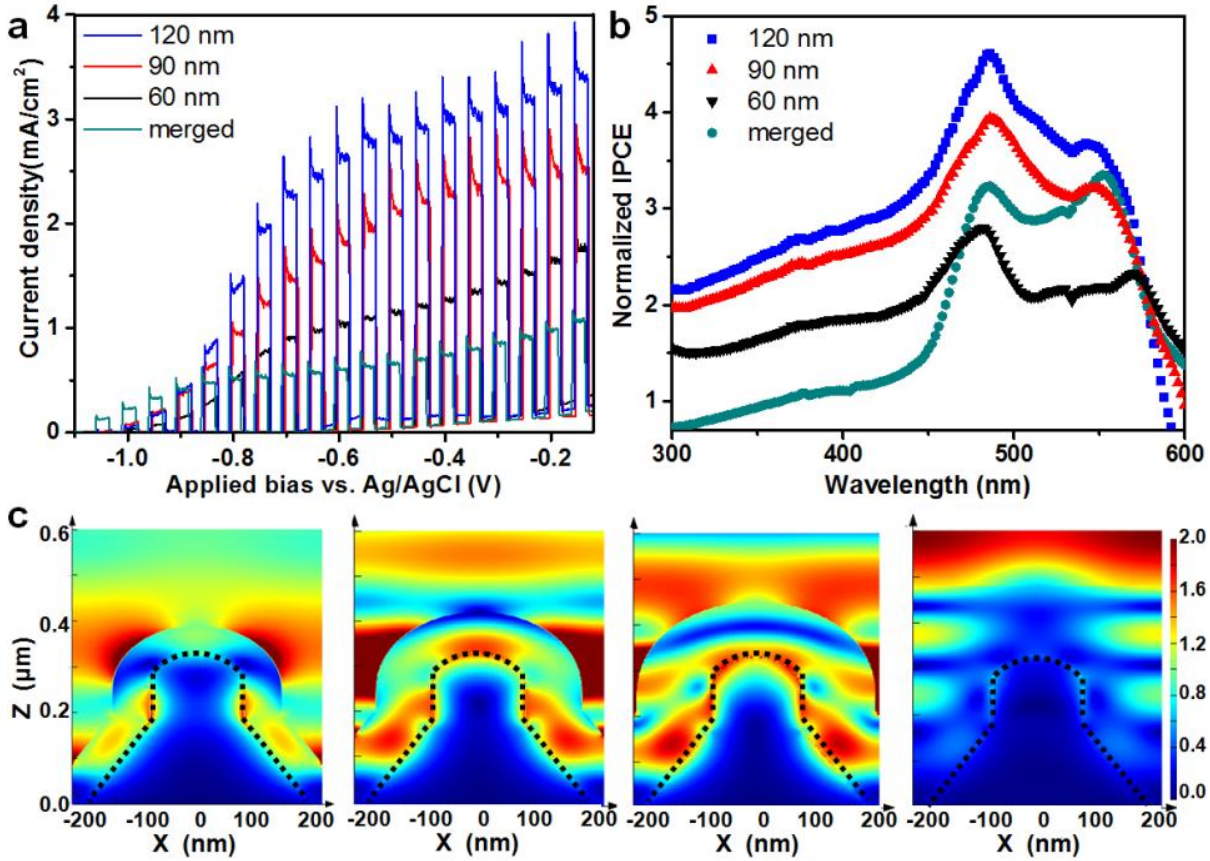

Figure 4-8. Characterization of CdS/Au PTPs (0.5) with different CdS thicknesses. (a) Chopped photocurrent densities of the CdS/Au PTPs (0.5) with different CdS thicknesses under AM 1.5G illumination. (b) Normalized IPCE curves of the CdS/Au PTPs (0.5) with different CdS thicknesses, which are calculated by dividing the IPCE of the CdS/Au PTPs (0.5) by that of the CdS/Au planar, respectively. (c) FDTD simulated electric field distributions $|E/E_0|$ of the CdS/Au PTPs (0.5) with different CdS thicknesses at the wavelength of 550 nm. From left to right: 60 nm, 90 nm, 120 nm, and merged, respectively.

4.1.5 Incident angle dependence of PEC performance of PTP CdS/Au anode

It should be noted that all previous measurements were performed under the normal incidence of AM 1.5G illumination and from a practical perspective, the investigation of the incident angle effect is essential. The wavelength-resolved optical absorption of the CdS/Au

PTPs (0.5) as a function of incident angle was calculated by FDTD simulations. The results revealed that only a slight variation is observed in the photonic-modes dominated short wavelength region, while the optical loss is mainly generated over long wavelength region that is dominated by the SPR modes (Figure 4-9a). In order to evaluate the overall light absorption of the CdS/Au PTPs, the averaged light absorption (ALA) is employed, which is calculated by dividing the solar photons absorbed in the CdS/Au PTPs by the total solar photons in the wavelength range of 300-600 nm [Equation 1].[119, 120]

$$ALA = \frac{\int_{\lambda 0}^{\lambda 1} LA(\lambda) * \frac{\lambda}{hc} * I_{AM1.5}(\lambda) d\lambda}{\int_{\lambda 0}^{\lambda 1} \frac{\lambda}{hc} * I_{AM1.5}(\lambda) d\lambda} \quad (1)$$

where h is Planck's constant, c is light speed in free space, λ is light wavelength (λ0 and λ1 equal 300 and 600 nm, respectively) and $I_{AM1.5}$ is the solar spectrum of AM 1.5G, LA is the simulated light absorption in Figure 4-9b. All ALA maintain around 90% regardless of the incident angle which implies an almost angle-independent PEC performance (Figure 4-9b and 4-10f). Note that, a slight reduction of the photocurrent density (< 8%) was observed as the incident angle is altered from 0 to 40 degree (Figure 4-9b). It can be ascribed to the nonuniform electric field distributions that increasing incident angle results in spatial shrinkage of the strong electric filed in the CdS layer, which will lead to stronger recombination of the photogenerated carriers and consequently, a somewhat deteriorated photocurrent (Figure 4-10a-e).

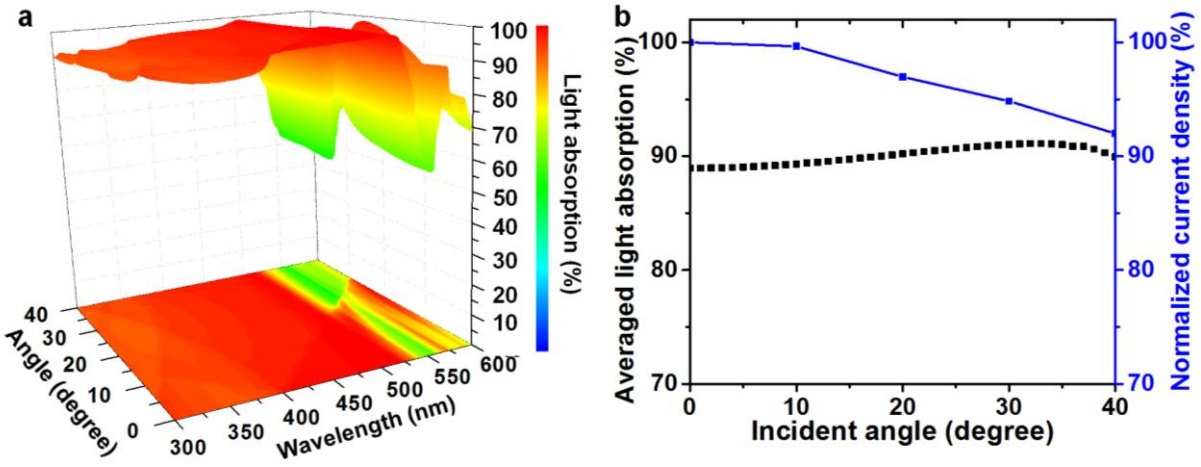

Figure 4-9. Optical characterization of the CdS/Au PTPs (0.5) with 120 nm CdS as a function of incident angle. (a) Simulated spectrally-resolved light absorption. (b) Averaged light absorption and normalized photocurrent density under AM 1.5G illumination at -0.4 V vs. Ag/AgCl.

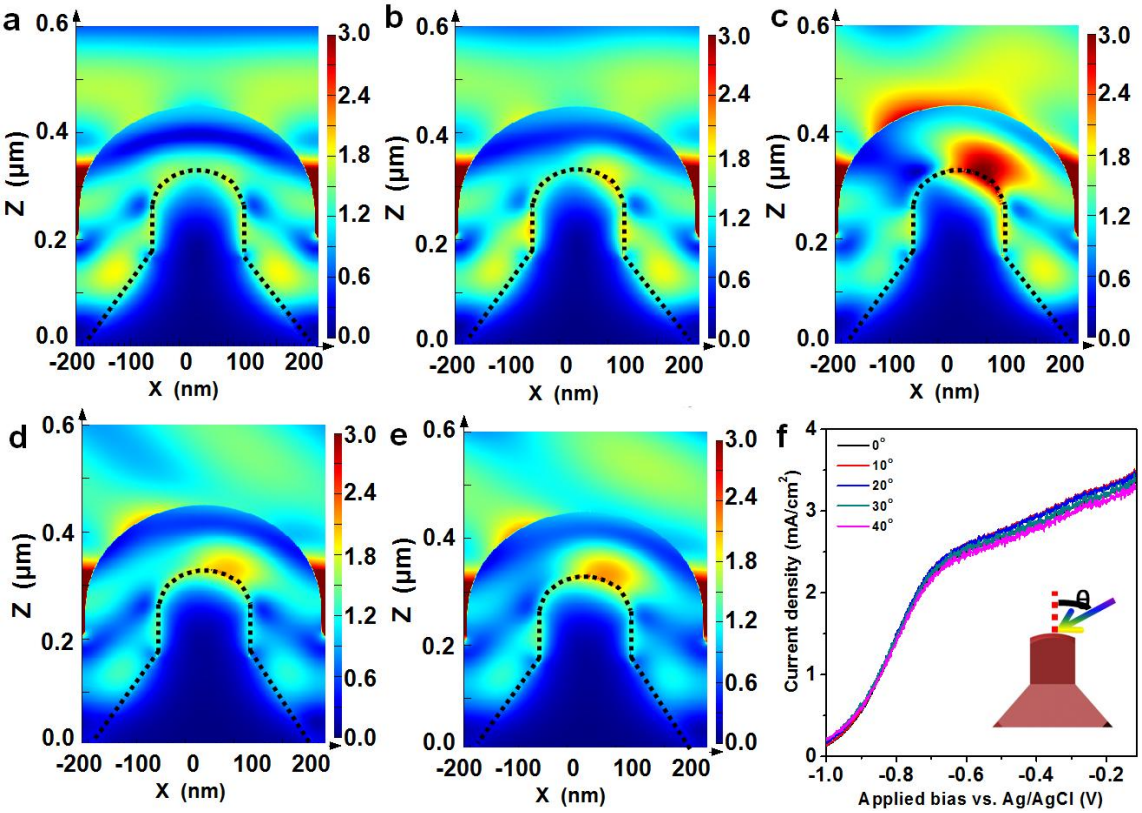

Figure 4-10. Electric field distribution of the CdS/Au PTPs (0.5) with 120 nm CdS illuminating with 550-nm-wavelength light of different incident angles ranging from (a) 0, (b) 10, (c) 20, (d) 30 to (e) 40 degree. (f) Photocurrent density of the CdS/Au PTPs (0.5) with 120

nm CdS as a function of incident angle under AM 1.5G illumination. Inset: schematic drawing of a PTP anode with an angle of incidence.

4.1.6 Conclusion

Perfectly ordered arrays of CdS/Au PTP nanostructures were successfully fabricated with a combination of nanoengineered AAO template and conventional techniques (*e.g.*, PVD and electrodeposition). A significant IPCE enhancement was observed by taking advantage of SPR and photonic modes root in Au PTPs, where the SPR modes dominate in the longer wavelength range over 450 nm and photonic modes contribute mainly in the shorter wavelength range below 450 nm. Different Au PTP profile and CdS thickness were systematically investigated with experiments and FDTD simulations to reach an omnidirectional and broadband enhancement in both optical absorption and quantum efficiency. The photocurrent up to 3.5 mA cm^{-2} was obtained from the CdS/Au PTP (0.5) with only less than 8% loss from 0 to 40 degree irradiation, four times of that from the planer CdS/Au. Moreover, the scalable strategy demonstrated here should not be limited to the CdS/Au PTP. Other plasmonic PTP, such as Ag, Al, Cu, and alloyed metals together with thin semiconductor materials are highly expectable for cost-effective photovoltaic and photochemical electrodes.

4.2 Template-guided programmable 1D Janus heteronanostructure arrays for efficient plasmonic photocatalysis

4.2.1 State of the art

Hetero-nanostructures (HNs) that integrate two or more nanocomponents by solid-state interfaces are emerging as an important family of advanced nanoarchitectures, owning to the synergistic effects induced by direct electronic and magnetic communications between the constituent nanocomponents.[121-126] Of particular interest are Janus HNs that comprise a metal and a semiconductor component, which have been applied in a broad range of areas including optoelectronics, catalysis, solar energy conversion, sensing, environmental remediation, and biomedicine.[121, 123, 127-130] The main merits of such Janus HNs for solar energy conversion are that they could not only increase charge injection and optical path length, but also enhance light absorption from visible to IR range, as compared to their single semiconductor counterparts alone or their physical mixture counterparts.[90] So far, three important strategies to construct efficient plasmonic metal−semiconductor HNs have been generalized in literature: 1) Tuning LSPR properties of plasmonic metals through adjusting their size, shape, and arrangement;[90, 131-133] 2) Adjusting the optical microcavities of semiconductors with the forms of photonic crystal,[134] whispering gallery mode,[135] and Fabry–Perot resonator;[136] 3) Optimizing the coupling effects between plasmonic metals and semiconductors by choosing isotropic configurations such as core@shell structures that are formed by completely coating metal with semiconductor or anisotropic structures (e.g., Janus and dumbbell-like) that are formed by partially integrating both of them at selected locations.[129, 137] Many studies showed that the anisotropic HNs enhanced photoconversion as compared to isotropic structures [129, 130, 138-140] due to the strong LSPR that locates at the junction area between plasmonic metals and semiconductors. Concurrently, the exposed domains of both the metal and semiconductor can facilitate charge carriers transfer from the HNs to their reaction partners such as oxidization agents and reduction agents in a liquid medium.

In order to assemble deterministically targeted Janus HNs at a large scale, various synthesis techniques have been intensively explored including bottom-up self-assembly and top-down lithography.[106, 125, 126, 141-143] The self-assembly strategies have been mainly focused on wet chemical processes, in which careful regulation of thermodynamic parameters and growth kinetics under the assistance of selected solvents, ligands, surfactants or catalyst additives are usually required case by case for different HNs.[125] On the other hand, lithography guided by templates such as polystyrene and hard AAO templates mainly relies on electrodeposition and physical/chemical vapor deposition.[106, 142, 144, 145] However, the resultant HN interfaces are always restricted to longitudinal direction with few options of size and shape for different nanocomponents.[106, 142] Therefore, although valuable advances in this field are attained, the development of an approach that enables precise control over each nanocomponent and their interface is still imperative to fully exploit the synergistic effects of Janus HNs.

In this section, we presented an approach to fabricate arrays of Janus HNs with the assistance of binary-pore template. We chose TiO_2−Au Janus HNs as a model system, because they are typical plasmonic−semiconductor HNs that are stable, readily synthesized and among the most studied HNs.[137] We employed a sequential process of over-etching and electrodeposition on a TiO_2−filled binary-pore template to grow TiO_2−Au Janus HNs (Figure 4-11a). We presented that each nanocomponent of the TiO_2−Au Janus HNs could be independently controlled at the different steps ranging from pore widening, over-etching, to material deposition. By incorporating an upgraded two-step anodization process, this general strategy enables to synthesize even more complex Janus HNs that are otherwise difficult to obtain. By combining with theoretical finite-difference time-domain modelling, we elucidated the boosted photocatalytic performance of the TiO_2−Au and TiO_2/Pt NPs−Au Janus HNs was ascribed to the LSPR effect along the interface of Au NRs and TiO_2 NTs induced direct hot electron injection and suppression of charge carrier recombination.

4.2.2 Synthesis and characterization of TiO_2−Au Janus HNs

A schematic flow diagram of the fabricating process of Janus HNs and the corresponding SEM images are shown in Figure 4-11.[146] The crucial step is over-etching of the B-pores of binary-pore template, which uniformly exposes the four edges and the tip of the square TiO_2 NTs that were deposited in the anodized A-pores via ALD (Figure 4-11a and b). Subsequently, an electrodeposition process was used to grow Au NRs in the over-etched B-pores, where intimate contacts with Au NRs were formed along the exposed four edges of the TiO_2 NTs (Figure 4-11a and c). The interfacial area can be adjusted by changing the Au NR length. When a short Au deposition time of 30 min was used, only partial length (~1.4 μm) of the TiO_2 NT edges (~ 2.0 μm) was covered by the Au NRs (Figure 4-12a). With the deposition time extending to 45 min, the isolated Au NRs in the over-etched B-pores overgrew from the template and converged to form a continuous Au nanopore film around the tips of the TiO_2 NTs (Figure 4-12b). Thus, the overgrowth should be avoided to assure that both the TiO_2 NTs and Au NRs have exposed domains simultaneously. A freestanding array of TiO_2−Au Janus HNs was presented after removing the remaining template (Figure 4-11a and d). Considering the fact that all the nanocomponents are densely packed with each other, the integrity of the TiO_2−Au HNs is retained with superior robust to many other reported HNs.[106]

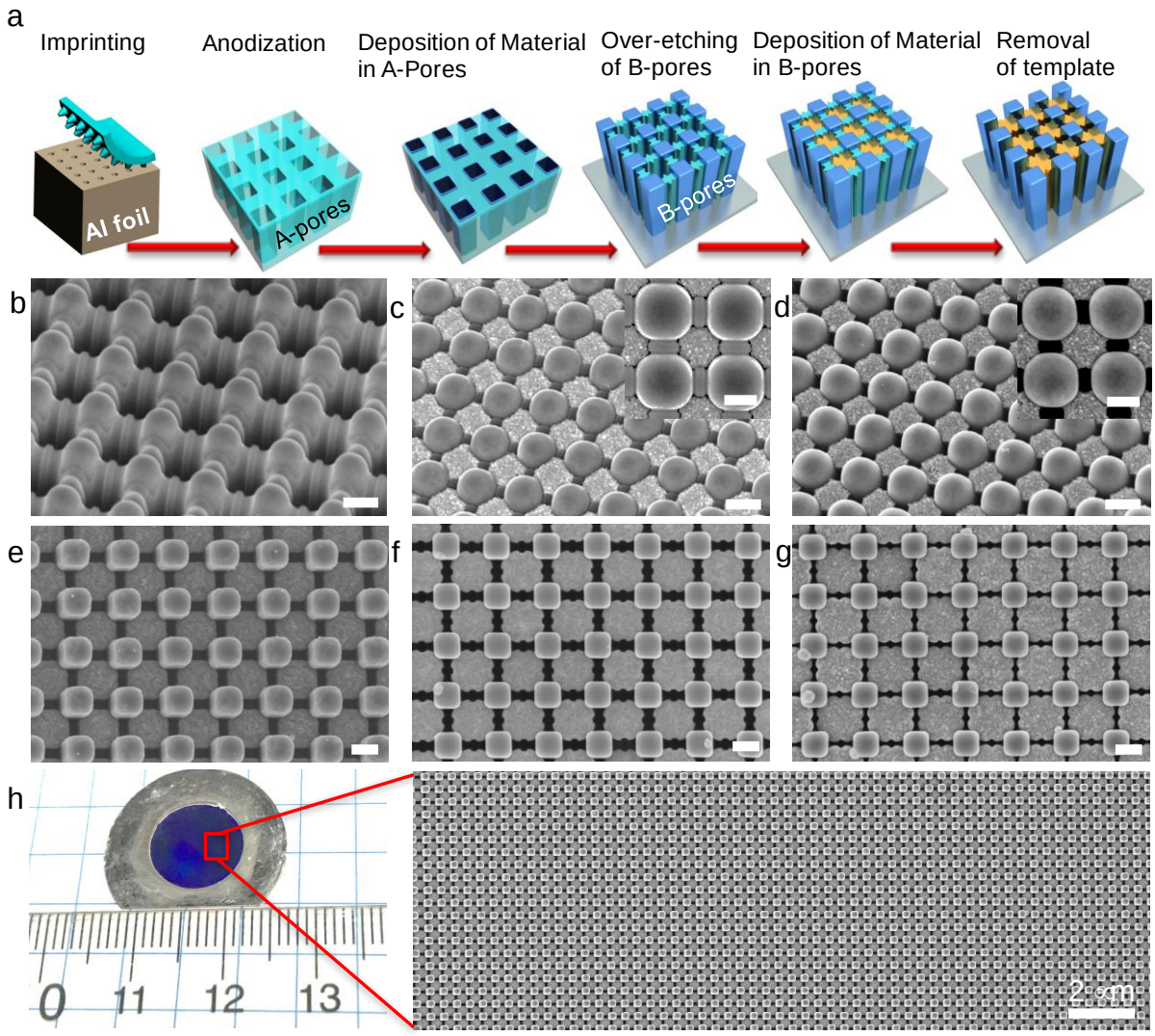

Figure 4-11. Array of Janus HNs. (a) Schematic flow diagram of the fabrication process of Janus HN arrays. (b) A tilted view SEM image of an A-pore TiO_2 filled template after 1h over-etching. (c) A tilted view and an enlarged top view (inset) SEM images of a binary template after the electrodeposition of Au NRs in the over-etched B-pores. (d) A tilted view and an enlarged top view (inset) SEM images of TiO_2−Au Janus HNs after removing the template. TiO_2−Au Janus HNs with different Au NRs and interfaces obtained after template over-etching: (e) in NaOH solution for 1h; (f) in NaOH solution for 40 min and then in H_3PO_4 for another 1h; (g) in NaOH solution for 70 min and then in H_3PO_4 for another 1h. (h) Photograph (left) and SEM image of a typical large-scale TiO_2−Au Janus HN array. Scale bars: 200 nm.

It is worth noting that the size and shape of the Au NRs and TiO_2 NTs can be readily adjusted as well as their interfaces. For example, quasi-square shaped Au NRs with the size of about 220 nm were obtained (Figure 4-11e) through over-etching of template in NaOH solution for one hour. As we changed the over-etching time in NaOH solution to 40 min and then another one hour in H_3PO_4 solution, four identical concaves were observed at the middle of each side of square Au NR (Figure 4-25f). Concurrently the size of the Au NRs was enlarged to about 300 nm with 70 min over-etching in NaOH and then another 1h in H_3PO_4 solution (Figure 4-11g). While the size of TiO_2 NTs could be enlarged using different pore-widening time for the A-pores (Figure 4-12c and d). Accordingly, the interfaces of the Au NRs and TiO_2 NTs were also changed due to the different perimeter exposure of the TiO_2 NT edges. Moreover, the photograph and low-magnified SEM in Figure 4-11h demonstrated a uniform square-centimeter area of the TiO_2−Au Janus HNs, which could be scaled up to wafer size with other advanced imprinting techniques, such as roll to roll nanoimprinting.[147] Therefore, large-scale arrays of TiO_2−Au Janus HNs with customized nanocomponents and interfaces could be realized by adjusting the different parameters ranging from over-etching, pore widening, to material deposition.

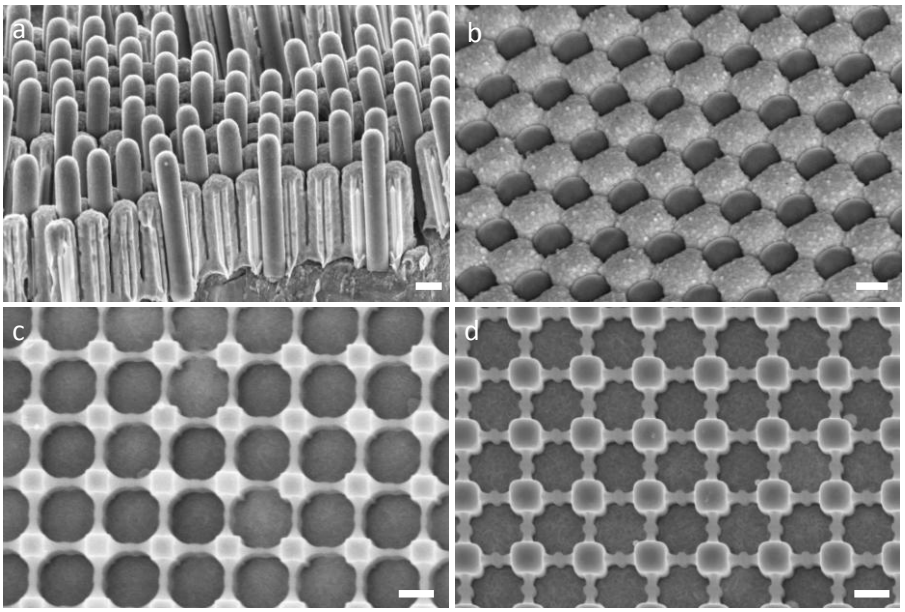

Figure 4-12. SEM images of TiO_2−Au Janus HNs with Au NRs of different lengths: (a) ~ 1.4 μm and (b) ~ 2.1 μm. SEM images of TiO_2−Au Janus HNs with TiO_2 NTs of different sizes: (c) ~ 161 nm and (d) ~ 221 nm. Scale bars: 200 nm

The composition of as-prepared TiO_2−Au Janus HNs was confirmed by energy-dispersive X-ray (EDX) mapping and line-scanning. The EDX maps of an array of Janus HNs confirmed the perfect match of the spatial distributions of Ti (cyan) and Au (orange) with the arrangement of the A- and B-pores in the binary-pore template (Figure 4-13a). While the O (green) and Al (dark cyan) elemental distributions coincide with the frame of the remaining template. The TiO_2−Au Janus HNs was also confirmed by EDX line-scan along a row of six HNs after dissolving the template (red arrow indicated in Figure 4-13b). The periodic elemental distributions of Ti (cyan curve) and O (green curve) perfectly match each other with respect to the square wires, while the elemental distribution of Au (yellow curve) fits with the quasi-square wires with concaves on each side. Moreover, noble metal and transition metal oxide NPs were incorporated into the HNs as functional co-catalysts.[148] For example, Pt NPs were deposited inside the A-pores via 2 cycles of ALD before the deposition of TiO_2 NTs.

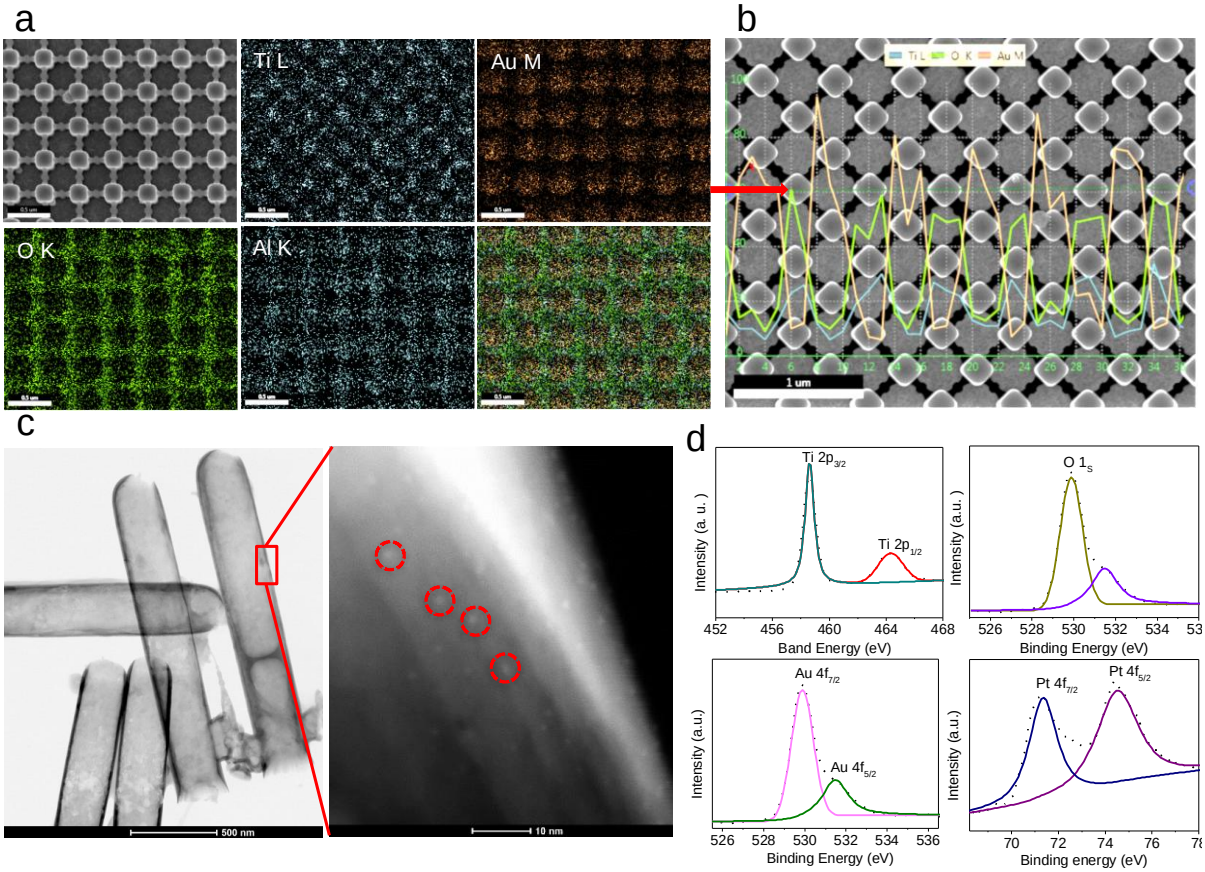

Figure 4-13. EDX, TEM and XPS Characterization of Janus HNs. (a) SEM image and the corresponding EDX elemental maps of TiO_2−Au Janus HNs within template (Ti, cyan; Au, orange; O, green; Al, dark cyan). (b) EDX elemental line-scan of freestanding TiO_2−Au Janus HNs, where the distribution profiles of Ti (cyan), O (green), and Au (orange) along the green line are plotted and imbedded in SEM image (red arrow indicated). (c) TEM image of scratched TiO_2/Pt NTs. (d) XPS spectra of TiO_2/Pt NPs−Au Janus HNs, including Ti 2p, O 1s, Au 4f, and Pt 4f, respectively.

TEM elemental mapping of the as-prepared TiO_2/Pt NTs shows that the Ti and Pt element intensities are much stronger along the perimeter edges of the nanopores, confirming the existence of the Pt and TiO_2 inside the nanopores (Figure 4-14a). After scratching the TiO_2/Pt NTs from the substrate, it was clearly indicated that the Pt NPs with an average size of about 2 nm were anchored on the outside surface of TiO_2 NT (Figure 4-13c). X-ray photoelectron spectroscopy (XPS) was also used to examine the metal Pt NPs in a TiO_2/Pt NPs−Au Janus HNs (Figure 4-14b). The high-resolution Ti 2p3/2 and Ti 2p1/2, as well as O

1s core-level, are consistent with the typical values of the TiO_2. And the observed intense doublet of Au (83.8 and 87.4 eV) and Pt (71.2 and 74.5 eV) is due to the obvious metallic Au0 and Pt0, respectively (Figure 4-13d).

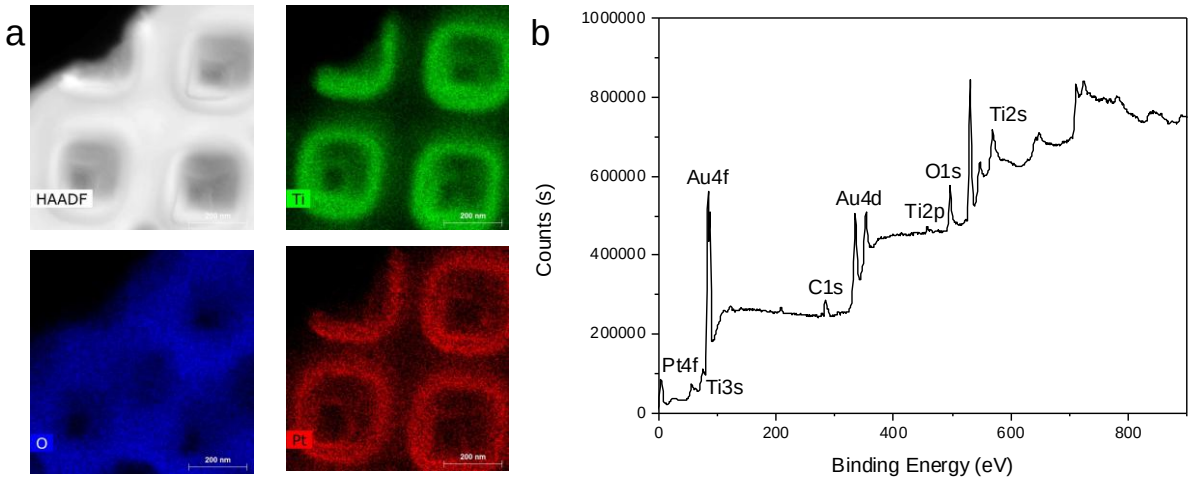

Figure 4-14. Material characterization of Janus HNs. (a) TEM elemental mapping of an array of TiO_2/Pt NTs after the sequential ALD deposition of Pt NPs (2 cycles) and TiO_2 NTs (800 cycles). (b) Full XPS spectrum of an array of TiO_2/Pt NPs−Au Janus HNs.

4.2.3 Upgraded TiO_2−Au Janus HNs using two-step anodization

Considering that the over-etching process will expose not only the desired four edges of the nanocomponent in A-pores, but also the undesired tip of the nanocomponent, it might be difficult to construct desired HNs when some other semiconductor and metal are integrated in A-pores. For example, when SnO_2 NTs were deposited in A-pores, instead of depositing pre-defined Au NRs in B-pores, randomly distributed Au NPs were observed on the tips of SnO_2 nanotubes after the same processes as that for the TiO_2−Au Janus HNs (Figure 4-15). As SnO_2 has a better conductivity than TiO_2, the electrodeposits will preferentially initialize and grow at the exposed tips of the SnO_2 NTs. To insulate the tip of SnO_2 NTs from the electrodeposition process, an additional cap is needed.

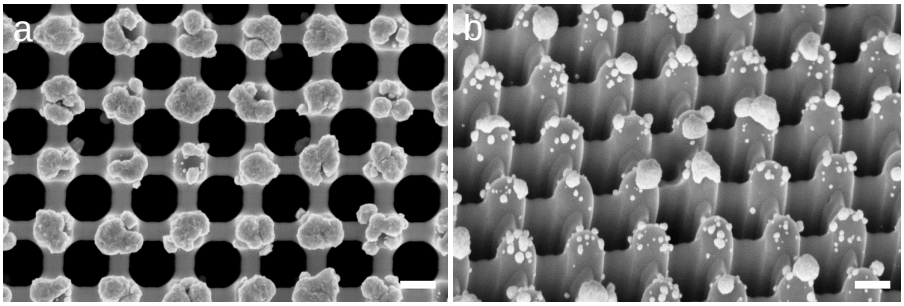

Figure 4-15. SEM images of an over-etched SnO_2 NTs. (a) Top and (b) tilted view SEM images of an over-etched SnO_2 NTs, where random-sized Au NPs were observed on the exposed tips of SnO_2 NTs with a 10 min Au electrodeposition. Scale bars: 200 nm

Thus, a two-step anodization was carried out to grow a template with dual-diameter A-pores, which resulted in a variable wall thickness from ~73 nm in the bottom-segment to ~152 nm in the top-segment along the pore axes (Figure 4-16a). Consequently, the B-pores could also be selectively etched on the dual-diameter templates with and without A-pores filled with SnO_2 NTs (Figure 4-16b-d). Most importantly, the four edges of the large-diameter SnO_2 NTs at the bottom-segment could be exposed after over-etching while the small-diameter SnO_2 NTs at the top-segment were still wrapped by the remaining barrier layer (Figure 4-16c-d).

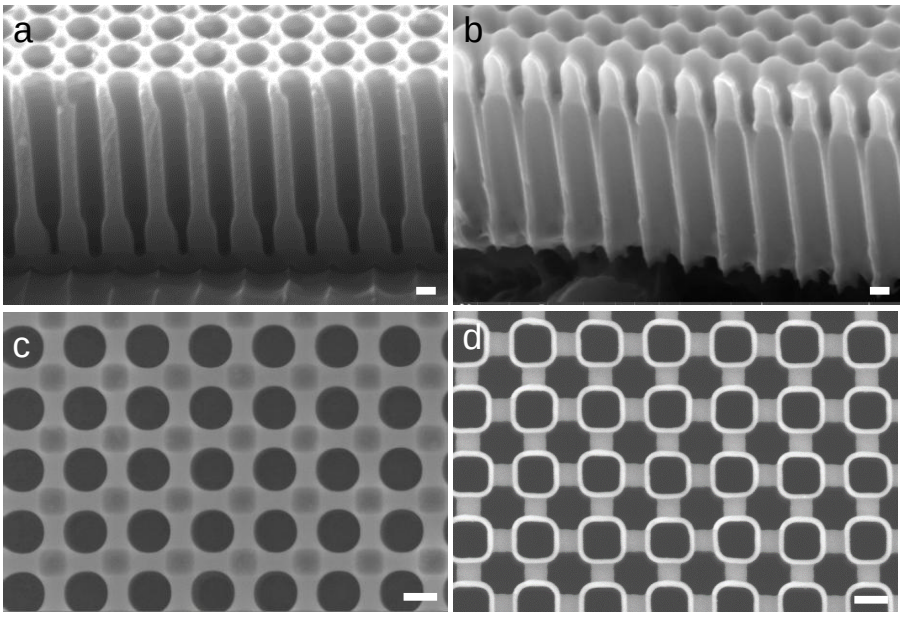

Figure 4-16. SEM images of AAO templates. (a) Dual-pore AAO template after a two-step sequential anodization, which includes first-step anodization (15 min), pore-widening (1 h),

and second-step anodization (3 min). Selective etching of B-pores: bare AAO template (b); AAO template with SnO_2 filled in A-pores (c) top-segment with remaining barrier layer and (d) bottom-segment with over-etched B-pores. Scale bars: 200 nm

Because of the isolation from the remaining barrier layer at the top-segment, the Au electrodeposition will be restricted in B-pores to form a desired SnO_2−Au interface (Figure 4-17a). An array of SnO_2−Au HNs is presented after removal of the remaining template, where their four edges about 1.5 μm length at the bottom-segment are intimately connected while their top-segment of ~300 nm in length is physically separated from each other (Figure 4-17b). Furthermore, we could also expand the options of the Janus HNs by taking other advantages of the two-step anodized template. For example, the length and diameter ratios of the top- and bottom-segments in A-pores could be designed and realized by using different anodizing and pore widening duration, as well as the length and diameter ratios of the two segments in B-pores could also be defined with different electrodeposition and etching time (Figure 4-17c). Therefore, customized Janus HNs with a greater freedom for each nanocomponent and their interface become feasible when an upgraded two-step anodization is involved in the fabricating process.

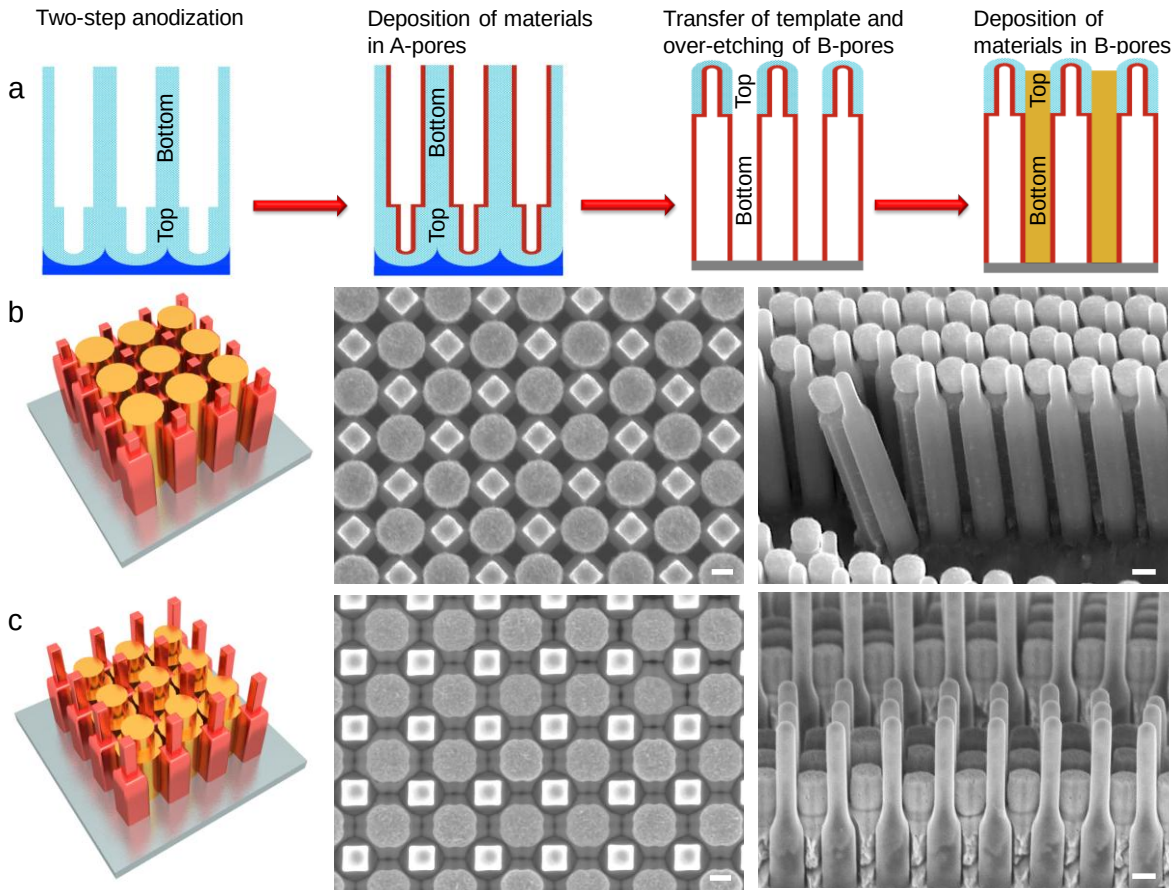

Figure 4-17. Janus HNs based on an upgraded two-step anodization. (a) Schematic flow diagram of the fabrication process. Illustrations and corresponding SEM images of the SnO_2−Au Janus HNs with different diameter and length ratios from top- to bottom-segment (top: bottom), including length ratios of SnO_2 NTs (b) 1:5 and (c) 1:1, diameter ratios of SnO_2 NTs (b) 1:2 and (c) 1:2, length ratios of Au NRs (b) 1:5 and (c) 1:2, and diameter ratio of Au NRs (b) 1:1 and (c) 1:1.6, respectively. Scale bars: 200 nm.

4.2.4 PEC performance of TiO_2−Au Janus HNs

The most exciting feature of the TiO_2−Au Janus HNs is their ability to improve the photo-conversion efficiency. Firstly, the TiO_2 NT length was rationally chosen to 2 μm, as it has been reported that 2 μm is the maximum penetration depth of the incident light in TiO_2, and any further increase of NT length would increase its electronic resistance while without the benefit of enhanced light capture.[149-151] Meanwhile, to minimize the negative effects of incorporating Au NRs, the Au NR length was also carefully considered with the assistance of

FDTD simulation. The simulated spectra indicated that with the increase of Au NR length, the light absorption of TiO_2 NTs in the TiO_2−Au Janus HNs began to decrease and would be seriously compromised when the Au NR length was increased to 2 μm (Figure 4-18a). While only small variation was observed regarding the visible light absorption of Au NRs with different length (Figure 4-18b). With a proper Au NR length of 800 nm, the electric field distribution revealed that most of the UV light was absorbed by the TiO_2 NTs above the top of Au NRs and no obvious difference was observed with or without incorporating Au NRs (Figure 4-18c-d). Therefore, the TiO_2 (2 μm)−Au (800 nm) Janus HNs was selected to demonstrate the plasmonic photocatalysis.

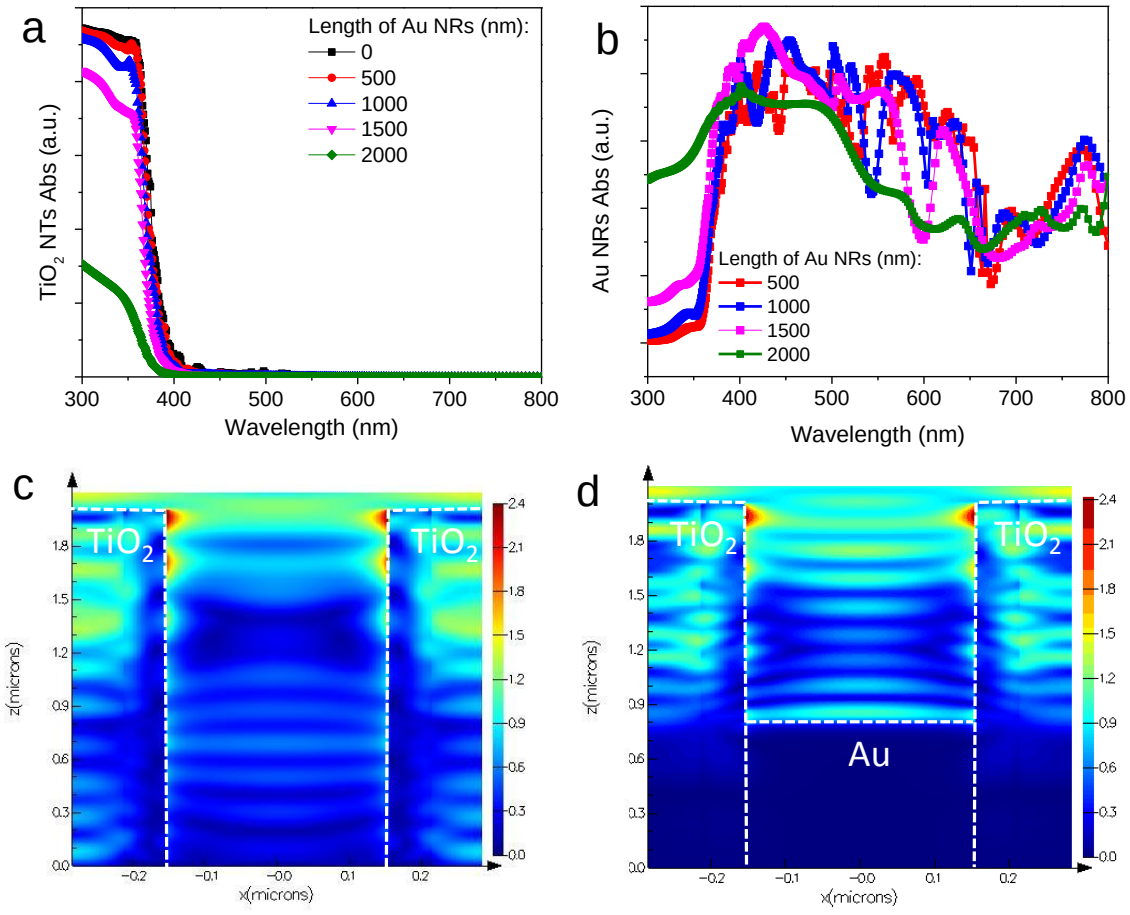

Figure 4-18. FDTD simulated absorption spectra and electric field distributions for Janus HNs. FDTD simulated absorption spectra of (a) TiO_2 NTs and (b) Au NRs in the TiO_2−Au

HNs with different lengths of Au NRs. FDTD simulated electric field distributions of (c) TiO_2 NTs (2 μm) and (d) TiO_2 (2 μm)−Au HNs (800 nm) at the wavelength of 350 nm.

Figure 4-19a shows chopped photocurrents of the TiO_2−Au Janus HNs and TiO_2 NTs under AM 1.5G illumination (100 $mWcm^{-2}$) with and without a 420 nm long-pass filter. The photocurrent of the TiO_2−Au Janus HNs reached to about 1.7 mA cm^{-2} at 1.23 V (vs. RHE) under AM 1.5G illumination, which was about 2.5 times of that from the TiO_2 NTs. Meanwhile, the TiO_2−Au Janus HNs showed an obvious visible light response with a density of 0.2 mA cm^{-2} at 1.23 V (vs. RHE), while no visible light response was found for the TiO_2 NTs. To further elucidate the role of Au NRs, the IPCE spectra of the TiO_2−Au Janus HNs and TiO_2 NTs were collected (Figure 4-19b). The IPCE spectra revealed that the observed photoconversion was dominated by the photoactivity of TiO_2 in the UV region, where the TiO_2−Au Janus HNs showed a much higher and broader spectrum comparing with the TiO_2 NTs. Meanwhile, an obvious IPCE spectrum in the visible region was also observed with a peak of 1.21% at around 540 nm (inset of Figure 4-19b), which might be ascribed to the plasmonic energy transfer from the Au NRs to the TiO_2 NTs at the energies below the band edge of TiO_2 through hot electron injection.[134, 151-155]

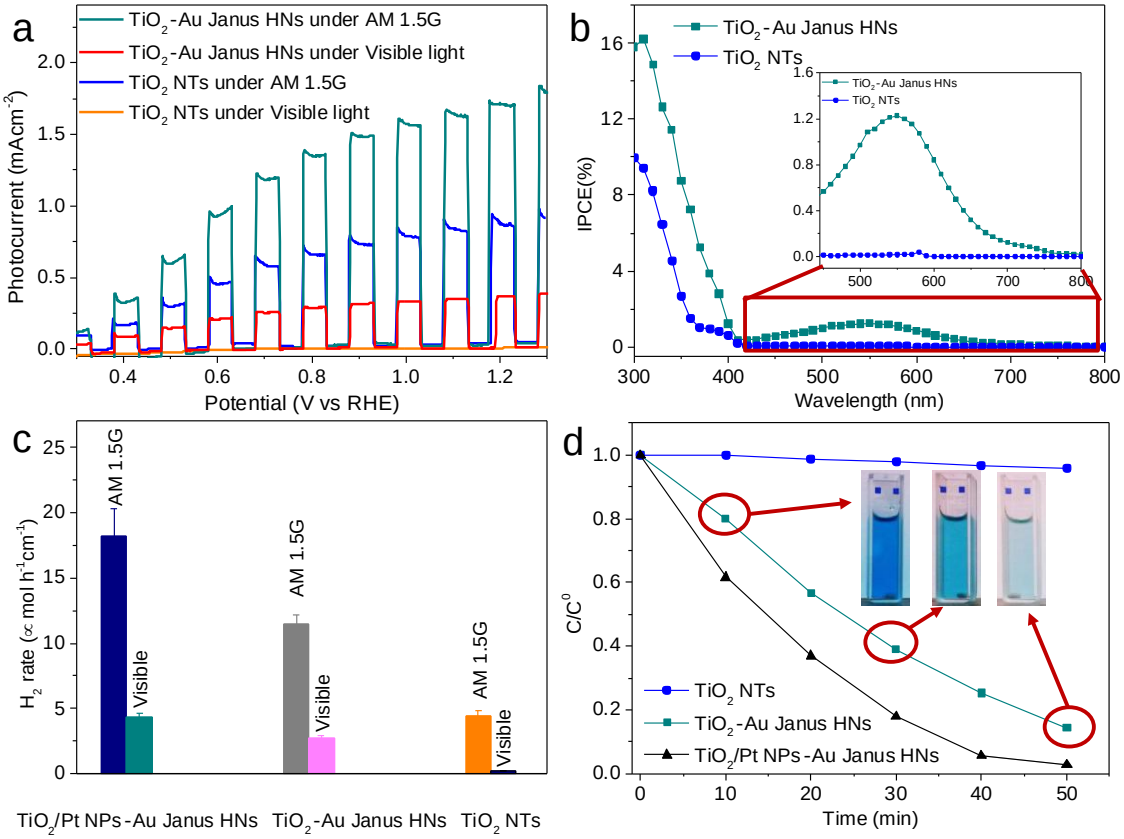

Figure 4-19. Photoactivities of Janus HNs. (a) Chopped photocurrents of TiO_2−Au Janus HNs and TiO_2 NTs under AM 1.5G and visible light illumination. (b) IPCE spectra of TiO_2−Au Janus HNs and TiO_2 NTs in the range of 300−800 nm without applying external bias. (c) H_2 evolution rate of three samples (TiO_2/Pt−Au Janus HNs, TiO_2−Au Janus HNs, and TiO_2 NTs) under AM 1.5G and visible light illumination. (d) Visible light driven photodegradation of MB. Inset: photos of the reduction of MB dye with the TiO_2−Au Janus HNs after different periods of time.

It is important to directly examine the evolution of H_2 gas. Under AM 1.5G illumination, the TiO_2−Au Janus HNs presented about three times H_2 evolution rate (12.8 ± 1.5 $\mu molh^{-1}cm^{-2}$) as compared to that of the TiO_2 NTs (4.8 ± 0.6 $\mu molh^{-1}cm^{-2}$). When Pt NPs (~2 nm) were incorporated as a co-catalyst to form TiO_2/Pt NPs−Au Janus HNs, the H_2 evolution rate was further increased to 17.5 ± 2.6 $\mu molh^{-1}cm^{-2}$ (Figure 4-19c). More importantly, the TiO_2/Pt NPs−Au and TiO_2−Au Janus HNs showed an obvious H_2 evolution under visible light illumination, while ignorable H_2 was detected from the TiO_2 NTs, proving

the evidence of hot electron injection. The different H_2 evolution rate for the TiO_2/Pt NPs−Au (4.3 ± 0.4 μmolh^{-1}cm^{-2}) and TiO_2−Au (3.1 ± 0.3 μmolh^{-1}cm^{-2}) Janus HNs indicated that the Pt NPs improved the collection of hot electrons. Hot electron injection was also demonstrated by visible light photoreduction of MB, a model acceptor molecule (Figure 4-19d). After 50 min of visible light irradiation, the TiO_2/Pt NPs−Au and TiO_2−Au Janus HNs exhibited ~96% and 80% reduction of the MB dye (Figure 4-19d), while TiO_2 NTs showed insignificant activity (less than 3%, part of the activity may come from photobleaching).[156, 157]

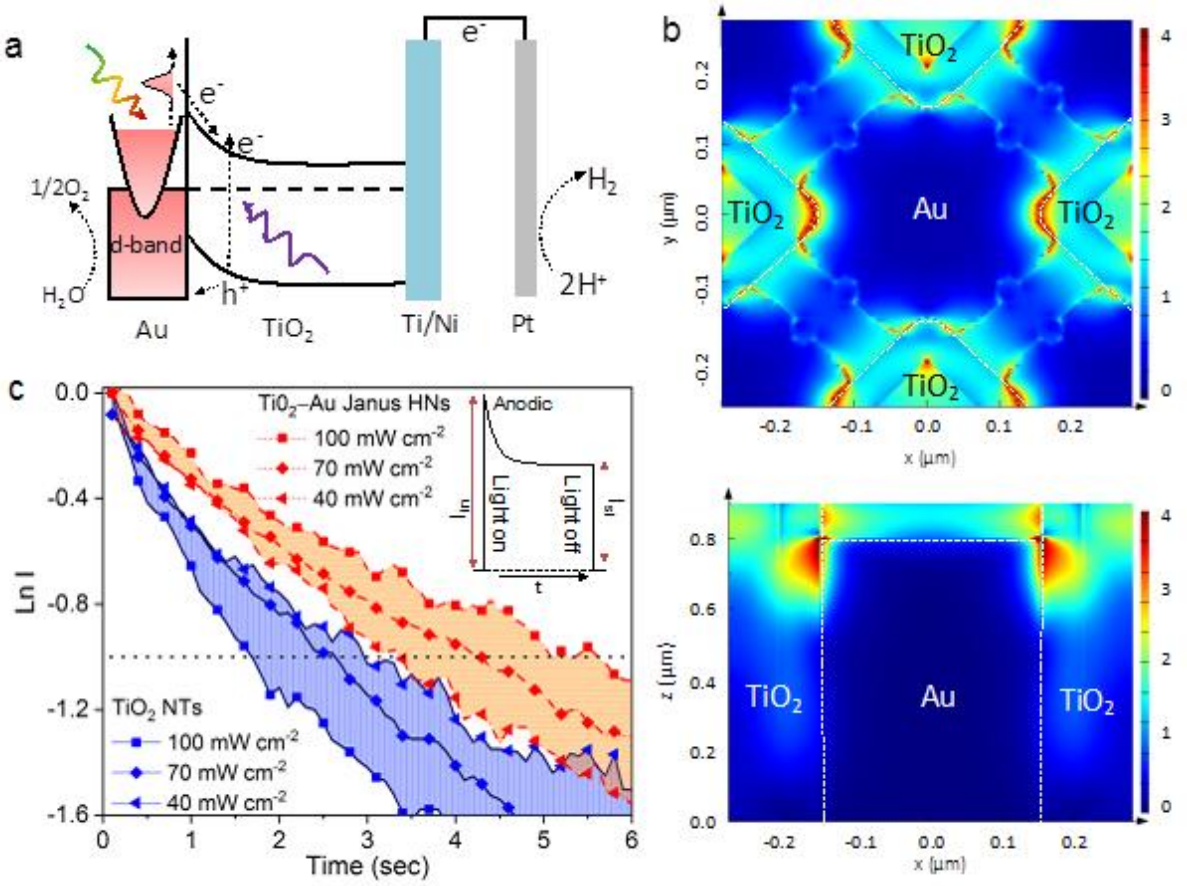

Figure 4-20. Photocarrier transfer paths. (a) Schematic of the possible photocarrier transfer paths involved in the TiO_2−Au Janus HNs. (b) FDTD simulated electric field distribution at 540 nm. Top: top-down view; Bottom: cross-sectional view. (c) Anodic transient dynamics under AM 1.5G with different irradiation intensities. Inset: the scheme for the calculation of the transient dynamics.

Based on the above results, we postulated the major photocarrier transfer paths involved in the TiO_2−Au Janus HNs (Figure 4-20a). On one hand, the significant IPCE improvement in the visible region was ascribed to the hot electron injection. This behavior can be seen in a simple FDTD model consisting array of TiO_2−Au Janus HNs at 540 nm (Figure 4-20b). The LSPR created a strong local field distribution $|E/E_0|^2$ that spans over the whole thickness of the TiO_2 NTs and a large part of the interface. When the field distribution was extracted versus the wavelength, it was seen that the intensity of the local field is peaked around 540 nm and becomes weaker at the shorter and longer wavelengths (Figure 4-21), which closely correlate with the measured absorption spectrum of the TiO_2−Au Janus HNs (Figure 4-22). This confirms that the photocarrier transfer in the visible region is originated from the LSPR effect induced hot electron injection.

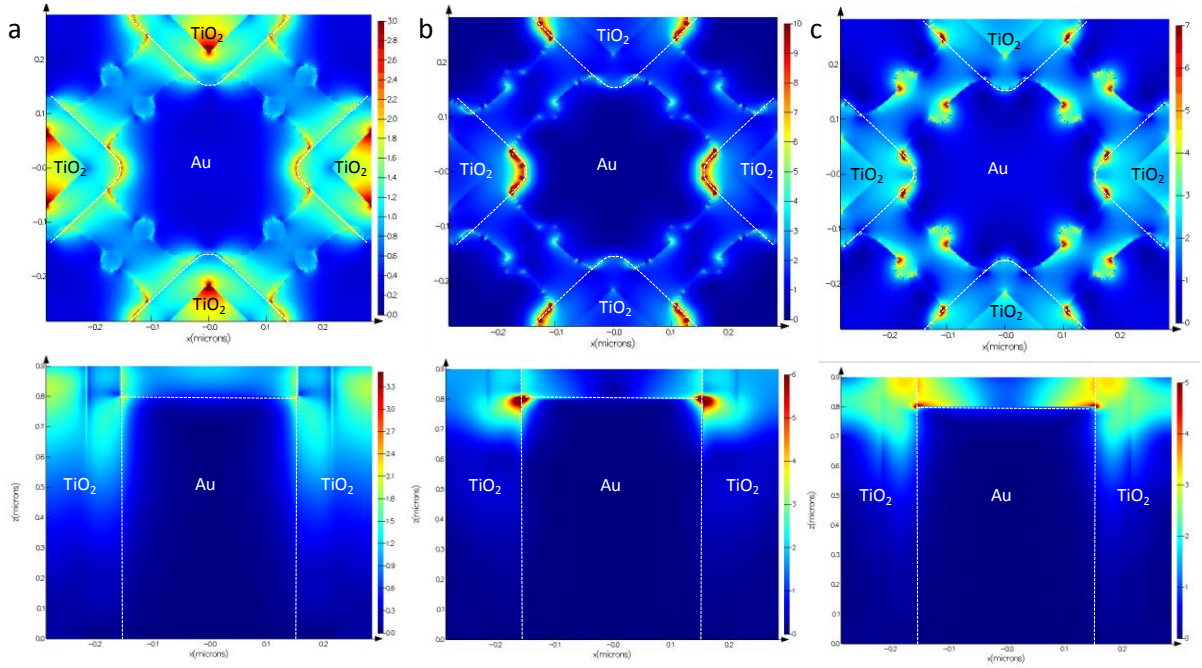

Figure 4-21. FDTD simulated electric field distributions of the TiO_2−Au Janus HNs at different wavelength: (a) 500 nm, (b) 580 nm, and (c) 620 nm.

On the other hand, since the light absorption of the TiO_2 NTs showed no obvious difference with or without Au NRs, the IPCE enhancement in the UV region should be ascribed to other reason. From the photocurrent transient measurement, it indicates that the

Au NRs could increase the charge separation and suppress the charge recombination of the TiO_2−Au Janus HNs under illumination, which leaves long-lived holes in TiO_2 to oxidize water and increases the photocatalytic water splitting rate. To quantitatively determine the charge recombination behavior, a normalized parameter D is introduced:

$$D = (I_t - I_{st})/(I_{in} - I_{st}) \quad (2)$$

where I_t, I_{st} and I_{in} are the time-dependent, steady-state and initial photocurrent, respectively, as shown in inset of Figure 4-21c.[158] The transient time constant (τ) is defined as the time when *lnD = -1* in the normalized plots of *lnD* – t, which reflects the general behavior of charge recombination and lifetime of the charge carrier. τ was estimated to be 5.2 s for the TiO_2-Au HNs under the illumination of 100 $mWcm^{-2}$, which was about three times of the TiO_2 NTs (1.7 s), indicating the suppressed carrier recombination.[159, 160] Moreover, differing from the conventional phenomenon observed for the TiO_2 NTs, the lifetime of the charge carriers for the TiO_2-Au HNs increased with the increase of light intensity (Figure 4-20c). Considering that the local electric field gradient is proportional to the light intensity, the resultant stronger LSPR along the interface caused a better suppression of charge recombination, which was supposed to be the major reason of the photoactivity enhancement in the UV region. Therefore, the formed plasmonic TiO_2-Au Janus HNs could not only extend the light collection in the visible range, but also enhance the light utilization in the UV range.

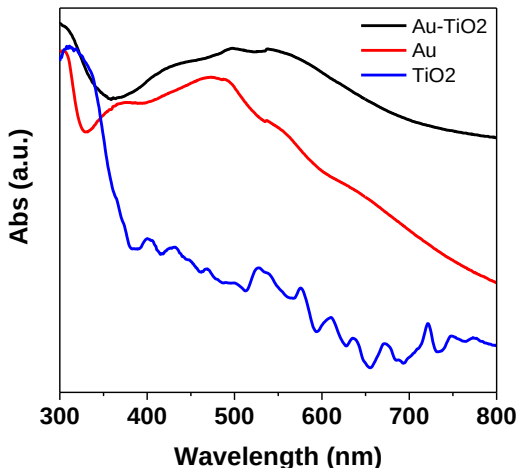

Figure 4-22. Diffuse reflectance UV−vis absorption spectrum of TiO_2 (2 μm)−Au HNs (800 nm) Janus HNs, TiO_2 NTs (2 μm), and Au NRs (800 nm).

4.2.5 Conclusion

In summary, we have developed a generic and efficient strategy to fabricate large-scale arrays of customized Janus HNs based on one- and two-step anodized binary-pore templates. Each nanocomponent of the Janus HNs were precisely programmed with pre-determined size, shape, composition, dimension, and interfaces at different processing step ranging from the anodization, pore-widening, over-etching, to material deposition. As a demonstration, rationally selected TiO_2-Au and TiO_2/Pt NPs-Au Janus HNs were used for plasmonic photocatalysis and exhibited superior performance to the TiO_2 NTs, which was ascribed to the LSPR effect induced direct hot electron injection and suppression of charge carrier recombination. It is clear that a further improvement on Janus HNs based plasmonic photocatalysis could be expected by tuning each nanocomponent and their interface,[161] as well as incorporating proper co-catalysts for each nanocomponent.[148] Multi-component arrays of customized HNs with an excellent integrity could be realized in conjunction with other template based nanostructuring strategies such as on-wire[162] and coaxial[163] lithography. The enabled heterogeneous nanoarchitectures demonstrated here could allow us to study the structure–property relationship from the fundamentally single microscopic HN to assembled macroscopic HN arrays at large scale.

4.3 Scalable fabrication of geometry-tunable self-aligned 2D superlattice photonic crystals for spectrum-programmable light trapping

4.3.1 State of the art

Photonic nanostructures have been widely exploited to trap light in the fields of optics, optoelectronics, and solar energy harvesting, etc [1, 164-166]. Considering that the light trapping property of a photonic architecture is highly dependent on its photonic density of states [167, 168], photonic crystals (PhCs) are believed to be promising nanostructures for engineering light absorption performance due to their outstanding capabilities in modulating the photonic density of states [169-171]. Beyond the conventional PhC with an array of structural units, superlattice PhCs (SPhCs) including multiple sets of structural subunits have been proposed, which are theoretically predicted to possess elevated photonic density of states because of the Brillouin zone folding effect arising from the lattice symmetry reduction and anisotropy introduction in the lattice, thus possessing superior light trapping capability [172-174]. For example, Callahan et al. and Tanaka et al. theoretically demonstrates that silicon photovoltaic devices decorated with 2D SPhCs consisting of two sets of nanopores (NPs) can achieve broadband light absorption enhancement [175, 176]. And strong light absorption was also numerically obtained over broader spectral regions for 2D tantalum SPhC solar absorber because the diffraction loss limiting the absorption efficiency of the PhC counterparts was overcome by the synergistic contribution of cavity resonance modes in two sets of NPs, as demonstrated by Rinnerbauer et al. [177]. For in-depth fundamental research and practical application of such SPhCs, it is imperative to develop an approach to fabricate large-scale highly-ordered SPhCs to obtain a uniform optical response. Meanwhile, this method should allow for precise geometrical modulation towards realizing desired optical properties to satisfy different practical requirements. At present, the techniques for fabricating such 2D SPhCs are mostly restricted to EBL and focused ion beam (FIB) approaches which both are time-consuming, high-costly and thus not suitable for scale-up fabrication [174, 178, 179]. To our

best knowledge, the maximum area of the ever-reported SPhCs is only ~10 mm^2 [180]. Although the multistep lithography is suitable for mass production, mismatching errors between different lithographic steps will be generated, leading to inhomogeneous optical performance. In general, efficient techniques for fabricating large-area SPhCs with precise geometrical tunability and reliable structural uniformity are still lacking.

In this section, we develop a template-assisted route to fabricate wafer-scale highly-order 2D SPhCs with prominent geometrical tunability. For demonstration, the cheap nickel (Ni) was selected as the active material of SPhCs and the as-replicated Ni SPhCs were exploited as optical absorber to boost solar-to-thermal energy conversion. The fabrication of Ni SPhCs was based on a structural replication process starting from AAO templates with two arrays of NPs [146]. We showed that the size, depth, and morphology for each set of NPs in the dual-pore Ni SPhC can be independently controlled. Furthermore, Ni SPhCs consisting of NPs and nanodents (NDs) were fabricated where NPs and NCs are simultaneously formed and can be geometrically modulated together. Taking Ni SPhC with 800 nm periodicity as an example, we observed omnidirectional stably-strong light absorption (about 95%) arising from cavity resonance and SPR. We then generalized the fabrication technique to Ni SPhCs with other periodicities (400, 600, and 1000 nm). By virtue of the prominent light trapping performance, we finally utilized Ni SPhCs as solar absorber to boost the performance of a solar steam generation system and a solar thermoelectric generator. This work not only demonstrates a versatile approach to fabricate SPhCs with selectable materials and with tunable NP geometries but also provide a conceptual blueprint for geometrically designing SPhCs to achieve superior light absorption.

4.3.2 Synthesis and characterization of metallic superlattice photonic crystals

Ni SPhCs were fabricated through a structural replication process to replace AAO templates with the Ni material. The detailed fabrication process is introduced in the Supporting Information. Briefly, the fabrication process includes seven steps, as summarized

in Figure 4-23a. Firstly, anodic anodization of Al foils decorated with squarely-arranged nanodent (ND) array gave rise to periodic square NPs (named 'A NP') at the ND positions and another array of circular NPs (named 'B NP') [181, 182]. The B NPs were blocked from the electrolyte by a thick alumina membrane [146]. Figure 4-23b and c demonstrate the top-view and tilt-view scanning electron microscope (SEM) images of an AAO template after opening B NPs. Intriguingly, the B NPs are always situated at the junction sites of four neighboring A NPs. As can be seen in Figure 4-23f, stronger anodization electric fields occur at both the pre-patterned NDs and the fourfold junction sites where A NPs and B NPs locate respectively, implying that periodic electric fields result in the NP alignment because the anodization electric fields dominate over the anodic oxide growth [49]. The NP self-alignment induced by the periodic electric fields avoids otherwise mismatching errors between two sets of NPs in conventional multi-step lithography and thus benefits to obtaining uniform structures for scale-up production as evidenced by the large-area SEM image in Figure 4-23h. In cooperation with a structural replication process, a Ni SPhC was finally obtained. As illustrated in Figure 4-23d and e, the as-replicated Ni SPhC inherits almost all geometrical features of the AAO template, illustrating that Ni SPhCs can be geometrically modulated by designing the corresponding geometrical parameters of the original AAO template. The cross-sectional SEM image of the Ni SPhC demonstrates that both NPs are of the same pore depth which can be precisely designed by controlling the anodization time (Figure 4-23g). Notably, considering that the nanoimprinting moulds for generating ND array on Al foils are obtained by the interference lithography technique which allows for large-area fabrication and that two sets of NPs are self-aligned, highly-ordered large-scale (e.g., wafer scale) Ni SPhCs are realizable.

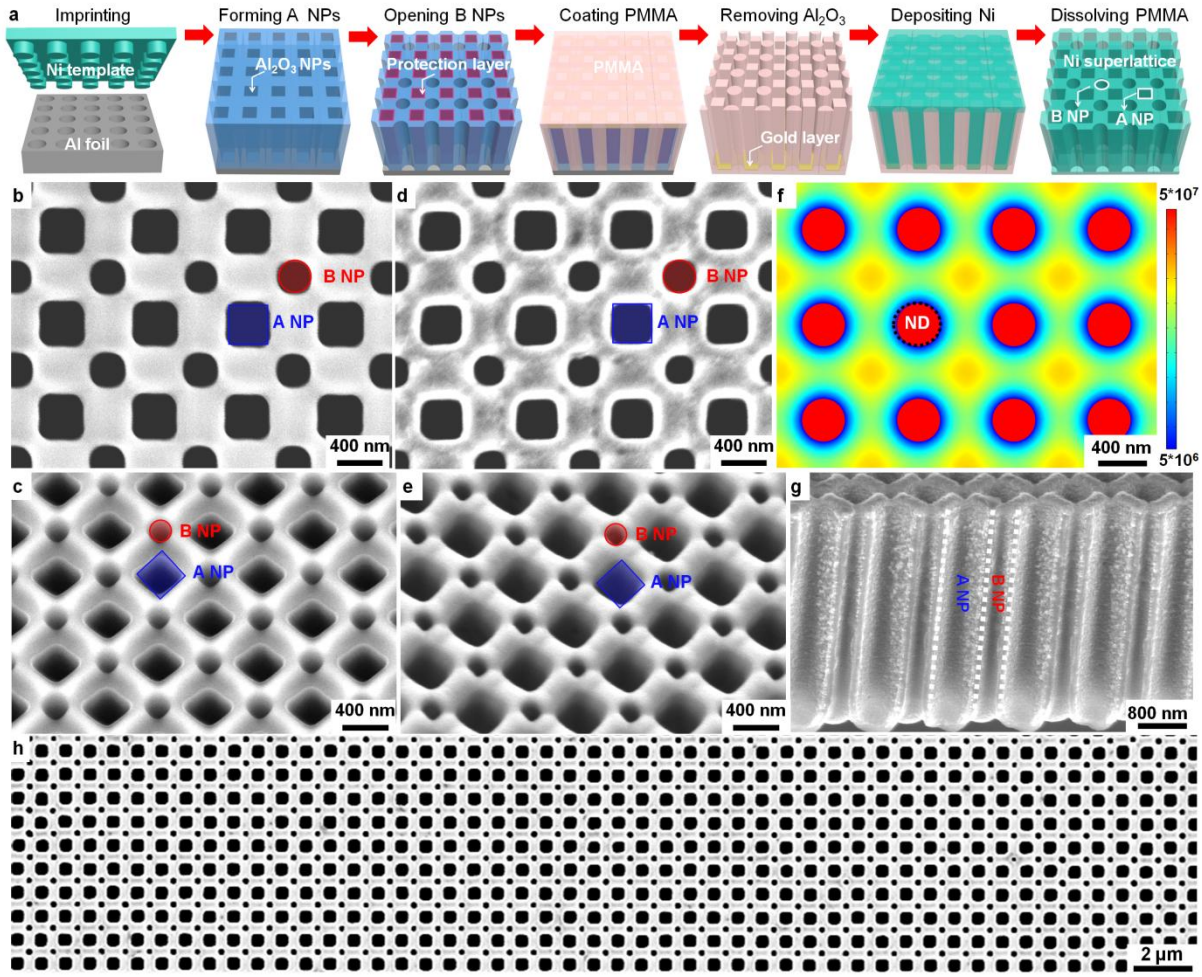

Figure 4-23. Fabrication and structural characterization of Ni SPhCs. (a) Schematic drawing of fabrication process for Ni SPhCs. (b) Top- and (c) tilt- view SEM images of AAO template. (d) Top- and (e) tilt- view SEM images of Ni SPhC. (f) COMSOL simulated electric field distribution at the top surface of nanopatterned Al foil when an external bias is applied to the aluminum for anodization. (g) Cross-sectional-view SEM image of Ni SPhC. (h) Large-scale SEM image of Ni SPhC. The Ni SPhC has a periodicity of 800 nm.

4.3.3 Optical optmization of metallic superlattice photonic crystals

Because the optical property of a nanophotonic structure is usually dependent on its geometry [183-185], here we modulate the light trapping performance of Ni SPhCs through changing the pore size, morphology, and depth. Due to the sequential pore-opening with the assistance of the thick membrane locating at the top surface of B NPs (Figure 4-23a), the sizes of A NPs and B NPs in the AAO template and the Ni SPhC counterparts can be independently

tuned by controlling the wet-chemical etching time. It is worth noting that so as to prevent the AAO membrane from cracking due to the H_2 bubbles formed during the wet-chemical etching, the concentrations of the etching solutions need to be low enough to decrease the H_2 generation rate, for example, 0.025 mol/L for sodium hydroxide solution and 0.1 mol/L for phosphoric acid solution. Figure 4-24a and b demonstrate the top-view SEM images of Ni SPhCs with different-size A NPs. With the increase of A NP size, the light absorption efficiencies are improved and the cutoff wavelengths are red shifted (Figure 4-24c).

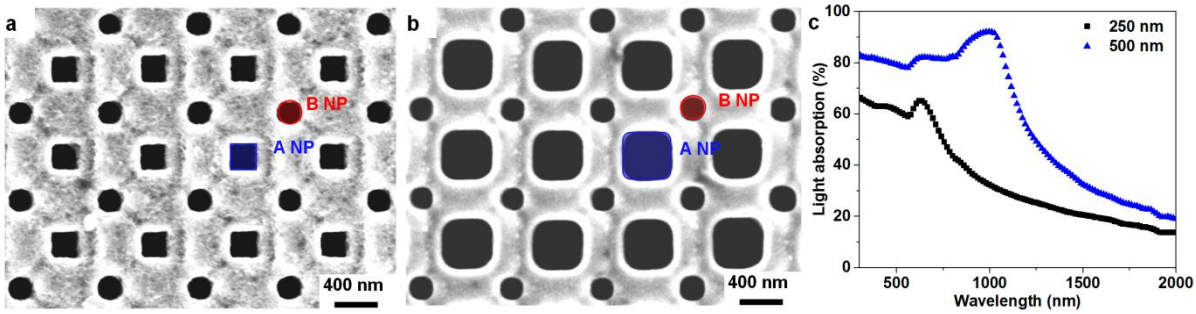

Figure 4-24. Pore-size modulation of Ni SPhCs. Top-view SEM images of Ni SPhCs with different A Pore sizes: (a) ~250 nm and (b) ~500 nm. (c) Light absorption spectra of Ni SPhCs with different A NP sizes: ~ 250 nm and ~ 500 nm.

In addition, by virtue of the inhomogeneous etching rate for the side walls of B NPs of the AAO template in phosphoric acid solutions, the morphology of B NPs was further tuned from circle to circles with bulgy edges. As compared with the Ni SPhC with circular B NPs, Ni SPhCs with sharply-edged B pores shown in Figure 4-25a and b demonstrate obvious improvement in the light absorption at short wavelengths (Figure 4-25c). To elicit the cause for the light absorption enhancement, the electric fields in Ni SPhCs were calculated using FDTD method. Figure 4-25d and e show that strong electric fields locate in the vicinity of the bulgy edges of B NPs, confirming that sharp edges are helpful for improving the light absorption.

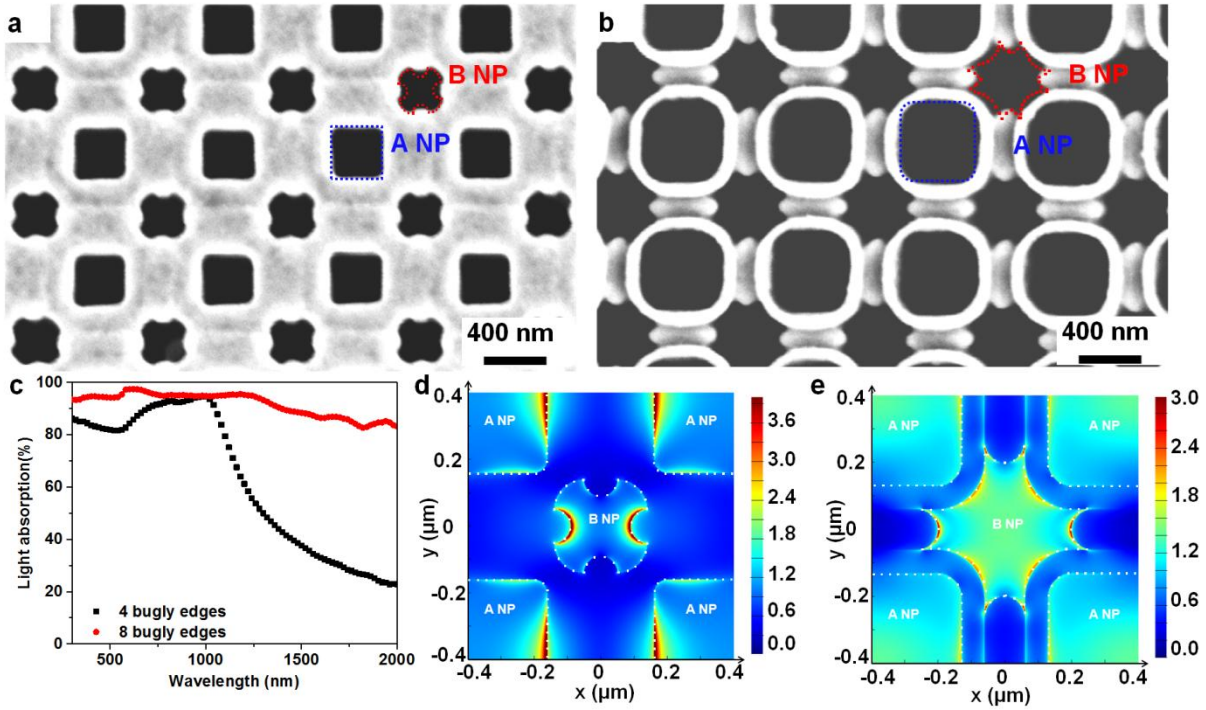

Figure 4-25. Pore-morphology modulation of Ni SPhCs. Top-view SEM images of Ni SPhC with B pores owning (a) four and (b) eight bulgy edges. (c) Light absorption spectra of Ni SPhCs. Electric filed distributions at the top surfaces of Ni SPhCs owning (d) four and (e) eight bulgy edges illuminated by 600-nm-wavelength light.

Finally, besides Ni SPhCs with the same pore depth, Ni SPhCs with different pore depths were also fabricated (Figure 4-26a). In contrast with the Ni SPhC with the same pore depth (Figure 4-23d), the Ni SPhC in Figure 4-26b owns different pore depths, for example, the depth of B NPs is about two times of that for A NPs. Intriguingly, both samples have similar light absorption performance (Figure 4-26c). To explain the microscopic origin, Figure 4-26d demonstrates the electric fields in dual sets of pores. Obviously, strong electric fields are only located around the top surface, especially in the small B NPs. Accordingly, the electric field intensities (E^2) in the small B NPs decrease by a factor of ~80% at -400 nm, unambiguously demonstrating that only the top parts of the small NPs contribute to the light absorption.

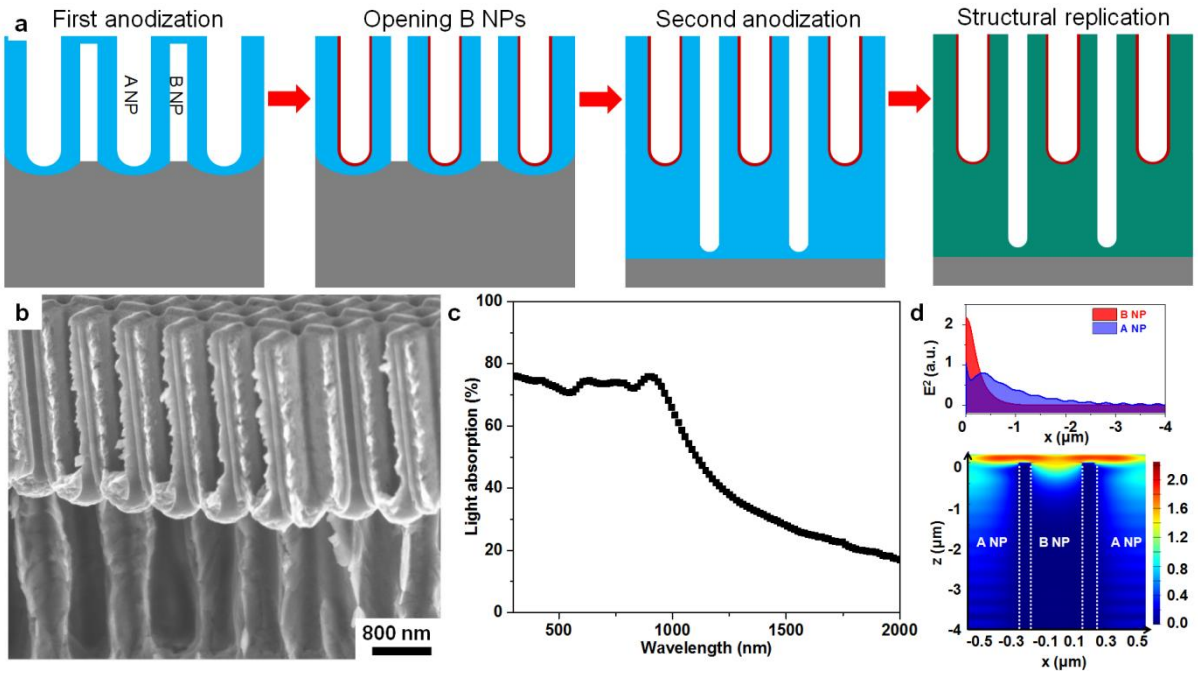

Figure 4-26. Fabrication and characterization of Ni SPhCs with different NP depths. (a) Schematic drawing of fabrication process. (b) Cross-sectional-view SEM image. (c) Light absorption. Inset: top-view SEM image. (d) Electric filed distribution in Ni SPhCs with the same pore depth (down) illuminated by 600-nm-wavelength light and electric filed intensities on the axes of both NPs (up).

Based on the aforementioned recognitions that large pores and sharp edges are in favor of light trapping and that shallow depth is sufficient for efficient light absorption in small NPs, Ni SPhCs consisting of large NPs, small NCs and breached side walls were fabricated. In addition to NPs at the ND zones, another set of shallow NCs which were isolated from the aforementioned B NPs by the barrier membrane were formed at the early stage of anodization (Figure 4-27a). Note that, the fabrication process for the NP-NC template was simplified with respect to that for the dual-pore template since the step for opening B NPs by argon ion milling was omitted. The NPs and NCs can be enlarged together in diluted phosphoric acid solutions, as illustrated in Figure 4-27a. According to the aforementioned strategy, the Ni SPhC consisting of deep NPs and shallow NCs was replicated, as illustrated in Figure 4-27b. The walls of NCs were partially breached at the every wall junction, thus realizing sharp

edges (Figure 4-27c). Figure 4-27d shows the cross-sectional SEM image and accordingly, the depths of NPs and NCs were measured to be ~4.5 μm and ~350 nm, respectively. Due to the fact that the Ni SPhC can be fabricated without rigid substrates and that the Ni film thickness can be precisely controlled by the electrodeposition time, the Ni SPhC saves weight and has reliable mechanical robustness which is suitable for flexible applications such as building integration (Figure 4-27e). Moreover, an optical photograph of a Ni SPhC with the same diameter of 1 inch as a two-Euro coin is presented. An overwhelming observation is a black surface, directly demonstrating prominent light absorption. As expected, steadily strong light absorption (~95%) is achieved at wavelengths below ~1200 nm for the Ni NP-NC SPhC (Figure 4-27e). In particular, the Ni SPhC demonstrates identical light absorption spectrum regardless of the polarization of the normal incidence (Figure 4-27f). In the meantime, approximately omnidirectional light absorption is observed (Figure 4-27g). Due to the fabrication difficulty reduction because of the simultaneous formation and geometrical modulation for dual sets of nanostructures as well as the strong capability in light trapping, we will focus on the Ni NP-NC SPhCs in the following sections.

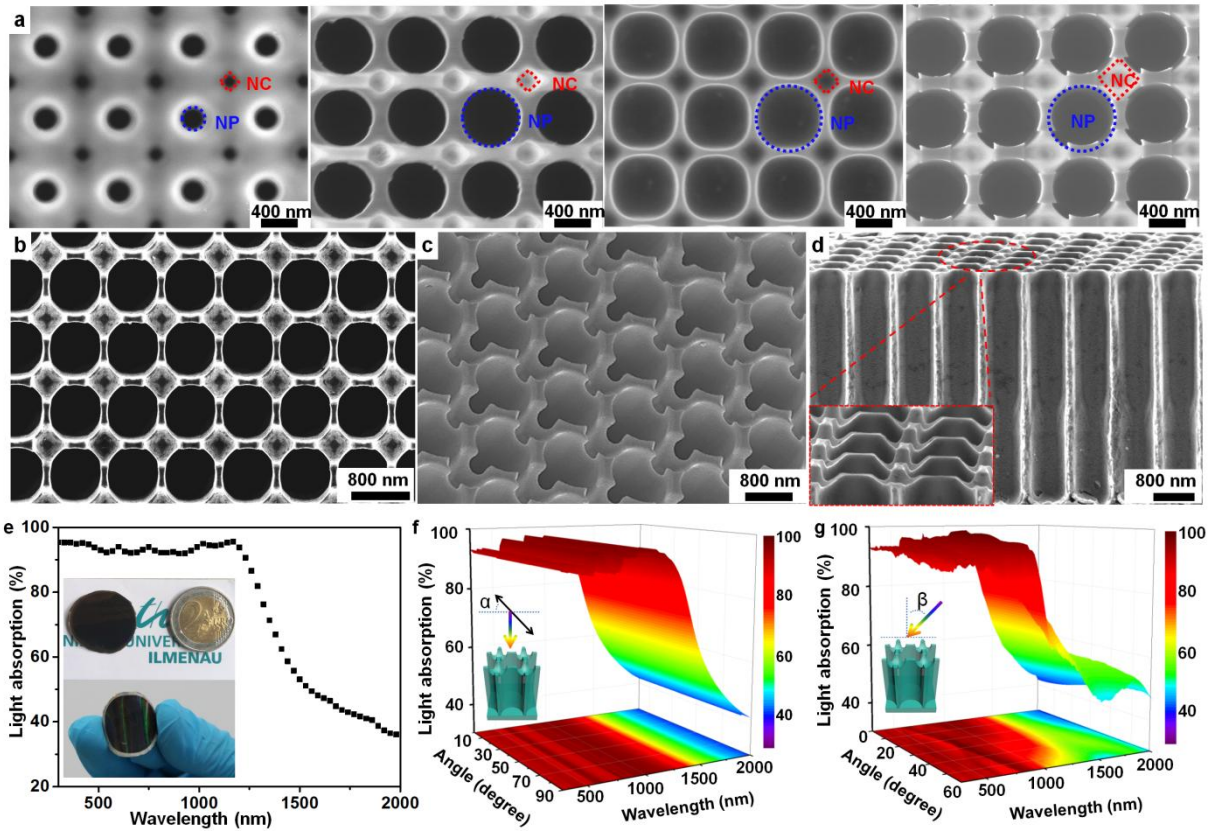

Figure 4-27. Structural and optical characterization of Ni NP-NC SPhC. (a) SEM images of AAO template after being etched in 0.5 M phosphoric acid solutions for (from left to right) 0 h, 3 h, 6 h, and 7h. (b) Top-, (c) tilt-, and (d) cross-sectional- view SEM images of Ni NP-NC SPhC. (e) Experimental light absorption spectrum of Ni NP-NC SPhC. Insets: Ni SPhC with a 1-inch diameter (up) and mechanical flexibility (down). (f) Theoretical light absorption spectra as a function of wavelength and polarization angle α. (g) Theoretical absorption spectra as a function of wavelength and incident angle β. The Ni SPhC has a periodicity of 800 nm.

To further shed light on the origins of the strong light absorption, the electric fields in the Ni NP-NC SPhC were calculated under the illumination with different wavelengths (400, 600, and 800 nm). As can be seen in Figure 4-28a, the cavity resonance always occurs. However, the cavity resonance is only observed in NCs at the short wavelengths of 400 and 600 nm (Figure 4-28b). Given that electromagnetic modes in cavities are represented as Equation 3 [186],

$$\lambda_{lmn} = \frac{2}{\sqrt{\left(\frac{m}{L_x}\right)^2 + \left(\frac{n}{L_y}\right)^2 + \left(\frac{2l+1}{2L_z}\right)^2}} \quad (3)$$

where L_{x-z} are cavity dimensions, and m, n, j are non-negative integers, the cutoff wavelength of the NCs should be ~720 nm as (m, n, j) = (1, 0, 0) and (L_x, L_y, L_z) = (420, 420, 350) nm, which is in accordance with the simulation result that cavity resonance at 800 nm is not observed. In the same way, the deep NPs should have the cut-off wavelength of ~1440 nm which is different from the experimental result of ~1250 nm (Figure 4-28b). This deviation can be ascribed to the fact that the NPs have imperfect rectangular morphology. Notably, the breached walls are characteristic of intense electric fields (Figure 4-28c), indicating that the localized SPR contributes to the light absorption [154, 187]. In addition, the propagating SPR plays important role in light trapping as well [188, 189]. To match the in-plane wave vector k_{spp} of propagating SPR and the wave vector k_0 of the incident light, the Ni SPhC should satisfy Equation 4 [190, 191],

$$k_{spp} = k_0 \sin\theta \pm n\frac{2\pi}{p} \quad (4)$$

where θ, n, k_0, p represent the incident angle of light, positive integers, the light wave vector in vacuum, the NP periodicity, respectively. As θ = 0 (for normal incidence), the active wavelength is ~800 nm (n = 1), which can be evidenced by the widespread intense electric fields moving downwards the bottoms of NCs (Figure 4-28b).

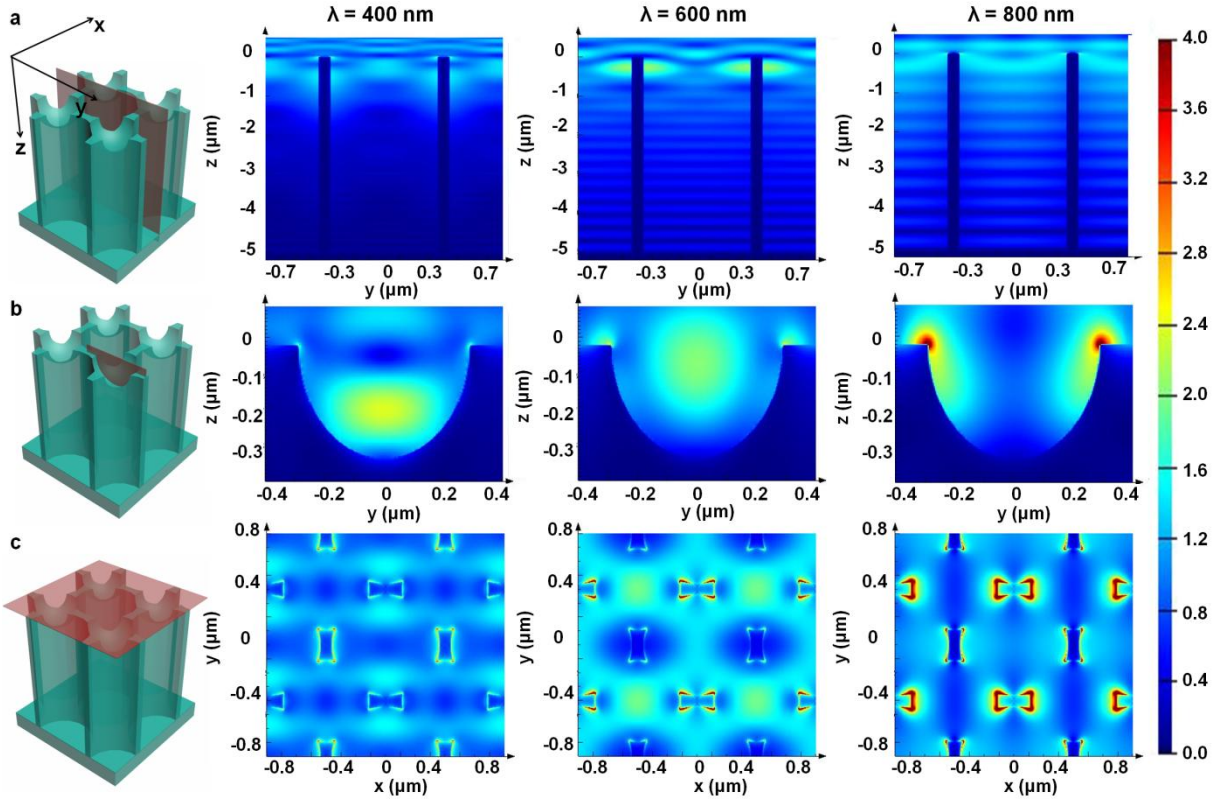

Figure 4-28. FDTD simulated electric field distributions for Ni NP-NC SPhC. Electric filed distributions at (a) the cross section in NPs, (b) the cross section in NCs, and (c) the top surface of the Ni SPhC under the illumination with various wavelengths (400, 600 and 800 nm). The red planes in the three-dimensional schematic drawing represent the cross section under investigation.

4.3.4 Application of metallic superlattice photonic crystals as spectrum-programmable solar absorbers

The prominent light trapping properties and mechanical robustness enable Ni SPhCs to serve as promising candidates for solar absorbers in the fields of solar steam generation, solar desalination, solar thermoelectrics, and solar thermophotovoltaics, etc. For diverse practical requirements, the light absorption spectra of solar absorbers need to cover different wavelength regions [192, 193]. In other words, the cutoff wavelengths of the absorption spectra need to be spectrally shiftable. Herein, we fabricated three more types of Ni SPhCs with the periodicities of 400, 600 and 1000 nm, respectively. The SEM images illustrate that the

features of NPs and NCs are still maintained regardless of the periodicity (Figure 4-29a-f). Similarly, these new samples demonstrate selectively enhanced light absorption and all absorption efficiencies below the cutoff wavelength are maintained ~95% (Figure 4-29g). The cutoff wavelength derived from Figure 4-29g is linear with the periodicity and is monotonically shifted from ~600 to ~1500 nm as the periodicity is increased from 400 to 1000 nm (Figure 4-29h).

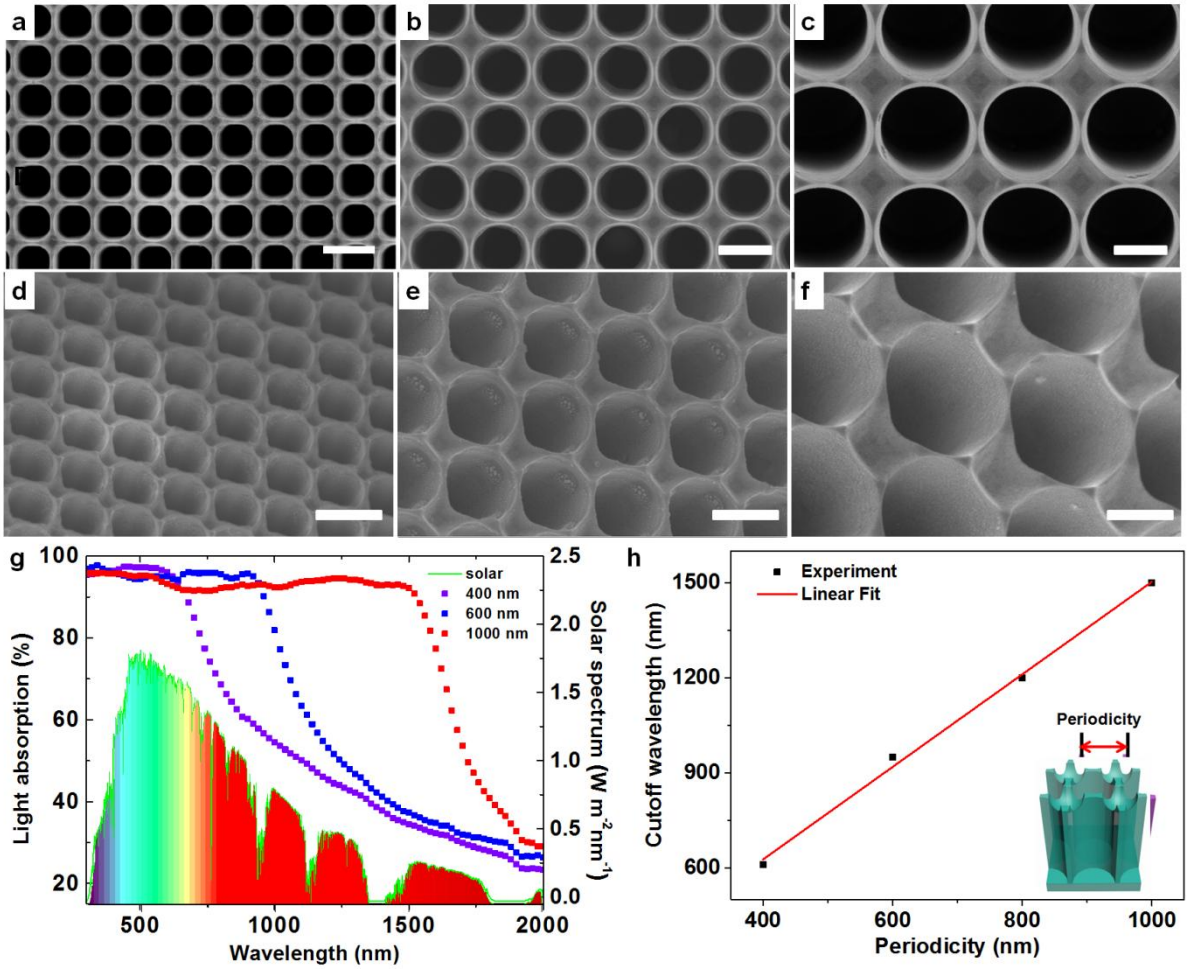

Figure 4-29. Structural and optical characterization of Ni SPhCs with different periodicities. Top-view SEM images of Ni SPhCs with the periodicities: (a) 400 nm, (b) 600, and (c) 1000 nm. Tilt-view SEM images of Ni SPhCs with the periodicities: (d) 400 nm, (e) 600, and (f) 1000 nm. (g) Experimental light absorption of Ni SPhCs with periodicities (400, 600, and 1000 nm) and AM 1.5G solar spectrum. (h) Cutoff wavelengths of absorption spectra as a function of SPhC periodicity. All scale bars: 500 nm.

In a solar steam generation system, the 1000-nm-periodicity Ni SPhC was exploited as solar absorber because of its broadband light absorption spectrum. Figure 4-30a shows the experimental water mass change as a function of time. With the Ni SPhC, the evaporation rate is 1.30 kg m^{-2} h^{-1} and accordingly, the steady-state evaporation efficiency was ~81.5% which is ~2.3 times of that without Ni SPhCs. Actually, there is no protection for the experimental set-up, and the evaporation efficiency can be further improved by minimizing the radial heat loss. The Ni SPhC was also chosen for promoting the performance of a thermoelectric generator. As the Ni SPhC was attached to the hot side of a thermoelectric generator, the open circuit voltage output increases to ~100 mV, while only ~40 mV for the reference with a Ni plane (Figure 4-30b). Although the enhanced performance was observed at low temperatures, raising work temperatures will dramatically increase the blackbody radiation loss and thus deteriorate the energy conversion performance of Ni SPhCs which is determined by the solar-to-thermal conversion efficiency (see calculation details in the Supporting Information) [78, 194]. Regarding the 1000-nm-periodicity Ni SPhC, the solar-to-thermal conversion efficiency of ~89% is calculated at 400 K due to the low emissivity of ~2% (Figure 4-30c), confirming the better performance of the solar steam generation system and the thermoelectric generator with Ni SPhCs. While the operational temperature is increased to 1800K, the solar-to-thermal conversion efficiency is decreased to 46% under 500 suns because the emissivity soars up to 36%. Spectrally-shiftable selective light absorption spectra of Ni SPhCs enable to overcome this dilemma by decoupling the competition between solar energy harvesting and thermal radiation loss. For example, the emissivity of the Ni SPhC with 600 nm periodicity is only 25%, and consequently the solar-to-thermal conversion efficiency of 53% is still maintained (Figure 4-30d). It is noteworthy that the energy conversion efficiency can be further optimized by virtue of the linear programmability of the cutoff wavelength with the SPhC periodicity.

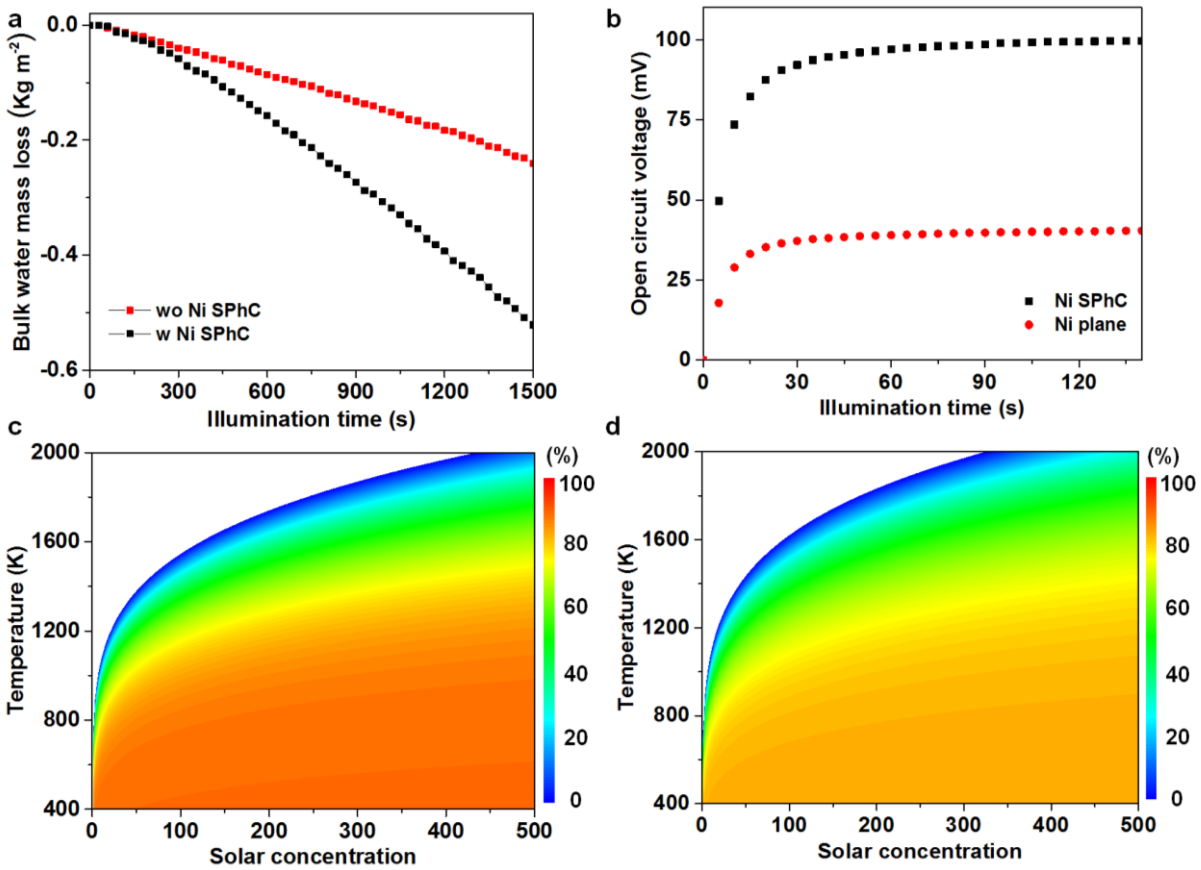

Figure 4-30. Solar energy harvesting with Ni NP-NC SPhCs as solar absorber. (a) Evaporation mass loss of water with/without Ni SPhC of 1000 nm periodicity under AM 1.5G solar radiation. (b) Time-dependent open circuit voltage output of thermoelectric generator with the Ni SPhC of 1000 nm periodicity and planar film illuminated by AM 1.5G solar radiation. Solar-to-thermal conversion efficiencies as a function of solar concentration and temperature for Ni SPhCs with (c) 1000 nm and (d) 600 nm periodicities.

4.3.5 Conclusion

In summary, we realized wafer-scale highly-ordered SPhCs using a scalable and precisely-tunable process. Firstly, we synthesized Ni SPhCs with dual self-aligned sets of NPs by virtue of the periodic anodization electric fields and found that large NPs and sharp edges are in favor of light trapping and that only top parts of small NPs contribute to light absorption. Thus, we then fabricated Ni SPhCs involving large NPs, shallow NCs, and breached side walls which were simultaneously formed, consequently decreasing the

fabrication complexity. By tuning geometrical parameters of Ni SPhCs such as the pore size, morphology, depth, and periodicity, we obtained spectrally-programmable stably-strong light absorption spectra which originate from the complementary collaboration between the SPR and cavity resonance. Specially, the light absorption performance was almost independent of the polarization and the incident angle which is crucial for practical utilizations in a wide geographical region. Besides the prominent optical performance, Ni SPhCs also demonstrate reliable mechanical robustness which both enable Ni SPhCs as ideal solar absorbers in the solar steam generation system and the solar thermoelectric system. More importantly, the spectrum-programmable light absorption spectra of Ni SPhCs can balance the tradeoff between light absorption and thermal radiation to optimize solar-to-thermal conversion efficiencies at different temperatures. Note that, the material should not be limited to Ni, other metals and even semiconductors which are suitable for ECD can also be chosen for fabricating functional SPhCs, thus providing considering scope for the utilization of SPhCs in optical, electronic, and magnetic devices. Therefore, we believe that these results will promote the exploration of new design and application of SPhCs.

CHAPTER 5. Summary and outlook

In this dissertation, I realized three kinds of highly ordered nanostructures including 1D PTP Au-core/CdS-shell array, Au-NW/TiO_2-NT janus hetero-nanostructure array, and 2D metallic SPhCs. These advanced architectures could be employed as versatile scaffolds to construct energy-related devices, and have great potentials to improve the overall performance dramatically and break the limits imposed by the planar configuration. In particular, the ordered nanostructure arrays with multiple components are of great significance, and the corresponding devices can combine the advantages of these nanostructuralized components, thereby beneficial to improving the relevant performance systematically. Moreover, the high regularity of the nanostructure distribution, the uniformity of the nanounits as well as the controllable sizes and profiles of the nanostructure enable the resulting architectures as a powerful platform to investigate the specific energy converting reactions microscopically. These results could, in turn, guide the further evolution of the relevant devices.

However, to meet the multiple requirements of the future energy market, some requisite efforts are still needed. First, modifications on surfaces or interfaces of the ordered nanostructures to reduce the surface recombination of charge carriers for energy conversion devices need more attention. This issue limits the further performance improvement for the corresponding devices, since enlarging the surface area would be unavoidable to cause a large density of surface states and defects. The second challenge is choosing different functional materials, organizing them to well aligned nanostructure arrays and making the corresponding devices perform efficiently. Though such issue has long been studied, the compatibility of each functional component still requires more work to optimize the overall performance systematically. Particularly, the band gap alignments of metal to semiconductors, semiconductor to semiconductor and semiconductor to electrolyte govern the photo conversion efficiency of the solar energy conversion devices. Third, comprehensive

understanding on the correlations of the geometrical parameters (e.g., size, morphology, and distribution) with the detailed processes for energy conversion is also required to give an essential guideline to the device design. The other challenge is fabricating the ordered nanostructure arrays on a large scale and with a low cost, to make the corresponding devices more competitive in the energy market. With the development of nanotechnologies, we are confident that these issues will be eventually addressed.

Bibliography

1. Wen, L.; Wang, Z.; Mi, Y.; Xu, R.; Yu, S. H.; Lei, Y., Designing heterogeneous 1D nanostructure arrays based on AAO templates for energy applications. *Small* **2015,** *11*, 3408.
2. Shafiee, S.; Topal, E., When will fossil fuel reserves be diminished? *Energy Policy* **2009,** *37*, 181.
3. Yang, Z.; Zhang, J.; Kintner-Meyer, M. C.; Lu, X.; Choi, D.; Lemmon, J. P.; Liu, J., Electrochemical energy storage for green grid. *Chem. Rev.* **2011,** *111*, 3577.
4. Walter, M. G.; Warren, E. L.; McKone, J. R.; Boettcher, S. W.; Mi, Q.; Santori, E. A.; Lewis, N. S., Solar water splitting cells. *Chem. Rev.* **2010,** *110*, 6446.
5. Energiewende, A., Current and future cost of photovoltaics–long-term scenarios for market development system prices and LCOE of utility-scale PV systems. Berlin, **2015**.
6. Zhao, H.; Zhou, M.; Wen, L.; Lei, Y., Template-directed construction of nanostructure arrays for highly-efficient energy storage and conversion. *Nano Energy* **2015,** *13*, 790.
7. Lei, Y.; Yang, S.; Wu, M.; Wilde, G., Surface patterning using templates: concept, properties and device applications. *Chem. Soc. Rev.* **2011,** *40*, 1247.
8. Long, J. W.; Dunn, B.; Rolison, D. R.; White, H. S., Three-dimensional battery architectures. *Chem. Rev.* **2004,** *104*, 4463.
9. Han, F.; Meng, G.; Zhou, F.; Song, L.; Li, X.; Hu, X.; Zhu, X.; Wu, B.; Wei, B., Dielectric capacitors with three-dimensional nanoscale interdigital electrodes for energy storage. *Sci. Adv.* **2015,** *1*, e1500605.
10. Chen, Y., Nanofabrication by electron beam lithography and its applications: A review. *Microelectron. Eng.* **2015,** *135*, 57.
11. Levinson, H. J., *Principles of lithography*. USA, 2005.
12. Okazaki, S., Resolution limits of optical lithography. *J. Vac. Sci. Technol. B Microelectron Nanom. Struct.* **1991,** *9*, 2829.
13. Okazaki, S., Lithographic technologies for future ULSI. *Appl. Surf. Sci.* **1993,** *70*, 603.
14. Wang, Y.; Du, Z.; Park, Y.; Chen, C.; Zhang, X.; Pan, L., Quasi-3D plasmonic coupling scheme for near-field optical lithography and imaging. *Opt. Lett.* **2015,** *40*, 3918.
15. Vieu, C.; Carcenac, F.; Pepin, A.; Chen, Y.; Mejias, M.; Lebib, A.; Manin-Ferlazzo, L.; Couraud, L.; Launois, H., Electron beam lithography: resolution limits and applications. *Appl. Surf. Sci.* **2000,** *164*, 111.
16. Chou, S. Y.; Krauss, P. R.; Renstrom, P. J., Imprint of sub-25 nm vias and trenches in polymers. *Appl. Phys. Lett.* **1995,** *67*, 3114.
17. Chou, S. Y.; Krauss, P. R.; Renstrom, P. J., Imprint lithography with 25-nanometer resolution. *Science* **1996,** *272*, 85.
18. Chou, S. Y.; Krauss, P. R.; Zhang, W.; Guo, L.; Zhuang, L., Sub-10 nm imprint lithography and applications. *J. Vac. Sci. Technol. B Microelectron. Nanom. Struct.* **1997,** *15*, 2897.
19. Sugawara, M., *Plasma etching: fundamentals and applications*. New York, **1998**.
20. Wang, Z.; Cao, D.; Xu, R.; Qu, S.; Wang, Z.; Lei, Y., Realizing ordered arrays of nanostructures: A versatile platform for converting and storing energy efficiently. *Nano Energy* **2016,** *19*, 328.
21. Bowden, N.; Terfort, A.; Carbeck, J.; Whitesides, G. M., Self-assembly of mesoscale objects into ordered two-dimensional arrays. *Science* **1997,** *276*, 233.
22. Brinker, C. J., Evaporation-induced self-assembly: functional nanostructures made easy. *MRS Bull.* **2004,** *29*, 631.
23. Boncheva, M.; Whitesides, G. M., Making things by self-assembly. *MRS Bull.* **2005,** *30*, 736.
24. Whitesides, G. M.; Grzybowski, B., Self-assembly at all scales. *Science* **2002,** *295*, 2418.

25. Glotzer, S.; Solomon, M.; Kotov, N. A., Self-assembly: From nanoscale to microscale colloids. *AIChE J.* **2004,** *50*, 2978.
26. Hosokawa, K.; Shimoyama, I.; Miura, H., Two-dimensional micro-self-assembly using the surface tension of water. *Sensors Actuators A Phys.* **1996,** *57*, 117.
27. Dungey, K. E., Kixium monolayers: A simple alternative to the bubble raft model for close-packed spheres. *J. Chem. Educ.* **2000,** *77*, 618.
28. Cui, T.; Hua, F.; Lvov, Y., Lithographic approach to pattern multiple nanoparticle thin films prepared by layer-by-layer self-assembly for microsystems. *Sensors Actuators A Phys.* **2004,** *114*, 501.
29. Velev, O. D., Self-assembly of unusual nanoparticle crystals. *Science* **2006,** *312*, 376.
30. Chen, D., Anti-reflection (AR) coatings made by sol–gel processes: a review. *Sol. Energy Mater. Sol. Cells* **2001,** *68*, 313.
31. Wang, Y.; Zhou, W., A review on inorganic nanostructure self-assembly. *J. Nanosci. Nanotechnol.* **2010,** *10*, 1563.
32. Lei, Y.; Cai, W. P.; Wilde, G., Highly ordered nanostructures with tunable size, shape and properties: A new way to surface nano-patterning using ultra-thin alumina masks. *Prog. Mater. Sci.* **2007,** *52*, 465.
33. Mikulskas, I.; Juodkazis, S.; Tomasiunas, R.; Dumas, J. G., Aluminum oxide photonic crystals grown by a new hybrid method. *Adv. Mater.* **2001,** *13*, 1574.
34. Zhan, Z. B.; Lei, Y., Sub-100-nm Nanoparticle Arrays with Perfect Ordering and Tunable and Uniform Dimensions Fabricated by Combining Nanoimprinting with Ultrathin Alumina Membrane Technique. *ACS Nano* **2014,** *8*, 3862.
35. Zhao, H.; Wang, C.; Vellacheri, R.; Zhou, M.; Xu, Y.; Fu, Q.; Wu, M.; Grote, F.; Lei, Y., Self-Supported Metallic Nanopore Arrays with Highly Oriented Nanoporous Structures as Ideally Nanostructured Electrodes for Supercapacitor Applications. *Adv. Mater.* **2014,** *26*, 7654.
36. Lei, Y.; Chim, W. K.; Zhang, Z. P.; Zhou, T. J.; Zhang, L. D.; Meng, G. W.; Phillipp, F., Ordered nanoporous nickel films and their magnetic properties. *Chem. Phys. Lett.* **2003,** *380*, 313.
37. Lei, Y.; Liang, C. H.; Wu, Y. C.; Zhang, L. D.; Mao, Y. Q., Preparation of highly ordered nanoporous Co membranes assembled by small quantum-sized Co particles. *J. Vac. Sci. Technol. B* **2001,** *19*, 1109.
38. Masuda, H.; Yasui, K.; Nishio, K., Fabrication of ordered arrays of multiple nanodots using anodic porous alumina as an evaporation mask. *Adv. Mater.* **2000,** *12*, 1031.
39. Fu, Q.; Zhan, Z. B.; Dou, J. X.; Zheng, X. Z.; Xu, R.; Wu, M. H.; Lei, Y., Highly Reproducible and Sensitive SERS Substrates with Ag Inter-Nanoparticle Gaps of 5 nm Fabricated by Ultrathin Aluminum Mask Technique. *ACS Appl. Mater. Interfaces* **2015,** *7*, 13322.
40. Lin, Q. F.; Leung, S. F.; Lu, L. F.; Chen, X. Y.; Chen, Z.; Tang, H. N.; Su, W. J.; Li, D. D.; Fan, Z. Y., Inverted Nanocone-Based Thin Film Photovoltaics with Omnidirectionally Enhanced Performance. *ACS Nano* **2014,** *8*, 6484.
41. Tsui, K. H.; Lin, Q.; Chou, H.; Zhang, Q.; Fu, H.; Qi, P.; Fan, Z., Low-Cost, Flexible, and Self-Cleaning 3D Nanocone Anti-Reflection Films for High-Efficiency Photovoltaics. *Adv. Mater.* **2014,** *26*, 2805.
42. Wang, C. L.; Wen, L. Y.; Kups, T.; Mi, Y.; Vellacheri, R.; Fang, Y. G.; Schaaf, P.; Zhao, H. P.; Lei, Y., Growth control of AgTCNQ nanowire arrays by using a template-assisted electro-deposition method. *J. Mater. Chem. C* **2013,** *1*, 8003.
43. Grote, F.; Kuhnel, R. S.; Balducci, A.; Lei, Y., Template assisted fabrication of free-standing MnO_2 nanotube and nanowire arrays and their application in supercapacitors. *Appl. Phys. Lett.* **2014,** *104*, 053904.

44. Al-Haddad, A.; Wang, Z. J.; Xu, R.; Qi, H. Y.; Vellacheri, R.; Kaiser, U.; Lei, Y., Dimensional Dependence of the Optical Absorption Band Edge of TiO_2 Nanotube Arrays beyond the Quantum Effect. *J. Phys. Chem. C* **2015,** *119*, 16331.
45. Tarish, S.; Wang, Z. J.; Al-Haddad, A.; Wang, C. L.; Ispas, A.; Romanus, H.; Schaaf, P.; Lei, Y., Synchronous Formation of ZnO/ZnS Core/Shell Nanotube Arrays with Removal of Template for Meliorating Photoelectronic Performance. *J. Phys. Chem. C* **2015,** *119*, 14461.
46. Lee, W.; Schwirn, K.; Steinhart, M.; Pippel, E.; Scholz, R.; Gosele, U., Structural engineering of nanoporous anodic aluminium oxide by pulse anodization of aluminium. *Nat. Nanotechnol.* **2008,** *3*, 234.
47. Lee, W.; Kim, J. C.; Gosele, U., Spontaneous Current Oscillations during Hard Anodization of Aluminum under Potentiostatic Conditions. *Adv. Funct.Mater.* **2010,** *20*, 21.
48. Mubeen, S.; Singh, N.; Lee, J.; Stucky, G. D.; Moskovits, M.; McFarland, E. W., Synthesis of Chemicals Using Solar Energy with Stable Photoelectrochemically Active Heterostructures. *Nano Lett.* **2013,** *13*, 2110.
49. Lee, W.; Park, S. J., Porous Anodic Aluminum Oxide: Anodization and Templated Synthesis of Functional Nanostructures. *Chem. Rev.* **2014,** *114*, 7487.
50. Masuda, H.; Fukuda, K., Ordered metal nanohole arrays made by a two-step replication of honeycomb structures of anodic alumina. *Science* **1995,** *268*, 1466.
51. Masuda, H.; Yamada, H.; Satoh, M.; Asoh, H.; Nakao, M.; Tamamura, T., Highly ordered nanochannel-array architecture in anodic alumina. *Appl. Phys. Lett.* **1997,** *71*, 2770.
52. Hebert, K. R.; Albu, S. P.; Paramasivam, I.; Schmuki, P., Morphological instability leading to formation of porous anodic oxide films. *Nat. Mater.* **2012,** *11*, 162.
53. Fujishima, A.; Honda, K., Electrochemical Photolysis of Water at a Semiconductor Electrode. *Nature* **1972,** *238*, 37.
54. Boettcher, S. W.; Spurgeon, J. M.; Putnam, M. C.; Warren, E. L.; Turner-Evans, D. B.; Kelzenberg, M. D.; Maiolo, J. R.; Atwater, H. A.; Lewis, N. S., Energy-conversion properties of vapor-liquid-solid–grown silicon wire-array photocathodes. *Science* **2010,** *327*, 185.
55. Hu, S.; Shaner, M. R.; Beardslee, J. A.; Lichterman, M.; Brunschwig, B. S.; Lewis, N. S., Amorphous TiO_2 coatings stabilize Si, GaAs, and GaP photoanodes for efficient water oxidation. *Science* **2014,** *344*, 1005.
56. Kim, H. J.; Lee, S. H.; Upadhye, A. A.; Ro, I.; Tejedor-Tejedor, M. I.; Anderson, M. A.; Kim, W. B.; Huber, G. W., Plasmon-Enhanced Photoelectrochemical Water Splitting with Size-Controllable Gold Nanodot Arrays. *ACS Nano* **2014,** *8*, 10756.
57. Lee, J.; Mubeen, S.; Ji, X. L.; Stucky, G. D.; Moskovits, M., Plasmonic Photoanodes for Solar Water Splitting with Visible Light. *Nano Lett.* **2012,** *12*, 5014.
58. Mubeen, S.; Lee, J.; Singh, N.; Kramer, S.; Stucky, G. D.; Moskovits, M., An autonomous photosynthetic device in which all charge carriers derive from surface plasmons. *Nat. Nanotechnol.* **2013,** *8*, 247.
59. Wang, X.; Liow, C.; Qi, D.; Zhu, B.; Leow, W. R.; Wang, H.; Xue, C.; Chen, X.; Li, S., Programmable Photo-Electrochemical Hydrogen Evolution Based on Multi-Segmented CdS-Au Nanorod Arrays. *Adv. Mater.* **2014,** *26*, 3506.
60. Zhang, C.; Shao, M.; Ning, F.; Xu, S.; Li, Z.; Wei, M.; Evans, D. G.; Duan, X., Au nanoparticles sensitized ZnO nanorod@ nanoplatelet core–shell arrays for enhanced photoelectrochemical water splitting. *Nano Energy* **2015,** *12*, 231.
61. Zhou, M.; Bao, J.; Xu, Y.; Zhang, J. J.; Xie, J. F.; Guan, M. L.; Wang, C. L.; Wen, L. Y.; Lei, Y.; Xie, Y., Photoelectrodes Based upon Mo: $BiVO_4$ Inverse Opals for Photoelectrochemical Water Splitting. *ACS Nano* **2014,** *8*, 7088.
62. Qiu, Y. C.; Leung, S. F.; Zhang, Q. P.; Hua, B.; Lin, Q. F.; Wei, Z. H.; Tsui, K. H.; Zhang, Y. G.; Yang, S. H.; Fan, Z. Y., Efficient Photoelectrochemical Water Splitting with Ultrathin films of Hematite on Three-Dimensional Nanophotonic Structures. *Nano Lett.* **2014,** *14*, 2123.

63. Li, J.; Qiu, Y.; Wei, Z.; Lin, Q.; Zhang, Q.; Yan, K.; Chen, H.; Xiao, S.; Fan, Z.; Yang, S., A three-dimensional hexagonal fluorine-doped tin oxide nanocone array: a superior light harvesting electrode for high performance photoelectrochemical water splitting. *Energy Environ. Sci.* **2014,** *7*, 3651.
64. Li, Y. B.; Zhang, L.; Torres-Pardo, A.; Gonzalez-Calbet, J. M.; Ma, Y. H.; Oleynikov, P.; Terasaki, O.; Asahina, S.; Shima, M.; Cha, D.; Zhao, L.; Takanabe, K.; Kubota, J.; Domen, K., Cobalt phosphate-modified barium-doped tantalum nitride nanorod photoanode with 1.5% solar energy conversion efficiency. *Nat. Commun.***2013,** *4*, 2566.
65. Li, J. T.; Cushing, S. K.; Zheng, P.; Meng, F. K.; Chu, D.; Wu, N. Q., Plasmon-induced photonic and energy-transfer enhancement of solar water splitting by a hematite nanorod array. *Nat. Commun.* **2013,** *4*, 2651
66. Warren, E. L.; McKone, J. R.; Atwater, H. A.; Gray, H. B.; Lewis, N. S., Hydrogen-evolution characteristics of Ni–Mo-coated, radial junction, n+ p-silicon microwire array photocathodes. *Energy Environ. Sci.* **2012,** *5*, 9653.
67. Jang, J. W.; Du, C.; Ye, Y. F.; Lin, Y. J.; Yao, X. H.; Thorne, J.; Liu, E.; McMahon, G.; Zhu, J. F.; Javey, A.; Guo, J. H.; Wang, D. W., Enabling unassisted solar water splitting by iron oxide and silicon. *Nat. Commun.* **2015,** *6*, 7447.
68. Hu, S.; Chi, C. Y.; Fountaine, K. T.; Yao, M. Q.; Atwater, H. A.; Dapkus, P. D.; Lewis, N. S.; Zhou, C. W., Optical, electrical, and solar energy-conversion properties of gallium arsenide nanowire-array photoanodes. *Energy Environ. Sci.* **2013,** *6*, 1879.
69. Huang, M.; Zhang, Y.; Li, F.; Zhang, L.; Ruoff, R. S.; Wen, Z.; Liu, Q., Self-assembly of mesoporous nanotubes assembled from interwoven ultrathin birnessite-type MnO2 nanosheets for asymmetric supercapacitors. *Sci. Rep.* **2014,** *4*, 3878.
70. Mayer, M. T.; Du, C.; Wang, D. W., Hematite/Si Nanowire Dual-Absorber System for Photoelectrochemical Water Splitting at Low Applied Potentials. *J. Am. Chem. Soc.* **2012,** *134*, 12406.
71. Hwang, Y. J.; Wu, C. H.; Hahn, C.; Jeong, H. E.; Yang, P. D., Si/InGaN Core/Shell Hierarchical Nanowire Arrays and their Photoelectrochemical Properties. *Nano Lett.* **2012,** *12*, 1678.
72. Moir, J.; Soheilnia, N.; O'Brien, P.; Jelle, A.; Grozea, C. M.; Faulkner, D.; Helander, M. G.; Ozin, G. A., Enhanced Hematite Water Electrolysis Using a 3D Antimony-Doped Tin Oxide Electrode. *ACS Nano* **2013,** *7*, 4261.
73. Zhang, K.; Shi, X.; Kim, J. K.; Lee, J. S.; Park, J. H., Inverse opal structured α-Fe 2 O 3 on graphene thin films: enhanced photo-assisted water splitting. *Nanoscale* **2013,** *5*, 1939.
74. Chen, X. Q.; Ye, J. H.; Ouyang, S. X.; Kako, T.; Li, Z. S.; Zou, Z. G., Enhanced Incident Photon-to-Electron Conversion Efficiency of Tungsten Trioxide Photoanodes Based on 3D-Photonic Crystal Design. *ACS Nano* **2011,** *5*, 4310.
75. Coridan, R. H.; Arpin, K. A.; Brunschwig, B. S.; Braun, P. V.; Lewis, N. S., Photoelectrochemical behavior of hierarchically structured Si/WO_3 core–shell tandem photoanodes. *Nano Lett.* **2014,** *14*, 2310.
76. Wen, L.; Mi, Y.; Wang, C.; Fang, Y.; Grote, F.; Zhao, H.; Zhou, M.; Lei, Y., Cost-effective Atomic Layer Deposition Synthesis of Pt Nanotube Arrays: Application for High Performance Supercapacitor. *Small* **2014,** *10*, 3162.
77. Mi, Y.; Wen, L.; Xu, R.; Wang, Z.; Cao, D.; Fang, Y.; Lei, Y., Constructing a AZO/TiO_2 core/shell nanocone array with uniformly dispersed Au NPs for enhancing photoelectrochemical water splitting. *Adv. Energy Mater.* **2016,** *6*, 1501496.
78. Li, P.; Liu, B.; Ni, Y.; Liew, K. K.; Sze, J.; Chen, S.; Shen, S., Large-Scale Nanophotonic Solar Selective Absorbers for High-Efficiency Solar Thermal Energy Conversion. *Adv. Mater.* **2015,** *27*, 4585.

79. Ni, G.; Miljkovic, N.; Ghasemi, H.; Huang, X.; Boriskina, S. V.; Lin, C.-T.; Wang, J.; Xu, Y.; Rahman, M. M.; Zhang, T., Volumetric solar heating of nanofluids for direct vapor generation. *Nano Energy* **2015,** *17*, 290.
80. Zou, Z. G.; Ye, J. H.; Sayama, K.; Arakawa, H., Direct splitting of water under visible light irradiation with an oxide semiconductor photocatalyst. *Nature* **2001,** *414*, 625.
81. Maeda, K.; Teramura, K.; Lu, D. L.; Takata, T.; Saito, N.; Inoue, Y.; Domen, K., Photocatalyst releasing hydrogen from water - Enhancing catalytic performance holds promise for hydrogen production by water splitting in sunlight. *Nature* **2006,** *440*, 295.
82. Zhang, Z. H.; Dua, R.; Zhang, L. B.; Zhu, H. B.; Zhang, H. N.; Wang, P., Carbon-Layer-Protected Cuprous Oxide Nanowire Arrays for Efficient Water Reduction. *ACS Nano* **2013,** *7*, 1709.
83. Wang, X. D.; Xie, J. L.; Li, C. M., Architecting smart "umbrella" Bi2S3/rGO-modified TiO2 nanorod array structures at the nanoscale for efficient photoelectrocatalysis under visible light. *J. Mater. Chem. A* **2015,** *3*, 1235.
84. Liu, Y.; Liang, L.; Xiao, C.; Hua, X.; Li, Z.; Pan, B.; Xie, Y., Promoting Photogenerated Holes Utilization in Pore-Rich WO_3 Ultrathin Nanosheets for Efficient Oxygen-Evolving Photoanode. *Adv. Energy Mater.* **2016,** *6*, 1600437.
85. Lei, F.; Zhang, L.; Sun, Y.; Liang, L.; Liu, K.; Xu, J.; Zhang, Q.; Pan, B.; Luo, Y.; Xie, Y., Atomic-Layer-Confined Doping for Atomic-Level Insights into Visible-Light Water Splitting. *Angew. Chem., Int. Ed.* **2015,** *54*, 9266.
86. Xie, J. L.; Guo, C. X.; Yang, P. P.; Wang, X. D.; Liu, D. Y.; Li, C. M., Bi-functional ferroelectric $BiFeO_3$ passivated $BiVO_4$ photoanode for efficient and stable solar water oxidation. *Nano Energy* **2017,** *31*, 28.
87. Hou, W. B.; Cronin, S. B., A Review of Surface Plasmon Resonance-Enhanced Photocatalysis. *Adv. Funct.Mater.* **2013,** *23*, 1612.
88. Li, Y.; Takata, T.; Cha, D.; Takanabe, K.; Minegishi, T.; Kubota, J.; Domen, K., Vertically Aligned Ta_3N_5 Nanorod Arrays for Solar-Driven Photoelectrochemical Water Splitting. *Adv. Mater.* **2013,** *25*, 125.
89. Maier, S. A., *Plasmonics: fundamentals and applications*. Springer Science & Business Media: 2007.
90. Linic, S.; Christopher, P.; Ingram, D. B., Plasmonic-metal nanostructures for efficient conversion of solar to chemical energy. *Nat. Mater.* **2011,** *10*, 911.
91. Guo, L. H.; Ferhan, A. R.; Chen, H. L.; Li, C. M.; Chen, G. N.; Hong, S.; Kim, D. H., Distance-Mediated Plasmonic Dimers for Reusable Colorimetric Switches: A Measurable Peak Shift of More than 60 nm. *Small* **2013,** *9*, 234.
92. Zhan, Z. B.; Grote, F.; Wang, Z. J.; Xu, R.; Lei, Y., Degenerating Plasmonic Modes to Enhance the Performance of Surface Plasmon Resonance for Application in Solar Energy Conversion. *Adv. Energy Mater.* **2015,** *5*, 1501654.
93. Li, Z. B.; Meng, G. W.; Huang, Q.; Hu, X. Y.; He, X.; Tang, H. B.; Wang, Z. W.; Li, F. D., Ag Nanoparticle-Grafted PAN-Nanohump Array Films with 3D High-Density Hot Spots as Flexible and Reliable SERS Substrates. *Small* **2015,** *11*, 5452.
94. Wang, Z. J.; Cao, D. W.; Wen, L. Y.; Xu, R.; Obergfell, M.; Mi, Y.; Zhan, Z. B.; Nasori, N.; Demsar, J.; Lei, Y., Manipulation of charge transfer and transport in plasmonic-ferroelectric hybrids for photoelectrochemical applications. *Nat. Commun.* **2016,** *7*, 10348.
95. Kakavelakis, G.; Vangelidis, I.; Heuer-Jungemann, A.; Kanaras, A. G.; Lidorikis, E.; Stratakis, E.; Kymakis, E., Plasmonic Backscattering Effect in High-Efficient Organic Photovoltaic Devices. *Adv. Energy Mater.* **2016,** *6*, 1501640.
96. Atwater, H. A.; Polman, A., Plasmonics for improved photovoltaic devices. *Nat. Mater.* **2010,** *9*, 865.

97. Chen, X.; Jia, B. H.; Saha, J. K.; Cai, B. Y.; Stokes, N.; Qiao, Q.; Wang, Y. Q.; Shi, Z. R.; Gu, M., Broadband Enhancement in Thin-Film Amorphous Silicon Solar Cells Enabled by Nucleated Silver Nanoparticles. *Nano Lett.* **2012,** *12*, 2187.
98. Solarska, R.; Bienkowski, K.; Zoladek, S.; Majcher, A.; Stefaniuk, T.; Kulesza, P. J.; Augustynski, J., Enhanced Water Splitting at Thin Film Tungsten Trioxide Photoanodes Bearing Plasmonic Gold-Polyoxometalate Particles. *Angew. Chem. Int. Edit.* **2014,** *53*, 14196.
99. Archana, P. S.; Pachauri, N.; Shan, Z. C.; Pan, S. L.; Gupta, A., Plasmonic Enhancement of Photoactivity by Gold Nanoparticles Embedded in Hematite Films. *J. Phys. Chem. C* **2015,** *119*, 15506.
100. Wang, X. T.; Liow, C.; Qi, D. P.; Zhu, B. W.; Leow, W. R.; Wang, H.; Xue, C.; Chen, X. D.; Li, S. Z., Programmable Photo-Electrochemical Hydrogen Evolution Based on Multi-Segmented CdS-Au Nanorod Arrays. *Adv. Mater.* **2014,** *26*, 3506.
101. Jeong, S.; McGehee, M. D.; Cui, Y., All-back-contact ultra-thin silicon nanocone solar cells with 13.7% power conversion efficiency. *Nat. Commun.* **2013,** *4*, 2950.
102. Kargar, A.; Sun, K.; Jing, Y.; Choi, C.; Jeong, H.; Jung, G. Y.; Jin, S.; Wang, D. L., 3D Branched Nanowire Photoelectrochemical Electrodes for Efficient Solar Water Splitting. *ACS Nano* **2013,** *7*, 9407.
103. Li, G. J.; Li, H.; Ho, J. Y. L.; Wong, M.; Kwok, H. S., Nanopyramid Structure for Ultrathin c-Si Tandem Solar Cells. *Nano Lett.* **2014,** *14*, 2563.
104. Li, J. K.; Qiu, Y. C.; Wei, Z. H.; Lin, Q. F.; Zhang, Q. P.; Yan, K. Y.; Chen, H. N.; Xiao, S.; Fan, Z. Y.; Yang, S. H., A three-dimensional hexagonal fluorine-doped tin oxide nanocone array: a superior light harvesting electrode for high performance photoelectrochemical water splitting. *Energy Environ. Sci.* **2014,** *7*, 3651.
105. Xie, J. L.; Guo, C. X.; Li, C. M., Construction of one-dimensional nanostructures on graphene for efficient energy conversion and storage. *Energy Environ. Sci.* **2014,** *7*, 2559.
106. Wen, L. Y.; Wang, Z. J.; Mi, Y.; Xu, R.; Yu, S. H.; Lei, Y., Designing Heterogeneous 1D Nanostructure Arrays Based on AAO Templates for Energy Applications. *Small* **2015,** *11*, 3408.
107. Wang, Z. J.; Cao, D. W.; Xu, R.; Qu, S. C.; Wang, Z. G.; Lei, Y., Realizing ordered arrays of nanostructures: A versatile platform for converting and storing energy efficiently. *Nano Energy* **2016,** *19*, 328.
108. Gao, H. W.; Liu, C.; Jeong, H. E.; Yang, P. D., Plasmon-Enhanced Photocatalytic Activity of Iron Oxide on Gold Nanopillars. *ACS Nano* **2012,** *6*, 234.
109. Sherry, L. J.; Jin, R. C.; Mirkin, C. A.; Schatz, G. C.; Van Duyne, R. P., Localized surface plasmon resonance spectroscopy of single silver triangular nanoprisms. *Nano Lett.* **2006,** *6*, 2060.
110. Mayer, K. M.; Lee, S.; Liao, H.; Rostro, B. C.; Fuentes, A.; Scully, P. T.; Nehl, C. L.; Hafner, J. H., A label-free immunoassay based upon localized surface plasmon resonance of gold nanorods. *ACS Nano* **2008,** *2*, 687.
111. Xu, R.; Wang, X. D.; Song, L.; Liu, W.; Ji, A.; Yang, F. H.; Li, J. M., Influence of the light trapping induced by surface plasmons and antireflection film in crystalline silicon solar cells. *Opt. Express* **2012,** *20*, 5061.
112. Wen, L. Y.; Xu, R.; Mi, Y.; Lei, Y., Multiple nanostructures based on anodized aluminium oxide templates. *Nat. Nanotechnol.* **2017,** *12*, 244.
113. Li, H. Q.; Wang, X.; Xu, J. Q.; Zhang, Q.; Bando, Y.; Golberg, D.; Ma, Y.; Zhai, T. Y., One-Dimensional CdS Nanostructures: A Promising Candidate for Optoelectronics. *Adv. Mater.* **2013,** *25*, 3017.
114. Barnes, W. L.; Murray, W. A.; Dintinger, J.; Devaux, E.; Ebbesen, T. W., Surface plasmon polaritons and their role in the enhanced transmission of light through periodic arrays of subwavelength holes in a metal film. *Phys. Rev. Lett.* **2004,** *92*, 107401.

115. Kelly, K. L.; Coronado, E.; Zhao, L. L.; Schatz, G. C., The optical properties of metal nanoparticles: The influence of size, shape, and dielectric environment. *J. Phys. Chem. B* **2003,** *107*, 668.
116. Miller, M. M.; Lazarides, A. A., Sensitivity of metal nanoparticle surface plasmon resonance to the dielectric environment. *J. Phys. Chem. B* **2005,** *109*, 21556.
117. Damos, F. S.; Luz, R. C. S.; Kubota, L. T., Determination of thickness, dielectric constant of thiol films, and kinetics of adsorption using surface plasmon resonance. *Langmuir* **2005,** *21*, 602.
118. Chien, F. C.; Chen, S. J., Direct determination of the refractive index and thickness of a biolayer based on coupled waveguide-surface plasmon resonance mode. *Opt. Lett.* **2006,** *31*, 187.
119. Zhang, Y. A.; Stokes, N.; Jia, B.; Fan, S. H.; Gu, M., Towards ultra-thin plasmonic silicon wafer solar cells with minimized efficiency loss. *Sci. Rep.* **2014,** *4*, 4939.
120. Yu, R.; Ching, K. L.; Lin, Q. F.; Leung, S. F.; Arcrossito, D.; Fan, Z. Y., Strong Light Absorption of Self-Organized 3-D Nanospike Arrays for Photovoltaic Applications. *ACS Nano* **2011,** *5* (11), 9291-9298.
121. Costi, R.; Saunders, A. E.; Banin, U., Colloidal hybrid nanostructures: a new type of functional materials. *Angew. Chem. Int. Ed.* **2010,** *49*, 4878.
122. Surnev, S.; Fortunelli, A.; Netzer, F. P., Structure–property relationship and chemical aspects of oxide–metal hybrid nanostructures. *Chem. Rev.* **2012,** *113*, 4314.
123. Xu, C.; Wang, B.; Sun, S., Dumbbell-like Au− Fe_3O_4 nanoparticles for target-specific platin delivery. *J. Am. Chem. Soc.* **2009,** *131*, 4216.
124. Buck, M. R.; Bondi, J. F.; Schaak, R. E., A total-synthesis framework for the construction of high-order colloidal hybrid nanoparticles. *Nat. Chem.* **2012,** *4*, 37.
125. Carbone, L.; Cozzoli, P. D., Colloidal heterostructured nanocrystals: Synthesis and growth mechanisms. *Nano Today* **2010,** *5*, 449.
126. Cozzoli, P. D.; Pellegrino, T.; Manna, L., Synthesis, properties and perspectives of hybrid nanocrystal structures. *Chem. Soc. Rev.* **2006,** *35*, 1195.
127. Mokari, T.; Rothenberg, E.; Popov, I.; Costi, R.; Banin, U., Selective growth of metal tips onto semiconductor quantum rods and tetrapods. *Science* **2004,** *304*, 1787.
128. Liang, S.; Liu, X.-L.; Yang, Y.-Z.; Wang, Y.-L.; Wang, J.-H.; Yang, Z.-J.; Wang, L.-B.; Jia, S.-F.; Yu, X.-F.; Zhou, L., Symmetric and asymmetric Au–AgCdSe hybrid nanorods. *Nano Lett.* **2012,** *12*, 5281.
129. Hong, J. W.; Wi, D. H.; Lee, S.-U.; Han, S. W., Metal–Semiconductor Heteronanocrystals with Desired Configurations for Plasmonic Photocatalysis. *J. Am. Chem. Soc*. **2016,** *138*, 15766.
130. Seh, Z. W.; Liu, S.; Low, M.; Zhang, S. Y.; Liu, Z.; Mlayah, A.; Han, M. Y., Janus Au-TiO2 Photocatalysts with Strong Localization of Plasmonic Near-Fields for Efficient Visible-Light Hydrogen Generation. *Adv. Mater*. **2012,** *24*, 2310.
131. Kelly, K. L.; Coronado, E.; Zhao, L. L.; Schatz, G. C., The optical properties of metal nanoparticles: the influence of size, shape, and dielectric environment. *J. Phys. Chem. B* **2003**, *107*, 668.
132. Atwater, H. A.; Polman, A., Plasmonics for improved photovoltaic devices. *Nat. Mater*. **2010,** *9*, 205.
133. Qian, K.; Sweeny, B. C.; Johnston-Peck, A. C.; Niu, W.; Graham, J. O.; DuChene, J. S.; Qiu, J.; Wang, Y.-C.; Engelhard, M. H.; Su, D., Surface plasmon-driven water reduction: gold nanoparticle size matters. *J. Am. Chem. Soc.* **2014,** *136*, 9842.
134. Zhang, X.; Liu, Y.; Lee, S.-T.; Yang, S.; Kang, Z., Coupling surface plasmon resonance of gold nanoparticles with slow-photon-effect of TiO_2 photonic crystals for synergistically enhanced photoelectrochemical water splitting. *Energy Environ. Sci.* **2014,** *7*, 1409.

135. Zhang, J.; Jin, X.; Morales-Guzman, P. I.; Yu, X.; Liu, H.; Zhang, H.; Razzari, L.; Claverie, J. P., Engineering the absorption and field enhancement properties of Au–TiO_2 nanohybrids via whispering gallery mode resonances for photocatalytic water splitting. *ACS Nano* **2016,** *10*, 4496.
136. Dotan, H.; Kfir, O.; Sharlin, E.; Blank, O.; Gross, M.; Dumchin, I.; Ankonina, G.; Rothschild, A., Resonant light trapping in ultrathin films for water splitting. *Nat. Mater.* **2013,** *12*, 158.
137. Jiang, R.; Li, B.; Fang, C.; Wang, J., Metal/Semiconductor Hybrid Nanostructures for Plasmon-Enhanced Applications. *Adv. Mater.* **2014,** *26*, 5274.
138. Zhao, Q.; Ji, M.; Qian, H.; Dai, B.; Weng, L.; Gui, J.; Zhang, J.; Ouyang, M.; Zhu, H., Controlling structural symmetry of a hybrid nanostructure and its effect on efficient photocatalytic hydrogen evolution. *Adv. Mater.* **2014,** *26*, 1387.
139. Weng, L.; Zhang, H.; Govorov, A. O.; Ouyang, M., Hierarchical synthesis of non-centrosymmetric hybrid nanostructures and enabled plasmon-driven photocatalysis. *Nat. Commun.* **2014,** *5*, 4792.
140. Huang, Z.; Liu, Y.; Zhang, Q.; Chang, X.; Li, A.; Deng, L.; Yi, C.; Yang, Y.; Khashab, N. M.; Gong, J., Collapsed polymer-directed synthesis of multicomponent coaxial-like nanostructures. *Nat. Commun.* **2016,** *7*, 12147.
141. Donega, C. d. M., Synthesis and properties of colloidal heteronanocrystals. *Chem. Soc. Rev.* **2011,** *40*, 1512.
142. Hurst, S. J.; Payne, E. K.; Qin, L.; Mirkin, C. A., Multisegmented one-dimensional nanorods prepared by hard-template synthetic methods. *Angew. Chem. Int. Ed.* **2006,** *45*, 2672.
143. Walther, A.; Müller, A. H., Janus particles: synthesis, self-assembly, physical properties, and applications. *Chem. Rev.* **2013,** *113*, 5194.
144. Hao, Q.; Pang, J.; Zhang, Y.; Wang, J.; Ma, L.; Schmidt, O. G., Boosting the Photoluminescence of Monolayer MoS2 on High-Density Nanodimer Arrays with Sub-10 nm Gap. *Adv. Opt. Mater.* **2018**, *6*, 1700984.
145. Hao, Q.; Huang, H.; Fan, X.; Yin, Y.; Wang, J.; Li, W.; Qiu, T.; Ma, L.; Chu, P. K.; Schmidt, O. G., Controlled Patterning of Plasmonic Dimers by Using an Ultrathin Nanoporous Alumina Membrane as a Shadow Mask. *Acs. Appl. Mater. Inter.* **2017,** *9*, 36199.
146. Wen, L.; Xu, R.; Mi, Y.; Lei, Y., Multiple nanostructures based on anodized aluminium oxide templates. *Nat. Nanotechnol.* **2017,** *12*, 244.
147. Leung, S. F.; Gu, L. L.; Zhang, Q. P.; Tsui, K. H.; Shieh, J. M.; Shen, C. H.; Hsiao, T. H.; Hsu, C. H.; Lu, L. F.; Li, D. D.; Lin, Q. F.; Fan, Z. Y., Roll-to-roll fabrication of large scale and regular arrays of three-dimensional nanospikes for high efficiency and flexible photovoltaics. *Sci. Rep.* **2014**, *4*, 4243.
148. Yang, J.; Wang, D.; Han, H.; Li, C., Roles of cocatalysts in photocatalysis and photoelectrocatalysis. *Acc. Chem. Res.* **2013,** *46*, 1900.
149. Wang, G.; Wang, H.; Ling, Y.; Tang, Y.; Yang, X.; Fitzmorris, R. C.; Wang, C.; Zhang, J. Z.; Li, Y., Hydrogen-treated TiO_2 nanowire arrays for photoelectrochemical water splitting. *Nano Lett.* **2011,** *11*, 3026.
150. Park, J. H.; Kim, S.; Bard, A. J., Novel carbon-doped TiO_2 nanotube arrays with high aspect ratios for efficient solar water splitting. *Nano Lett.* **2006,** *6*, 24.
151. Zhang, Z.; Zhang, L.; Hedhili, M. N.; Zhang, H.; Wang, P., Plasmonic gold nanocrystals coupled with photonic crystal seamlessly on TiO_2 nanotube photoelectrodes for efficient visible light photoelectrochemical water splitting. *Nano Lett.* **2012,** *13*, 14.
152. Mi, Y.; Wen, L. Y.; Xu, R.; Wang, Z. J.; Cao, D. W.; Fang, Y. G.; Lei, Y., Constructing a AZO/TiO_2 Core/Shell Nanocone Array with Uniformly Dispersed Au NPs for Enhancing Photoelectrochemical Water Splitting. *Adv. Energy Mater.* **2016,** *6*, 1501496.
153. Pu, Y.-C.; Wang, G.; Chang, K.-D.; Ling, Y.; Lin, Y.-K.; Fitzmorris, B. C.; Liu, C.-M.; Lu, X.; Tong, Y.; Zhang, J. Z., Au nanostructure-decorated TiO_2 nanowires exhibiting

photoactivity across entire UV-visible region for photoelectrochemical water splitting. *Nano Lett.* **2013,** *13*, 3817.
154. Xu, R.; Wen, L.; Wang, Z.; Zhao, H.; Xu, S.; Mi, Y.; Xu, Y.; Sommerfeld, M.; Fang, Y.; Lei, Y., Three-dimensional plasmonic nanostructure design for boosting photoelectrochemical activity. *ACS Nano* **2017,** *11*, 7382.
155. Wang, Z.; Cao, D.; Wen, L.; Xu, R.; Obergfell, M.; Mi, Y.; Zhan, Z.; Nasori, N.; Demsar, J.; Lei, Y., Manipulation of charge transfer and transport in plasmonic-ferroelectric hybrids for photoelectrochemical applications. *Nat. Commun.* **2016,** *7*, 10348.
156. Costi, R.; Saunders, A. E.; Elmalem, E.; Salant, A.; Banin, U., Visible light-induced charge retention and photocatalysis with hybrid CdSe− Au nanodumbbells. *Nano Lett.* **2008,** *8*, 637.
157. Wu, B.; Liu, D.; Mubeen, S.; Chuong, T. T.; Moskovits, M.; Stucky, G. D., Anisotropic growth of TiO2 onto gold nanorods for plasmon-enhanced hydrogen production from water reduction. *J. Am. Chem. Soc* **2016,** *138*, 1114.
158. Tafalla, D.; Salvador, P.; Benito, R., Kinetic Approach to the Photocurrent Transients in Water Photoelectrolysis at n-TiO_2 Electrodes II. Analysis of the Photocurrent-Time Dependence. *J. Electrochem. Soc.* **1990,** *137*, 1810.
159. Li, J.; Cushing, S. K.; Zheng, P.; Meng, F.; Chu, D.; Wu, N., Plasmon-induced photonic and energy-transfer enhancement of solar water splitting by a hematite nanorod array. *Nat. Commun.* **2013,** *4*, 2651.
160. Meng, F.; Li, J.; Cushing, S. K.; Bright, J.; Zhi, M.; Rowley, J. D.; Hong, Z.; Manivannan, A.; Bristow, A. D.; Wu, N., Photocatalytic water oxidation by hematite/reduced graphene oxide composites. *Acs Catal.* **2013,** *3*, 746.
161. Wang, S.; Gao, Y.; Miao, S.; Liu, T.; Mu, L.; Li, R.; Fan, F.; Li, C., Positioning the Water Oxidation Reaction Sites in Plasmonic Photocatalysts. *J. Am. Chem. Soc.* **2017,** *139*, 11771.
162. Qin, L. D.; Park, S.; Huang, L.; Mirkin, C. A., On-wire lithography. *Science* **2005,** *309*, 113.
163. Ozel, T.; Bourret, G. R.; Mirkin, C. A., Coaxial lithography. *Nat. Nanotechnol.* **2015,** *10*, 319.
164. Benson, O., Assembly of hybrid photonic architectures from nanophotonic constituents. *Nature* **2011,** *480*, 193.
165. Polman, A.; Atwater, H. A., Photonic design principles for ultrahigh-efficiency photovoltaics. *Nat. Mater.* **2012,** *11*, 174.
166. Nemoto, K.; Trupke, M.; Devitt, S. J.; Stephens, A. M.; Scharfenberger, B.; Buczak, K.; Nöbauer, T.; Everitt, M. S.; Schmiedmayer, J.; Munro, W. J., Photonic architecture for scalable quantum information processing in diamond. *Phys. Rev. X* **2014**, *4*, 031022.
167. Soukoulis, C. M., Photonic crystals and light localization in the 21st century. Dordrecht, 2012.
168. Wang, K. X.; Yu, Z.; Liu, V.; Raman, A.; Cui, Y.; Fan, S., Light trapping in photonic crystals. *Energy Environ. Sci.* **2014,** *7*, 2725.
169. Chutinan, A.; John, S., Light trapping and absorption optimization in certain thin-film photonic crystal architectures. *Phys. Rev. A* **2008,** *78*, 023825.
170. Callahan, D. M.; Munday, J. N.; Atwater, H. A., Solar Cell Light Trapping beyond the Ray Optic Limit. *Nano Lett.* **2012,** *12*, 214.
171. John, S., Why trap light? *Nat.Mater.* **2012,** *11*, 997.
172. Neff, C. W.; Summers, C. J., A photonic crystal superlattice based on triangular lattice. *Opt. Express* **2005,** *13*, 3166.
173. Gaillot, D.; Graugnard, E.; Blair, J.; Summers, C., Dispersion control in two-dimensional superlattice photonic crystal slab waveguides by atomic layer deposition. *Appl. Phys. Lett.* **2007,** *91*, 181123.

174. Neff, C. W.; Yamashita, T.; Summers, C. J., Observation of Brillouin zone folding in photonic crystal slab waveguides possessing a superlattice pattern. *Appl.Phys. Lett.* **2007,** *90*, 021102
175. Tanaka, Y.; Kawamoto, Y.; Fujita, M.; Noda, S., Enhancement of broadband optical absorption in photovoltaic devices by band-edge effect of photonic crystals. *Opt. Express* **2013,** *21*, 20111.
176. Callahan, D. M.; Horowitz, K. A. W.; Atwater, H. A., Light trapping in ultrathin silicon photonic crystal superlattices with randomly-textured dielectric incouplers. *Opt. Express* **2013,** *21*, 30315.
177. Rinnerbauer, V.; Shen, Y. C.; Joannopoulos, J. D.; Soljacic, M.; Schaffler, F.; Celanovic, I., Superlattice photonic crystal as broadband solar absorber for high temperature operation. *Opt. Express* **2014,** *22*, A1895.
178. Gaillot, D. P.; Graugnard, E.; Blair, J.; Summers, C. J., Dispersion control in two-dimensional superlattice photonic crystal slab waveguides by atomic layer deposition. *Appl. Phys. Lett.* **2007,** *91*, 181123.
179. Near, R.; Tabor, C.; Duan, J.; Pachter, R.; El-Sayed, M., Pronounced effects of anisotropy on plasmonic properties of nanorings fabricated by electron beam lithography. *Nano Lett.* **2012,** *12*, 2158.
180. Rinnerbauer, V.; Lausecker, E.; Schäffler, F.; Reininger, P.; Strasser, G.; Geil, R.; Joannopoulos, J.; Soljačić, M.; Celanovic, I., Nanoimprinted superlattice metallic photonic crystal as ultraselective solar absorber. *Optica* **2015,** *2*, 743.
181. Wu, M.; Wen, L.; Lei, Y.; Ostendorp, S.; Chen, K.; Wilde, G., Ultrathin Alumina Membranes for Surface Nanopatterning in Fabricating Quantum-Sized Nanodots. *Small* **2010,** *6*, 695.
182. Zhan, Z.; Lei, Y., Sub-100-nm nanoparticle arrays with perfect ordering and tunable and uniform dimensions fabricated by combining nanoimprinting with ultrathin alumina membrane technique. *ACS Nano* **2014,** *8*, 3862.
183. Yu, Z.; Raman, A.; Fan, S., Fundamental limit of nanophotonic light trapping in solar cells. *Proc. Natl. Acad. Sci. USA* **2010,** *107*, 17491.
184. Joannopoulos, J. D.; Johnson, S. G.; Winn, J. N.; Meade, R. D., *Photonic crystals: molding the flow of light*. Princeton, 2011.
185. Hasan, S. B.; Mosk, A. P.; Vos, W. L.; Lagendijk, A., Finite-size Scaling of the Density of States in Photonic Band Gap Crystals. *Phys. Rev. Lett.* **2018,** *120*, 237402.
186. Maruyama, S.; Kashiwa, T.; Yugami, H.; Esashi, M., Thermal radiation from two-dimensionally confined modes in microcavities. *Appl. Phys. Lett.* **2001,** *79*, 1393.
187. Zhan, Z.; Xu, R.; Mi, Y.; Zhao, H.; Lei, Y., Highly controllable surface plasmon resonance property by heights of ordered nanoparticle arrays fabricated via a nonlithographic route. *ACS Nano* **2015,** *9*, 4583.
188. Grunin, A.; Zhdanov, A.; Ezhov, A.; Ganshina, E.; Fedyanin, A., Surface-plasmon-induced enhancement of magneto-optical Kerr effect in all-nickel subwavelength nanogratings. *Appl. Phys. Lett.* **2010,** *97*, 261908.
189. Chou, J. B.; Yeng, Y. X.; Lee, Y. E.; Lenert, A.; Rinnerbauer, V.; Celanovic, I.; Soljačić, M.; Fang, N. X.; Wang, E. N.; Kim, S. G., Enabling ideal selective solar absorption with 2D metallic dielectric photonic crystals. *Adv. Mater.* **2014,** *26*, 8041.
190. Radko, I.; Bozhevolnyi, S. I.; Brucoli, G.; Martín-Moreno, L.; García-Vidal, F.; Boltasseva, A., Efficient unidirectional ridge excitation of surface plasmons. *Opt. Express* **2009,** *17*, 7228.
191. Echtermeyer, T.; Milana, S.; Sassi, U.; Eiden, A.; Wu, M.; Lidorikis, E.; Ferrari, A., Surface plasmon polariton graphene photodetectors. *Nano Lett.* **2015,** *16*, 8.
192. Bermel, P.; Lee, J.; Joannopoulos, J. D.; Celanovic, I.; Soljacie, M., Selective solar absorbers. *Annu. Rev. Heat Transfer* **2012,** *15*, 231.

193. Tian, Y.; Zhao, C.-Y., A review of solar collectors and thermal energy storage in solar thermal applications. *Appl. Energ.* **2013,** *104*, 538.
194. Duffie, J. A.; Beckman, W. A., *Solar engineering of thermal processes*. New York, 2013.

Extended work

In addition to the achievements shown in this dissertation, I also cooperated with my colleagues in many research fields such as multi-pore AAO template, PEC, solar cell, SERS, and gas sensor. The abstracts and the table of content figures of the respective articless are demonstrated in this proceeding section to highlight the as-obtained academic results.

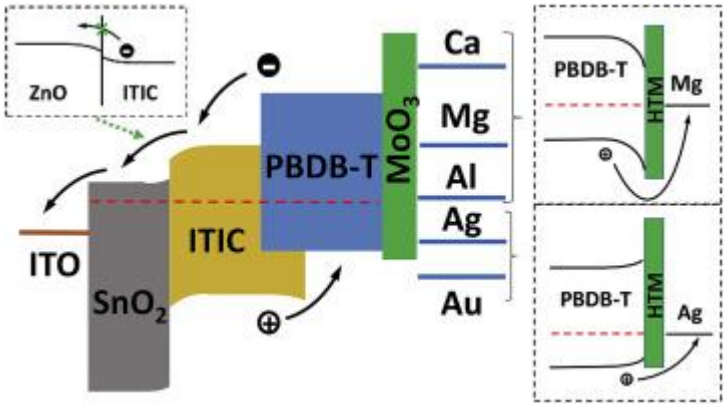

1. **Collection optimization of photo-generated charge carriers for efficient organic solar cells** (**J. Power Sources 2019, 412, 465-471**)

Collection of photo-generated charge carriers is of significance in organic photovoltaic devices. Herein, we focus on systematically exploring the effective methods to improve the charge collection efficiency in organic solar cells based on PBDB-T: ITIC. In the active layer, we observe that the energy level bending at the interface of acceptor/donor is influential to the recombination of charge carriers. For extracting electrons efficiently, we propose that using SnO_2 instead of ZnO as the electron conducting layer is advantageous in improving short-circuit current (Jsc), power conversion efficiency (PCE), and particularly stability. To unveil the dynamics of hole collection, we use different metals as the anode and find out that enlarging the work function of the anode close to the highest occupied molecular orbital (HOMO) of the donor is beneficial for enhancing the open-circuit voltage (Voc), Jsc, fill factor (FF) and thus PCE. The optimized device delivers a PCE of 10.77%. Insights on how to efficiently extract photo-generated charge carriers are elaborated systematically.

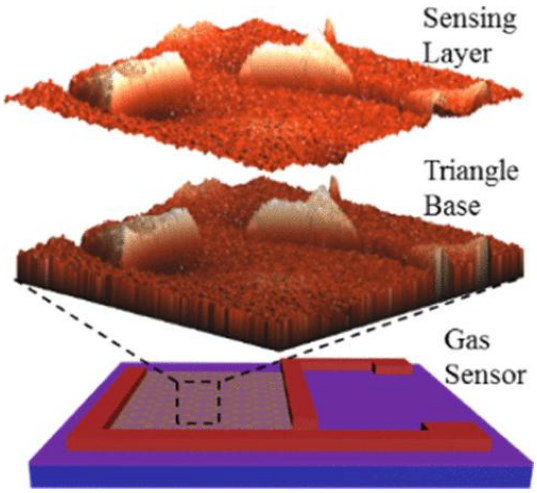

2. **Sensitive Gas-Sensing by Creating Adsorption Active Sites: Coating an SnO_2 Layer on Triangle Arrays (ACS Appl. Mater. Interfaces 2018, 10, 29092-29099)** It is a widely used strategy to enhance gas sensor sensitivity by improving its surface area, but this process, including bonding the sensing block into a device substrate, needs complex manipulations. This work shows a concept of creating adsorption active sites, in which an SnO_2 layer (6.85 nm thin) is directly coated on a triangle array substrate to be of an ensemble of triangular convex adsorption active sites (TCAASs). The resultant SnO2 gas sensors, with TCAAS periods ranging from 289 to 1154 nm, exhibit an adsorption-active-site-dependent sensitivity and present a low detection limit of around 6 ppm ethanol gas at room temperature. By characterizations of Kelvin force microscopy, a large surface potential variation exists on these adsorption active sites after introducing ethanol gas, distinctly showing a local adsorption enhancement. These results confirm that the creation of adsorption active sites can efficiently increase surface adsorption of a sensor to realize its sensitive gas-sensing.

3. **Carrier mobility-dominated gas sensing: a room-temperature gas-sensing mode for SnO_2 nanorod array sensors (ACS Appl. Mater. Interfaces 2018, 10, 13895-13902)**

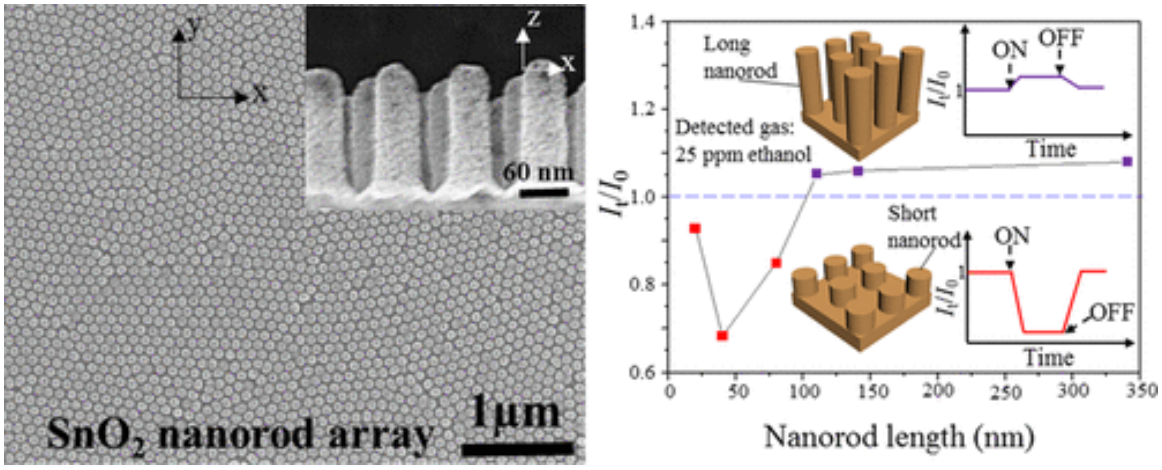

Adsorption-induced change of carrier density is presently dominating inorganic semiconductor gas sensing, which is usually operated at a high temperature. Besides carrier density, other carrier characteristics might also play a critical role in gas sensing. Here, we show that carrier mobility can be an efficient parameter to dominate gas sensing, by which room-temperature gas sensing of inorganic semiconductors is realized via a carrier mobility-dominated gas-sensing (CMDGS) mode. To demonstrate CMDGS, we design and prepare a gas sensor based on a regular array of SnO_2 nanorods on a bottom film. It is found that the key for determining the gas-sensing mode is adjusting the length of the arrayed nanorods. With the change in the nanorod length from 340 to 40 nm, the gas-sensing behavior changes from the conventional carrier-density mode to a complete carrier-mobility mode. Moreover, compared to the carrier density-dominating gas sensing, the proposed CMDGS mode enhances the sensor sensitivity. CMDGS proves to be an emerging gas-sensing mode for designing inorganic semiconductor gas sensors with high performances at room temperature.

4. Highly efficient solar cells based on Cl incorporated tri-cation perovskite materials (J. Mater. Chem. A 2018, 6, 13725-13734)

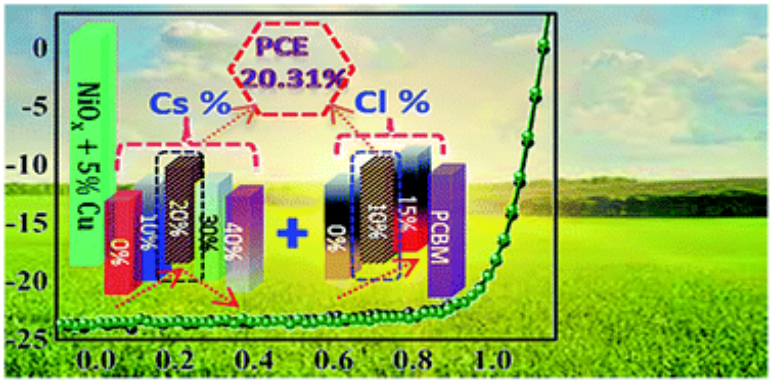

Though mixed cation hybrid organic–inorganic perovskite materials are of promise due to the high efficiency and long-term stability of the corresponding devices, a fundamental understanding on the function of the mixed cation system is still unclear. Herein, we systematically investigate the roles of the Cs cation and Cl anion in inverted structure perovskite solar cells based on $Cs_xFA_{0.2}MA_{0.8-x}Pb(I_{1-y}Cl_y)_3$. For the role of Cs, we observe that an appropriate amount of Cs in the film could improve the crystal quality of the film and optimize the energy band alignment of the device, thus reducing non-radiative recombination and promoting the charge transport efficiently. The presence of Cl with a suitable concentration also possesses these functions. More importantly, the two limitations for the application of the devices, hysteresis and performance instability, could also be addressed to some extent. Thus a high power conversion efficiency of 20.31% has been realized and a universal method for constructing highly-efficient perovskite solar cells has been provided.

5. MOCVD Compatible Atomic Layer Deposition Process of Al_2O_3 on SiC and Graphene/SiC Heterostructures (Materials Science Forum 2018, 924, 506-510)

Aluminium oxide was deposited on silicon, silicon carbide and epitaxial graphene grown on silicon carbide by atomic layer deposition using a standard MOCVD equipment. The morphology and the electrical properties of the aluminium oxide layers on both substrates were determined and compared to aluminium oxide layers deposited with a standard atomic layer deposition equipment. The high-k material fabricated with the developed MOCVD process show comparable or better properties compared to the standard atomic layer deposition process.

6. Self-Supported Bi_2MoO_6 Nanowall for Photoelectrochemical Water Splitting (ACS Appl. Mater. Interfaces 2017, 9, 23647-23653)

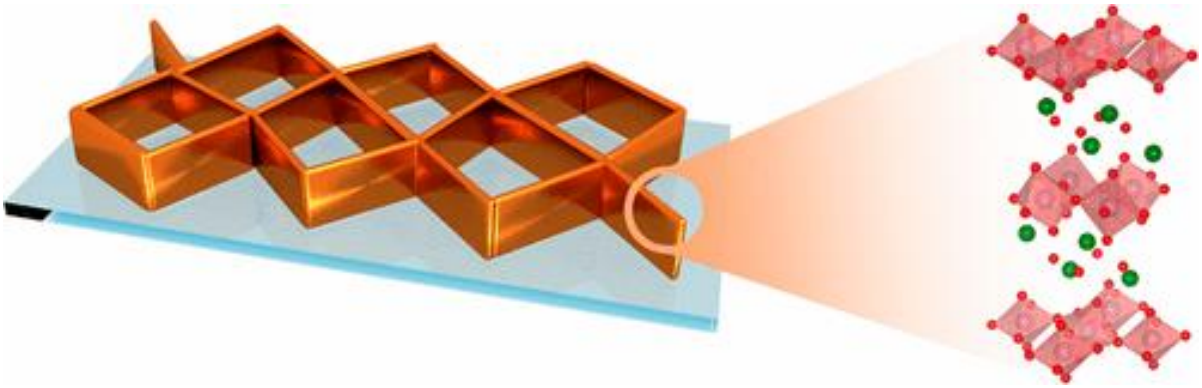

The nanowall has been regarded as a promising architecture for highly efficient photoelectrochemical (PEC) water splitting due to various advantages, such as open geometry, highly reactive facets, independent contact with current collector, and so forth. Here, a vertically aligned Bi2MoO6 nanosheet array, which is also called a nanowall, is first achieved directly on the ITO glass by a facile solvothermal approach. The structural features not only offer multiple superiorities for PEC processes, but also provide the bridge for in-depth insights of intrinsic features of Bi_2MoO_6 photoanodes. A quantitative analysis of the electrochemical process declares that the utilization of photogenerated charges in the Bi_2MoO_6 nanowall has been optimized, but the main obstacle comes from the severe bulk recombination and low efficiencies of charge separation. This evaluation both enriches the visual assessment methods and directs clear guidance for future improvement, which could serve as a beacon for well-directed and economic photoelectrode amelioration, to shorten the road toward ideal photoelectrodes.

7. Multiple nanostructures based on anodized aluminium oxide templates (Nat. Nanotechnol. 2017, 12, 244–250)

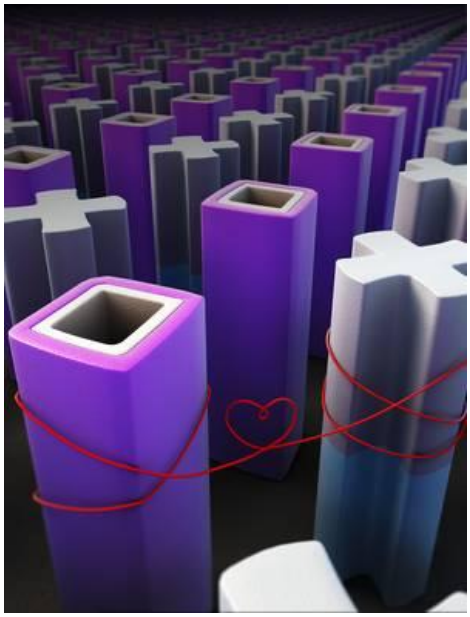

Several physico-chemical effects and properties in the solid state involve nanoscale interactions between adjacent materials and morphologies. Arrays of binary nanostructures can generate intimate interactions between different sub-components, but fabricating binary nanostructures is challenging. Here, we propose a concept to achieve diverse binary nanostructure arrays with high degrees of controllability for each of the sub-components, including material, dimension and morphology. This binary nanostructuring concept originates with a distinctive binary-pore anodized aluminium oxide template that includes two dissimilar sets of pores in one matrix, where the openings of the two sets of pores are towards opposite sides of the template. Using the same growth mechanism, the binary-pore template can be extended to multi-pore templates with more geometrical options. We also present photoelectrodes, transistors and plasmonic devices made with our binary nanostructure arrays using different combination of materials and morphologies, and demonstrate superior performances compared to their single-component counterparts.

8. **Efficacious engineering on charge extraction for realizing highly efficient perovskite solar cells (Energy Environ. Sci. 2017, 10, 2570-2578)**

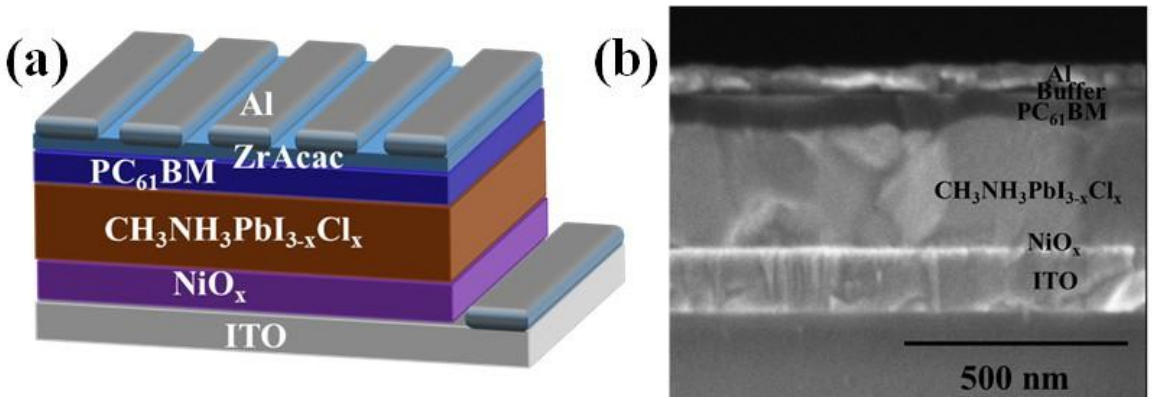

Efficient extraction of photogenerated charge carriers is of significance for acquiring a high efficiency for perovskite solar cells. In this paper, a systematic strategy for effectively engineering the charge extraction in inverted structured perovskite solar cells based on methylammonium lead halide perovskite ($CH_3NH_3PbI_{3-x}Cl_x$) is presented. Intentionally doping the chlorine element into the perovskite structure is helpful for obtaining a high open circuit voltage. The engineering is carried out by modifying the aluminium cathode with zirconium acetylacetonate, doping the hole transport layer of nickel oxide (NiOx) with copper and using an advanced fluorine doped tin oxide (FTO) substrate. This improves the bandgap alignment of the whole device, and thus, is of great benefit for extracting the charge carriers by promoting the transport rate and reducing the trap states. Consequently, an optimized power conversion efficiency of 20.5% is realized. Insights into how to extract charge carriers efficiently with a minimum energy loss are discussed.

9. A transparent CdS@ TiO_2 nanotextile photoanode with boosted photoelectrocatalytic efficiency and stability (Nanoscale 2017, 9, 15650-15657)

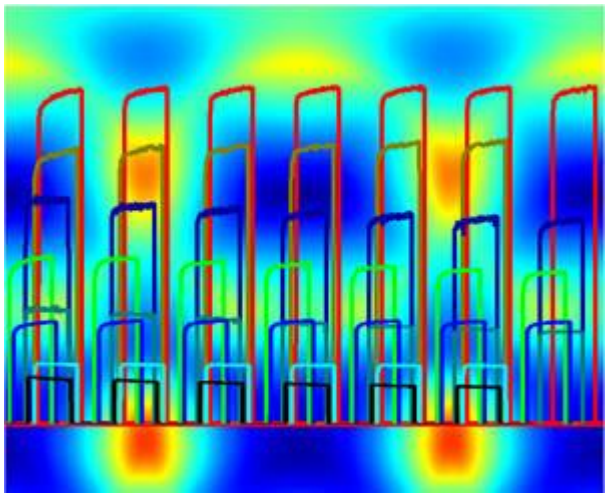

In the present work, we report the exploration of a transparent CdS@TiO_2 nanotextile photoanode with boosted photoelectrocatalytic (PEC) efficiency and stability, by the controllable coating of an amorphous TiO_2 ultrathin layer via the atomic layer deposition (ALD) technique. The optimal CdS@TiO_2 nanotextile photoanode with a 3.5 nm TiO_2 ultrathin layer exhibits a photocurrent density of 1.8 mA cm^{-2} at 0 V vs. RHE, which is 11 times higher than that of the pristine CdS counterpart. The photocatalytic H2 evolution rate of CdS@TiO_2 ranges up to 47.5 mmol g^{-1} h^{-1}, which is superior to those reported for one-dimensional CdS-based counterparts. Moreover, the photocurrent of CdS@TiO_2 nanotextile photoanodes shows only 9% decay after 9 h, suggesting its profoundly enhanced PEC stability, in comparison with that of pristine CdS photoanodes (almost down to zero after 3 hours). It is verified that the introduced TiO_2 nanoshells could limit the charge recombination, facilitate the charge separation, reduce the charge transfer resistance, and enhance the wettability of the electrodes, resulting in their significantly enhanced PEC performance.

10. Facile surface treatment on Cu_2O photocathodes for enhancing the photoelectrochemical response (Appl. Catal. B 2016, 198, 398-403)

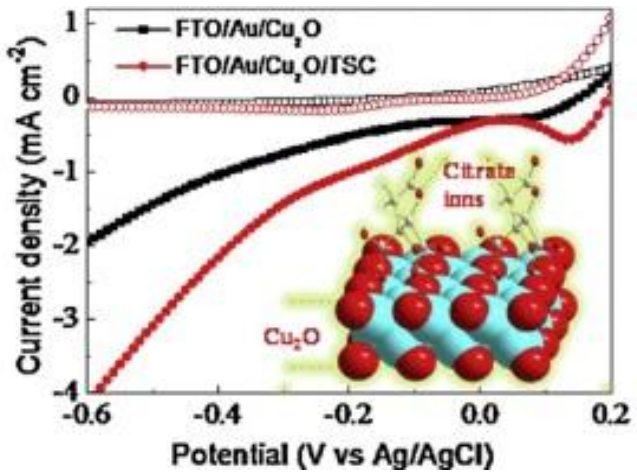

P-type Cu_2O has long been regarded as an advantageous material in photoelectrochemistry, owing to the suitable band gap structure and cost-effective production. However, such promising material is suffering from corrosion in aqueous electrolytes. To address this issue and attain a high photoelectrochemical performance, protective oxide layers and expensive catalysts have to be adopted. The complicacy of such additional procedures, however, limits the further applications. Instead of utilizing surface protecting oxide layers and expensive catalysts, herein, we report that the surface treatment of Cu_2O photocathodes using trisodium citrate (TSC) could also greatly enhance the photoelectrochemical performance. In comparison with the electrode without TSC, the photocathode of FTO/Au/Cu_2O/TSC/TiO_2/Pt presents a pronounced increment in photocurrent with a factor of about 2. Therefore, this paper provides a novel but convenient methodology to optimize the performance of solar energy conversion systems employing p-type Cu_2O by modifying the surface with functional molecules.

11. Fe (III) modified BiOCl ultrathin nanosheet towards high-efficient visible-light photocatalyst (Nano Energy 2016, 30, 109-117)

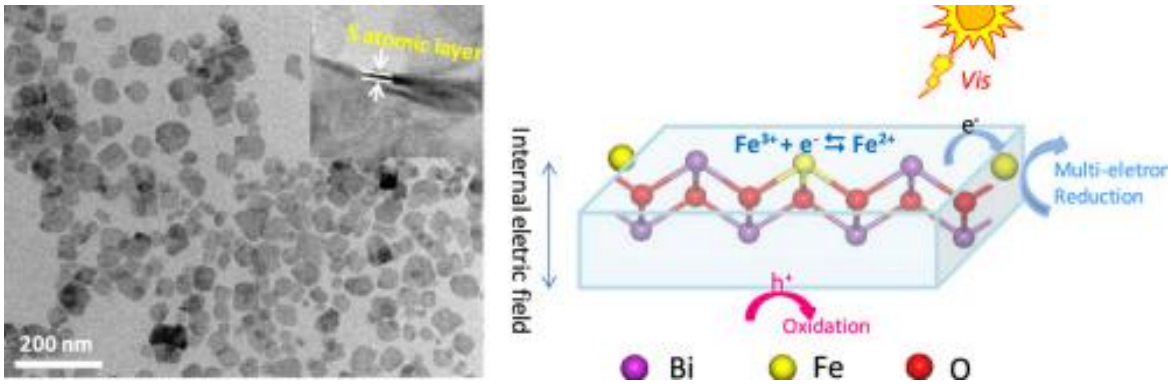

To pursue high photocatalytic activity in visible-light region, the Fe(III) modified BiOCl ultrathin nanosheet (Fe(III)@BOC NS) has been firstly synthesized via a facile solvothermal approach. The morphological and compositional characterizations reveal that the thickness of the as-prepared Fe(III)@BOC NS is less than 5 atomic layer with the exposure of active [001] facets. And the Fe(III) doping and surface grafting result in a 0.58 eV down-shift of the BiOCl conduction band minimum extending the light absorption from ultraviolet light to visible light region, as well as a promoted interfacial charge transfer upon visible light irradiation. Meanwhile, the Fe(III) modification introduces unique active sites on the surface of ultrathin nanosheet facilitating the surface reaction. Moreover, both of the appropriate self-induced electric field of [001] facets, and the shortened charge carrier diffusion length of ultrathin nanosheet enhance the separation and transfer efficiency of charge carriers. Therefore, by taking those advantages, we experimentally demonstrate that the Fe(III)@BOC NS is a high-efficiency visible-light photocatalyst for both of environment remediation and water splitting.

12. Effective approach to strengthen plasmon resonance localized on top surfaces of Ag nanoparticles and application in surface-enhanced Raman spectroscopy (Nanotechnology 2016, 27, 445301)

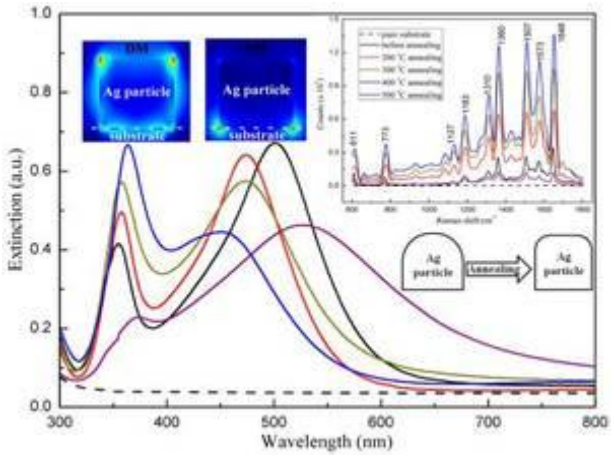

The spatial distribution of localized surface plasmon resonance (LSPR) plays a key role in many plasmonic applications. Based on the thermal stability of alumina templates, this work reports a novel approach to manipulate the distribution of LSPR and exhibits its significance for an important plasmonic application, the surface-enhanced Raman spectroscopy (SERS). A suitable thermal annealing sharpens the edges in top surfaces (far from the substrates) of Ag nanoparticles, which significantly strengthens the distal mode (DM) with the LSPR excited on the top surfaces. Because the top surface is the major place to adsorb probe molecules, this manipulation greatly improves the detection sensitivity of SERS. Our research provides a new way to improve the sensitivity of SERS, which also indicates that great care has to be taken on special LSPR mode which is largely responsible for a certain plasmonic application (e.g., the DM for SERS although it is not the major mode).

13. Manipulation of charge transfer and transport in plasmonic-ferroelectric hybrids for photoelectrochemical applications (Nat. Commun. 2016, 7, 10348)

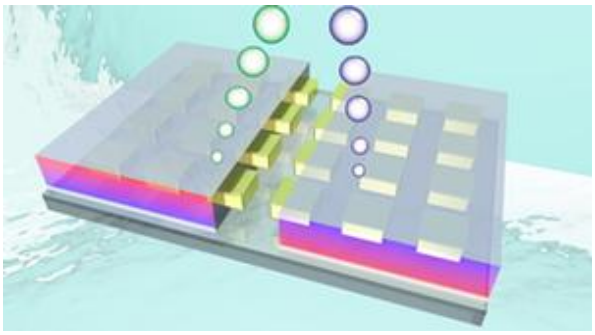

Utilizing plasmonic nanostructures for efficient and flexible conversion of solar energy into electricity or fuel presents a new paradigm in photovoltaics and photoelectrochemistry research. In a conventional photoelectrochemical cell, consisting of a plasmonic structure in contact with a semiconductor, the type of photoelectrochemical reaction is determined by the band bending at the semiconductor/electrolyte interface. The nature of the reaction is thus hard to tune. Here instead of using a semiconductor, we employed a ferroelectric material, $Pb(Zr,Ti)O_3$ (PZT). By depositing gold nanoparticle arrays and PZT films on ITO substrates, and studying the photocurrent as well as the femtosecond transient absorbance in different configurations, we demonstrate an effective charge transfer between the nanoparticle array and PZT. Most importantly, we show that the photocurrent can be tuned by nearly an order of magnitude when changing the ferroelectric polarization in PZT, demonstrating a versatile and tunable system for energy harvesting.

14. Exploration of nanowire- and nanotube-based electrocatalysts for oxygen reduction and oxygen evolution reaction (Materials Today Nano 2018, 3, 54-68)

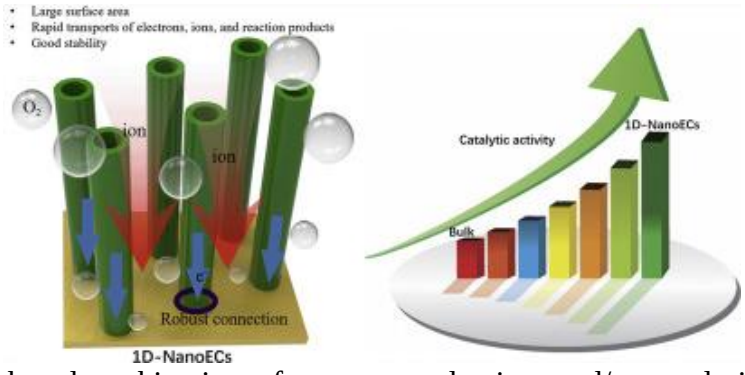

Electrocatalysts for oxygen reduction and/or evolution are key components for proton-exchange membrane fuel cells (PEMFCs) and water electrolysis. However, the slow kinetics of oxygen reduction and/or evolution reactions largely hampers the efficiencies of PEMFCs and water electrolysis. Highly efficient electrocatalysts for oxygen reduction and evolution reactions must meet three requirements: (i) rapid transport of electrons, ions, and products of the reaction; (ii) sufficient catalysts/reactants contact area; and (iii) good intrinsic activity. Nanostructuration of electrocatalysts provides an effective approach to overcome the slow kinetics because nanostructured electrocatalysts with rational design can not only provide sufficient active sites but also promote intrinsic activity of electrocatalysts as well as possess the ability of rapid transport of electrons, ions, and products of the reaction. Especially, electrocatalysts in the form of one-dimensional nanostructures (1D-Nano) such as nanowires (NWs) and nanotubes (NTs) have shown significant advantages, such as high surface area, rapid electron and mass transfer, low vulnerability to dissolution, Ostwald ripening, and aggregation, for oxygen evolution reaction (OER) and oxygen reduction reaction (ORR). In this review, we summarize different strategies for fabricating 1D nanostructure-based electrocatalysts (1D-NanoECs), which are categorized into template-free and template-assisted strategies, and emphasis has been placed on anodic aluminum oxide template–assisted strategies. Then, recent advances of 1D-NanoECs for ORR and OER applications are summarized. Finally, future challenges and opportunities about 1D-NanoECs are discussed.

15. Self-Supported Bi_2MoO_6 Nanowall for Photoelectrochemical Water Splitting (ACS Appl. Mater. Interfaces 2017, 9, 23647-23653)

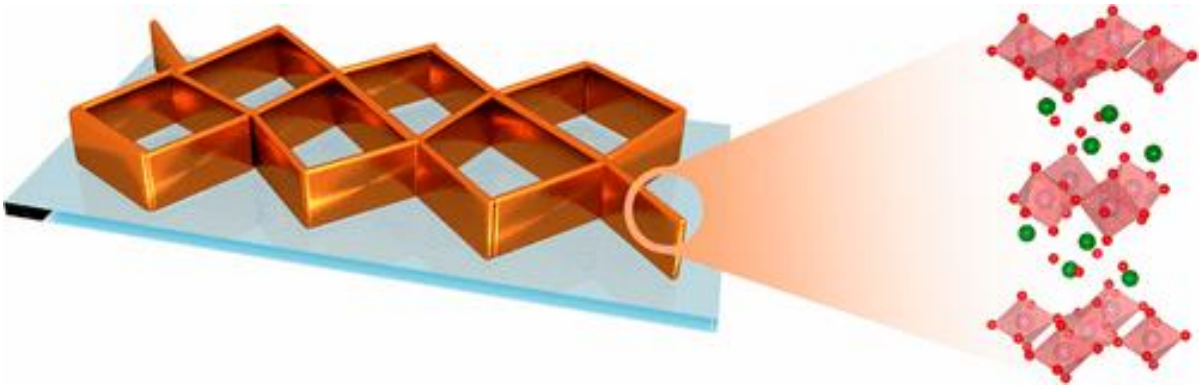

The nanowall has been regarded as a promising architecture for highly efficient photoelectrochemical (PEC) water splitting due to various advantages, such as open geometry, highly reactive facets, independent contact with current collector, and so forth. Here, a vertically aligned Bi_2MoO_6 nanosheet array, which is also called a nanowall, is first achieved directly on the ITO glass by a facile solvothermal approach. The structural features not only offer multiple superiorities for PEC processes, but also provide the bridge for in-depth insights of intrinsic features of Bi_2MoO_6 photoanodes. A quantitative analysis of the electrochemical process declares that the utilization of photogenerated charges in the Bi_2MoO_6 nanowall has been optimized, but the main obstacle comes from the severe bulk recombination and low efficiencies of charge separation. This evaluation both enriches the visual assessment methods and directs clear guidance for future improvement, which could serve as a beacon for well-directed and economic photoelectrode amelioration, to shorten the road toward ideal photoelectrodes.

16. Constructing well-defined AZO/TiO_2 core/shell nanocones with uniformly dispersed Au NPs for enhancing photoelectrochemical water splitting (Adv. Energy Mater. 2016, 6, 1501496)

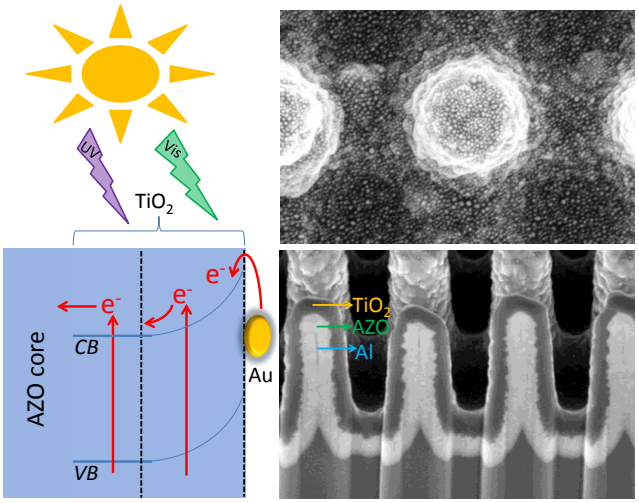

Constructing core/shell nanostructures with optimal structure and composition could maximize the solar light utilization. In this work, using an Al nanocone array as a substrate, well-defined regular array of AZO/TiO_2 core/shell nanocones with uniformly dispersed Au nanoparticles (AZO/TiO_2/Au NCA) is successfully realized through three sequential steps of atomic layer deposition, physical vapor deposition and annealing processes. By tuning the structural and compositional parameters, the advantages of light trapping and short carrier diffusion from the core/shell nanocone array, as well as the surface plasmon resonance and catalytic effects from the Au NPs can be maximally utilized. Accordingly, a remarkable PEC performance could be acquired and the photocurrent density of the AZO/TiO_2/Au NCA electrode reaches up to 1.1 mA/cm^2 at 1.23 V versus RHE under simulated sunlight illumination, which is five times of that from flat AZO/TiO_2 electrode (0.22 mA/cm^2). Moreover, the photoconversion of the AZO/TiO_2/Au NCA electrode approaches to 0.73% at 0.21 V versus RHE, which is one of the highest values with the lowest external potential that ever reported in Au/TiO_2 PEC composites. These results demonstrate a feasible route toward scalable fabrication of well-modulated core/shell nanostructures and can be easily applied to other metal/semiconductor composites for high-performance PEC electrodes.

17. The shift of the optical absorption band edge of ZnO/ZnS core/shell nanotube arrays beyond quantum effects (J. Mater. Chem. C 2016, 4, 1369-1374)

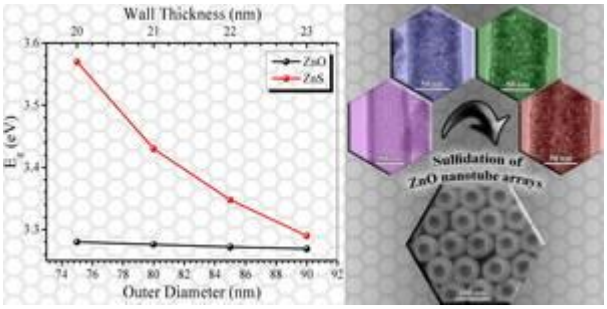

Unlike conventional investigations that focus on the manipulation of optical absorption band edge for a single componential material through quantum confinement effects, in this paper, we study the optical absorption properties of well-ordered ZnO/ZnS core/shell nanotube arrays. Our data point out that the profile of the absorbance spectrum of ZnO/ZnS nanotube arrays is determined by the two components and geometrical parameters of the nanostructure arrays. We find that both of the ZnO and ZnS show a decrease in the optical band gap with the increase in ZnS thickness and the diameter of the nanotube arrays, which is interestingly out of explanation from the material aspect. The subsequent finite-difference-time-domain simulations support such observations and illustrate that the geometrical and periodical parameters could also impact the optical absorption of the core/shell nanostructure arrays, even without concerning the quantum effects.

18. **Degenerating plasmonic modes to enhance the performance of surface plasmon resonance for application in solar energy conversion (Adv. Energy Mater. 2015, 5, 1501654)**

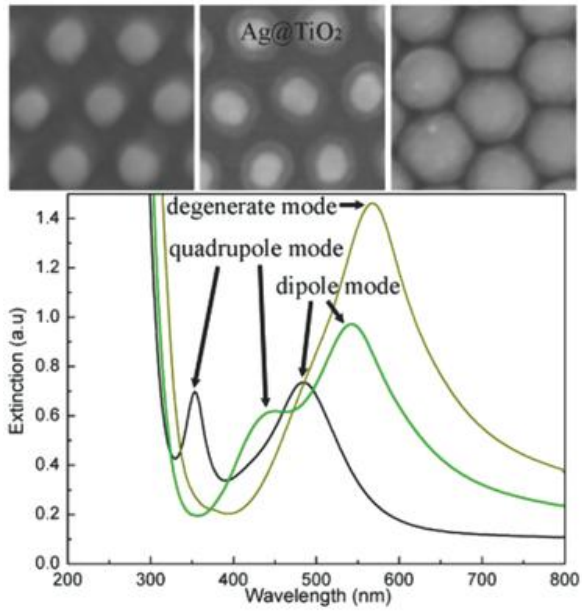

A new approach to enhance surface plasmon resonance (SPR) performance by degenerating the quadrupole and dipole SPR modes of highly ordered Ag nanoparticle arrays is proposed. The degenerate reason is confirmed to originate from the variation of refractive index in different wavelengths. The degenerate plasmonic modes strengthen SPR, which improves the photocurrent and photocatalytic activity in this incorporated system.

19. Designing Heterogeneous 1D Nanostructure Arrays Based on AAO Templates for Energy Applications (Small 2015, 11, 3408-3428)

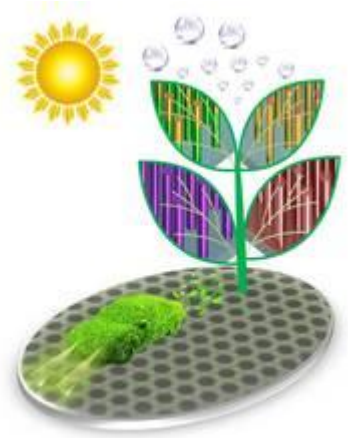

In order to fulfill the multiple requirements for energy production, storage, and utilization in the future, the conventional planar configuration of current energy conversion/storage devices has to be reformed, since technological evolution has promoted the efficiency of the corresponding devices to be close to the theoretical values. One promising strategy is to construct multifunctional 1D nanostructure arrays to replace their planar counterparts for device fabrication, ascribing to the significant superiorities of such 1D nanostructure arrays. In the last three decades, technologies based on anodic aluminium oxide (AAO) templates have turned out to be valuable meaning for the realization of 1D nanostructures and have attracted tremendous interest. In this review, recent progress in energy-related devices equipped with heterogeneous 1D nanostructure arrays that fabricated through the assistance of AAO templates is highlighted. Particular emphasis is given on how to develop efficient devices via optimizing the componential and morphological parameters of the 1D nanostructure arrays. Finally, aspects relevant to the further improvement of device performance are discussed.

20. Dimensional Dependence of the Optical Absorption Band Edge of TiO_2 Nanotube Arrays beyond the Quantum Effect (J. Phys. Chem. C 2015, 119, 16331-16337)

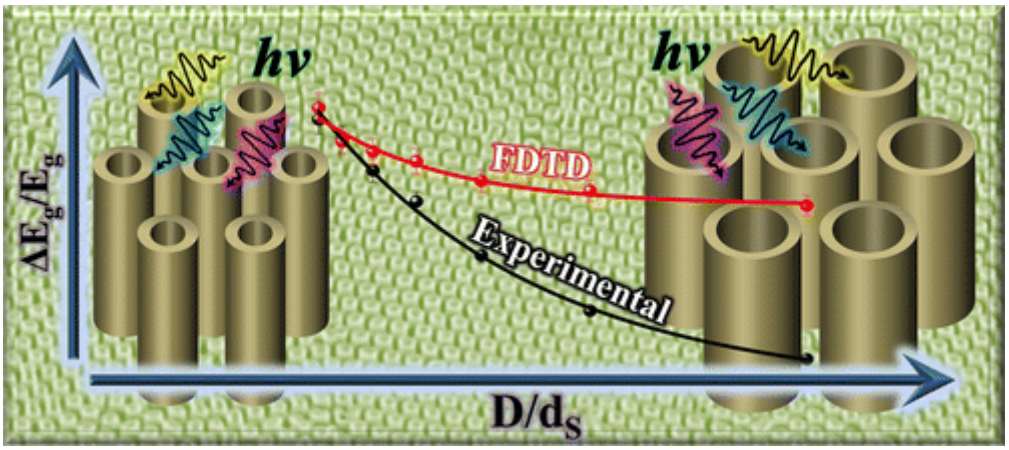

Instead of investigating the quantum effect that influences the absorption band edge of TiO_2 nanostructures, herein we report that geometrical parameters can also be utilized to manipulate the optical band gap of the TiO_2 nanotube arrays. Hexagonal arrays of TiO_2 nanotubes with an excellent crystalline quality were fabricated by techniques combining anodic aluminum oxide templates and atomic layer deposition. Through absorption spectroscopic analysis we observed that the optical absorption band edge of the TiO_2 nanotube arrays exhibited a red shift as the diameter of the nanotube was tuned to be larger and the distance between two nanotubes became smaller accordingly, while the wall thickness of the nanotube was kept constant. Subsequent finite-difference time-domain simulations supported the observation from theoretical aspect and revealed a large near-field enhancement around the outer space of the nanotubes for the arrays with densely distributed nanotubes when the corresponding arrays were exposed to the illuminations. Thus, this paper provides a new perspective for the shift of the optical band gap, which is of great significance to the research in photoelectronics.

21. Highly reproducible and sensitive SERS substrates with Ag internanoparticle gaps of 5 nm fabricated by ultrathin aluminum mask technique (ACS Appl. Mater. Interfaces 2015, 7, 13322–13328)

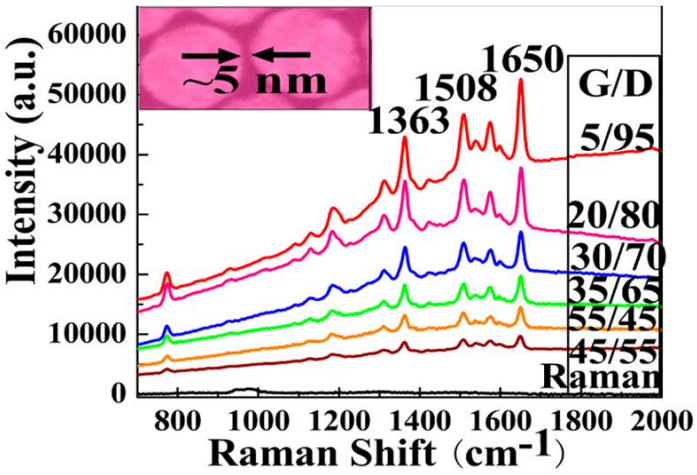

Applicable surface enhanced Raman scattering (SERS) active substrates require high enhancement factor (EF), excellent spatial reproducibility, and low-cost fabrication method on a large area. Although several SERS substrates with high EF and relative standard deviation (RSD) of signal less than 5% were reported, reliable fabrication for large area SERS substrates with both high sensitivity and high reproducibility via low-cost routes remains a challenge. Here, we report a facile and cost-effective fabrication process for large-scale SERS substrate with Ag inter-nanoparticle (NP) gaps of 5 nm based on ultrathin alumina mask (UTAM) surface pattern technique. Such closely packed Ag NP arrays with high density of electromagnetic field enhancement ("hot spots") on large area exhibit high SERS activity and excellent reproducibility, simultaneously. Rhodamine 6G molecules with concentration of 1×10^{-7} M are used to determine the SERS performance, and an EF of $\sim 10^9$ is obtained. It should be noted that we obtain RSDs about 2% from 10 random spots on an area of 1 cm^2, which implies the highly reproducible signals. Finite-difference time-domain simulations further suggest that the enhanced electric field originates from the narrow gap, which agrees well with the experimental results. The low value of RSD and the high EF of SERS signals indicate that the as-prepared substrate may be promising for highly sensitive and uniform SERS detection.

22. Highly controllable surface plasmon resonance property by heights of ordered nanoparticle arrays fabricated via a nonlithographic route (ACS Nano 2015, 9, 4583–4590)

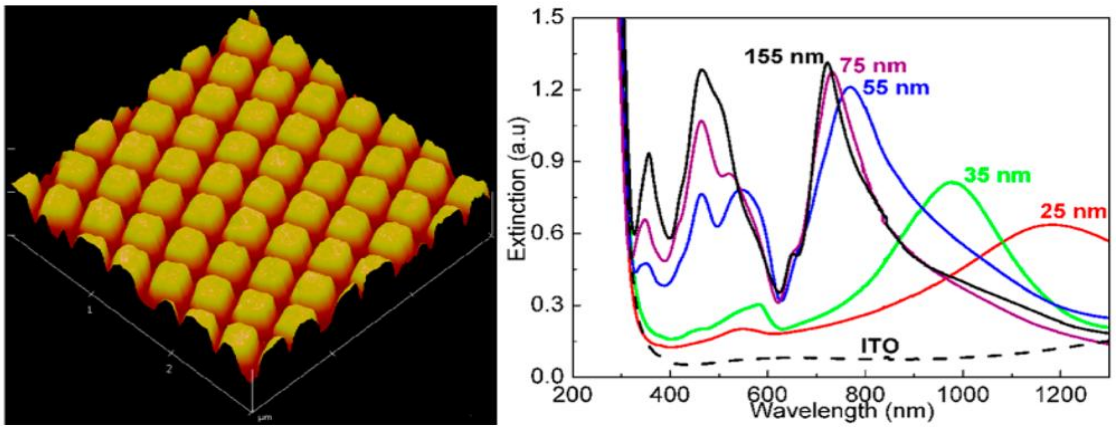

Perfectly ordered nanoparticle arrays are fabricated on large-area substrates (>cm^2) via a cost-effective nonlithographic route. Different surface plasmon resonance (SPR) modes focus consequently on their own positions due to the identical shape and uniform size and distance of these plasmonic metallic nanoparticles. On the basis of this and FDTD (finite-difference time-domain) simulation, this work reveals the variation of all SPR parameters (position, intensity, width, and mode) with nanoparticle heights, which demonstrates that the effect of heights are different in various stages. On increasing the heights, the major dipole SPR mode precisely blue-shifts from the near-infrared to the visible region with intensity strengthening, a peak narrowing effect, and multipole modes excitation in the UV–vis range. The intensity of multipole modes can be manipulated to be equal to or even greater than the major dipole SPR mode. After coating conformal TiO_2 shells on these nanoparticle arrays by atomic layer deposition, the strengthening of the SPR modes with increasing the heights results in the multiplying of the photocurrent (from ~2.5 to a maximum 90 μA cm^{-2}) in this plasmonic-metal–semiconductor-incorporated system. This simple but effective adjustment for all SPR parameters provides guidance for the future design of plasmonic metallic nanostructures, which is significant for SPR applications.

23. Fully understanding the positive roles of plasmonic nanoparticles in ameliorating the efficiency of organic solar cells (Nanoscale 2015, 7, 15251-15257)

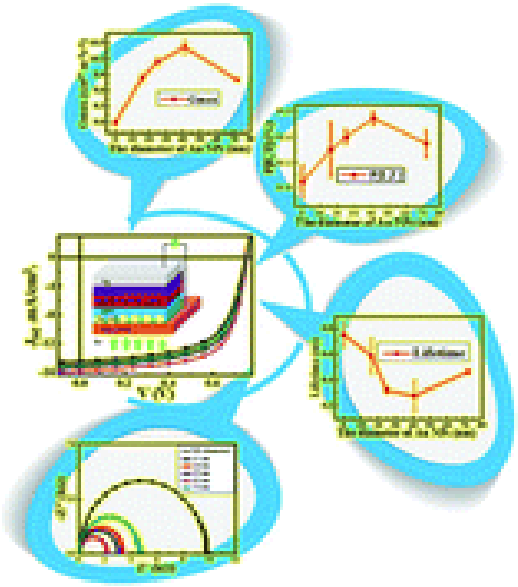

Herein, we constructed inverted PBDTTT-CF:$PC_{70}BM$ bulk-heterojunction organic solar cells by introducing Au nanoparticles to a ZnO buffer layer and a great improvement in energy conversion efficiency has been realized. To discover the positive roles of such plasmonic nanoparticles in the process of solar energy conversion, photovoltaic devices with the same architecture but different sized Au nanoparticles were purposely fabricated and it has been observed that the overall efficiency can be remarkably improved from 6.67% to 7.86% by embedding 41 nm Au nanoparticles in the buffer layer. The devices with other sizes of Au nanoparticles show a relatively low performance. Subsequent investigations including FDTD simulation and transient photoluminescence studies reveal that the existence of the plasmonic particles could not only improve the optical absorption and facilitate the exciton separation, but can also benefit the collection of charge carriers. Thus, this paper provides a comprehensive perspective on the roles of plasmonic particles in organic solar cells and insights into the photo energy conversion process in the plasmonic surroundings.

Scientific contribution

In total I have published and jointly published 26 papers in scientific journals during my Ph.D period, including 12 papers with impact factor higher than 10 (Nature Nanotechnology, Nature Communicaiton, Nano Energy, Energy & Environmental Science, ACS Nano, Nano Letters, Advanced Energy Materials, Applied Catalysis, B: Environmental), 10 papers with impact factor between 5 and 10 (Nanoscale, Small, Journal of Power Sources, Journal of Materials Chemistry C, and ACS applied materials & interfaces), and 2 paper with impact factor between 3 and 5 (Nanotechnology and Journal of Physical Chemistry C). The published papers were cited for over 800 times during my Ph.D study. (Source: google scholar database). I also gave contributions at conferences, including 2 talks and 1 posters.

Publications in SCI-indexed Scientific Journals during my Ph.D. study

1. R. Xu, H. Zhao, H. Jin, Z. Wang, Z. Zhang, S. Xu, Z. Zeng, S. Wang, Y. Lei, Scalable fabrication of geometry-tunable self-aligned superlattice photonic crystals for spectrum-programmable light trapping, ***Nano Energy***, 2019, 58, 543-551.
2. L. Wen,[+] R. Xu,[+] C. Cui, W. Tang, Y. Mi, X. Lu, Z. Zeng, S. Suib, P. Gao, Y. Lei, Template-guided programmable Janus hetero-nanostructure arrays for efficient plasmonic photocatalysis, ***Nano Letters***, 2018, 18, 8, 4914-4921. (co-first author)
3. R. Xu, L. Wen, Z. Wang, H. Zhao, S. Xu, Y. Mi, Y. Xu, M. Sommerfeld, Y. Fang, Y. Lei, Three-Dimensional Plasmonic Nanostructure Design for Boosting Photoelectrochemical Activity, ***ACS Nano***, 2017, 11, 7382-7389.
4. Z. Wang,[+] D. Cao,[+] R. Xu,[+] S. Qu, Z. Wang, Y. Lei, Realizing ordered arrays of nanostructures: A versatile platform for converting and storing energy efficiently, ***Nano Energy***, 2016, 19, 328-362. (co-first author)
5. S. Tarish,[+] A. Al-Haddad,[+] R. Xu,[+] D. Cao, Z. Wang, S. Qu, G. Nabi, Y. Lei, The shift of the optical absorption band edge of ZnO/ZnS core/shell nanotube arrays beyond

quantum effects, ***Journal of Materials Chemistry C***, 2016, 4, 1369-1374. (co-first author)

****

6. L. Wen, R. Xu, Y. Mi, Y. Lei, Multiple nanostructures based on anodized aluminium oxide templates, ***Nature Nanotechnology*** 2017, 12, 244-250.
7. Y. Sun, S. Lu, R. Xu, K Liu, Z. Zhou, S. Yue, M. Azam, K. Ren, Z. Wei, Z. Wang, Collection optimization of photo-generated charge carriers for efficient organic solar cells, ***Journal of Power Sources***, 2019, 412, 465-471.
8. S. Xu, Y. Xu, H. Zhao, R. Xu, Y Lei, Sensitive Gas-Sensing by Creating Adsorption Active Sites: Coating an SnO_2 Layer on Triangle Arrays, ACS A***pplied Materials & Interfaces***, 2018, 10, 29092-29099.
9. M. Azam, S. Yue, R. Xu, L. Kong, K. Ren, J. Liu, Z. Wang, S. Qu, Y. Lei, Z. Wang, Highly efficient solar cells based on Cl incorporated tri-cation perovskite materials, ***Journal of Materials Chemistry A*** 2018, 6, 13725-13734.
10. Z. Wang, D. Cao, L. Wen, R. Xu, M. Obergfell, Y. Mi, Z. Zhan, N. Nasori, J. Demsar, Y. Lei, Manipulation of charge transfer and transport in plasmonic-ferroelectric hybrids for photoelectrochemical applications, ***Nature Communications*** 2016, 7, 10348.
11. L. Liu, H. Hou, L. Wang, R. Xu, Y. Lei, S. Shen, D. Yang, W. Yang, A transparent CdS@TiO_2 nanotextile photoanode with boosted photoelectrocatalytic efficiency and stability, ***Nanoscale*** 2017, 9, 15650-15657.
12. M. Wu, Y. Wang, Y. Xu, J. Ming, M. Zhou, R. Xu, Q. Fu, Y. Lei, Self-supported Bi_2MoO_6 Nanowall for Photoelectrochemical Water Splitting, ***ACS Applied Materials & Interfaces*** 2017, 9, 23647-23653.
13. S. Yue, K. Liu, R. Xu, M. Li, M. Azam, K. Ren, J. Liu, Y. Sun, Z. Wang, D. Cao, X. Yan, S. Qu, Y. Lei, Z. Wang, Efficacious engineering on charge extraction for

realizing highly efficient perovskite solar cells, ***Energy & Environmental Science*** 2017, 10, 2570-2578.

14. D. Cao, N. Nasori, Z. Wang, L. Wen, R. Xu, Y. Mi, Y. Lei, Facile surface treatment on Cu2O photocathodes for enhancing the photoelectrochemical response, ***Applied Catalysis B: Environmental*** 2016, 198, 398-403.
15. Z. Zhan, R. Xu, X. Zheng, Q. Fu, M. Wu, Y. Lei, Effective approach to strengthen plasmon resonance localized on top surfaces of Ag nanoparticles and application in surface-enhanced Raman spectroscopy, ***Nanotechnology*** 2016, 27, 445301.
16. Y. Mi, L. Wen, R. Xu, Z. Wang, D. Cao, Y. Fang, Y. Lei, Constructing a AZO/TiO2 core/shell nanocone array with uniformly dispersed Au NPs for enhancing photoelectrochemical water splitting, ***Advanced Energy Materials*** 2016, 6, 1501496.
17. L. Wen, Z. Wang, Y. Mi, R. Xu, S. Yu, Y. Lei, Designing heterogeneous 1D nanostructure arrays based on AAO templates for energy applications, ***Small*** 2015, 11, 3408-3428.
18. A. Al-Haddad, Z. Wang, R. Xu, H. Qi, R. Vellacheri, U. Kaiser, Y. Lei, Dimensional dependence of the optical absorption band edge of TiO_2 nanotube arrays beyond the quantum effect, ***The Journal of Physical Chemistry C*** 2015, 119, 16331-16337.
19. Q. Fu, Z. Zhan, J. Dou, X. Zheng, R. Xu, M. Wu, Y. Lei, Highly reproducible and sensitive SERS substrates with Ag inter-nanoparticle gaps of 5 nm fabricated by ultrathin aluminum mask technique, ***ACS Applied Materials & Interfaces*** 2015, 7, 13322-13328.
20. Y. Mi, L. Wen, Z. Wang, D. Cao, R. Xu, Y. Fang, Y. Zhou, Y. Lei, Fe (III) modified BiOCl ultrathin nanosheet towards high-efficient visible-light photocatalyst, ***Nano Energy*** 2016, 30, 109-117.

21. D. Chi, S. Lu, R. Xu, K. Liu, D. Cao, L. Wen, Y. Mi, Z. Wang, Y. Lei, S. Qu, Z. Wang, Fully understanding the positive roles of plasmonic nanoparticles in ameliorating the efficiency of organic solar cells, ***Nanoscale*** 2015, 7, 15251-15257.
22. Z. Zhan, F. Grote, Z. Wang, R. Xu, Y. Lei, Degenerating plasmonic modes to enhance the performance of surface plasmon resonance for application in solar energy conversion, ***Advanced Energy Materials*** 2015, 5, 1501654.
23. Z. Zeng, R. Xu, H. Zhao, H. Zhang, S. Xu, Y. Lei, Exploration of Nanowire-and Nanotube-Based Electrocatalysts for Oxygen Reduction and Oxygen Evolution Reaction, ***Materials Today Nano***, 2018, 3, 54-68.
24. Z. Zhan, R. Xu, Y. Mi, H. Zhao, Y. Lei, Highly controllable surface plasmon resonance property by heights of ordered nanoparticle arrays fabricated via a nonlithographic route, ***ACS Nano*** 2015, 9, 4583-4590.
25. M. Eckstein, C. Koppka, S. Thiele, Y. Mi, R. Xu, Y. Lei, B. Hähnlein, F. Schwierz, J. Pezoldt, MOCVD Compatible Atomic Layer Deposition Process of Al2O3 on SiC and Graphene/SiC Heterostructures, ***Materials Science Forum*** 2018, 924, 506-510.
26. S. Xu, H. Zhao, Y. Xu, R. Xu, Y. Lei, Carrier Mobility-Dominated Gas Sensing: A Room-Temperature Gas-Sensing Mode for SnO2 Nanorod Array Sensors, ***ACS Applied Materials & Interfaces***, 2018, 10, 13895-13902.

****

Unpublished manuscripts

27. R. Xu, L. Wen, Z. Wang, Z. Zeng, M. Zhou, S. Bohm, H. Zhang, Y. Wu, E. Runge,Y. Lei, Programmable multiple plasmonic resonance of nanoparticle superlattice for enhancing photoelectrochemical activity (**under submission**).
28. R. Xu, Z. Zeng, Y Lei, Well-defined nanostructuring with programmable anodic aluminum oxide templates (**under submission**).

Conference contribution

1. R. Xu, H. Zhao, Y. Lei, Wafer-scale metallic two-dimensional superlattice photonic crystals for light trapping, 82th Annual Conference of the DPG, Mar 11- Mar 16, 2018, Berlin, Germany. **Talk.**
2. R. Xu, L. Wen, Z. Wang, H. Zhao, S. Xu, Y. Mi, Y. Xu, M. Sommerfeld, Y. Fang, Y. Lei, Omnidirectional Photoelectrochemical Activity of Ultrathin CdS film on Periodic Three-Dimensional Composite Pillar/Truncated-Pyramid Au arrays, 81th Annual Conference of the DPG, Mar 19- Mar 24, 2017, Dresden, Germany. **Talk.**
3. R. Xu, L. Wen, Z. Wang, H. Zhao, S. Xu, Y. Mi, Y. Xu, M. Sommerfeld, Y. Fang, Y. Lei Three-dimensional plasmonic nanostructure design for boosting photoelectrochemical Activity, 82th Annual Conference of the DPG, Mar 11- Mar 16, 2018, Berlin, Germany. **Poster.**

Declaration

I hereby declare that this Ph.D. dissertation entitled “Boosting Solar Energy Harvesting with Ordered Nanostructures Fabricated by anodic aluminum oxide templates” was carried out by me for the degree of Doctor of Philosophy under the supervision of Prof. Dr. Yong Lei. All dates or information in this dissertation that have been directly or indirectly consulted or used from other sources are clearly stated. This dissertation has not been submitted, in part or in whole, for any other degree or examination in any other University. I have acknowledged all main sources of help, and I have made clear exactly what was done by others and what I have contributed when the work was done jointly with others. Some of the results may have been published in scientific journals or elsewhere. I am aware that the falsity of this declaration will be regarded as an attempt of deception and will cause the derogation of the doctoral procedure.

Ilmenau,01/07/2019

Rui Xu